

Research Activities

– Synchrotron Radiation Experiments –

Study of electronic state of oxygen adsorbed Nb(110) using high-resolution angle-resolved photoemission spectroscopy

Y. Miyai^a, E. F. Schwier^b and K. Shimada^b

^a*Graduate School of Science, Hiroshima University, Kagamiyama 1-3-1, Higashi-Hiroshima 739-8526, Japan*

^b*Hiroshima Synchrotron Radiation Center, Hiroshima University, Kagamiyama 2-313, Higashi-Hiroshima 739-0046, Japan*

Keywords: superconductor, superconducting gap, ARPES, electron-phonon interaction

Superconductivity is an interesting physical phenomenon in which electrical resistance disappears at low temperature [1]. Among elemental superconductors, Nb has the highest transition temperature of $T_c=9.2$ K [1]. Recently, interfacial electronic states between Nb thin films and topological insulators have been reported in order to search for the Majorana fermion [2], and topologically non-trivial states have been predicted in the conduction band of Nb(110) [3]. However, the electronic band structure of the bulk and surfaces of Nb single crystals has not been elucidated experimentally so far. One of the reasons is the difficulty of clean surface reparation due to the segregation of oxygen atoms on the surface [4].

In this study, we have done high-resolution photoemission spectroscopy to examine the influence of oxygen on the superconductivity of Nb. A highly ordered oxygen-reconstructed Nb (110) surface was prepared by several cycles of annealing (1300 °C for several hours) and flashing (2000 °C for 10 sec). The reconstructed surface structure was judged by sharp low energy electron diffraction (LEED) spots. We used photon energies in the lower soft x-ray regime at the linear undulator beamline of BL-1 [5] and 6.3 eV at the μ -LaserARPES machine [6].

Figure 1(a) shows angle-integrated photoemission spectra taken above and below the superconducting transition temperature using laser. The appearance of the superconducting gap below T_c is clearly observed and allows us to extract its temperature dependence by fitting its spectral shape using the Dynes function [7],

$$\rho(\omega) = \rho_0 \operatorname{Re} \left[\frac{\omega + i\Gamma}{\sqrt{(\omega + i\Gamma)^2 - \Delta^2}} \right],$$

convoluted with a Gaussian whose width represents instrumental energy resolution. Here, Γ and Δ are parameters to be determined by the fit of the experimental spectra. The obtained gap size $\Delta(T)$ as a function of temperature is shown in Fig. 1(b). Here we should note that there exist errors as seen in Fig. 1(b), which is due to the statistics and intrinsic linewidth broadening. We attempted to fit the temperature dependence of Δ using an interpolation formula for the BCS superconducting gap

$$\Delta(T) = \Delta_0 \tanh \left[1.74 \sqrt{\frac{T_c}{T} - 1} \right]$$

following

previous study [6], and obtained the zero-temperature gap size as $\Delta_0 = 1.4$ meV and the transition temperature as $T_c = 9.5$ K. The Δ_0 value is comparable to previous studies on polycrystalline Nb [6,8]. Then we obtain $2\Delta_0/(k_B T_c) \sim 3.4$, which is closer to the BCS value, $2\Delta_0/(k_B T_c) \sim 3.53$ [1], and slightly smaller than the values obtained from the transport measurements, $2\Delta_0/(k_B T_c) \sim 3.876 - 3.883$ [1], or obtained from

photoemission studies on clean polycrystalline Nb, $2\Delta_0 / (k_B T_C) \sim 3.7$ [6,8].

We could observe an energy band crossing E_F in angle-resolved photoemission spectroscopy taken at 6.3 eV. By fitting the momentum distribution curves with a Lorentzian, we have obtained the dispersion as shown in Fig. 1(c). A clear kink structure exists around -25 meV which coincides with the Debye energy of 27-28 meV [1], indicating that the kink is originated from the electron-phonon interaction. By fitting the energy band dispersion below and above the kink structure with a linear function, we estimated the Fermi velocities with (v_F) and without (v_F^0) band renormalization. Then the electron-phonon coupling constant is evaluated as $\lambda = v_F^0 / v_F - 1 = 0.83 \pm 0.02$. The value is slightly smaller than that determined by the transport measurements, $\lambda = 1.01 - 1.22$ [1]. In general, if the coupling constant is smaller (larger) than 1, it is called weak (strong) coupling. In the case of Nb, the strength of the electron-phonon interaction is marginal between strong and weak coupling regimes. The reduced coupling strength for the oxygen adsorbed surface is also consistent with smaller $2\Delta_0 / (k_B T_C)$ value.

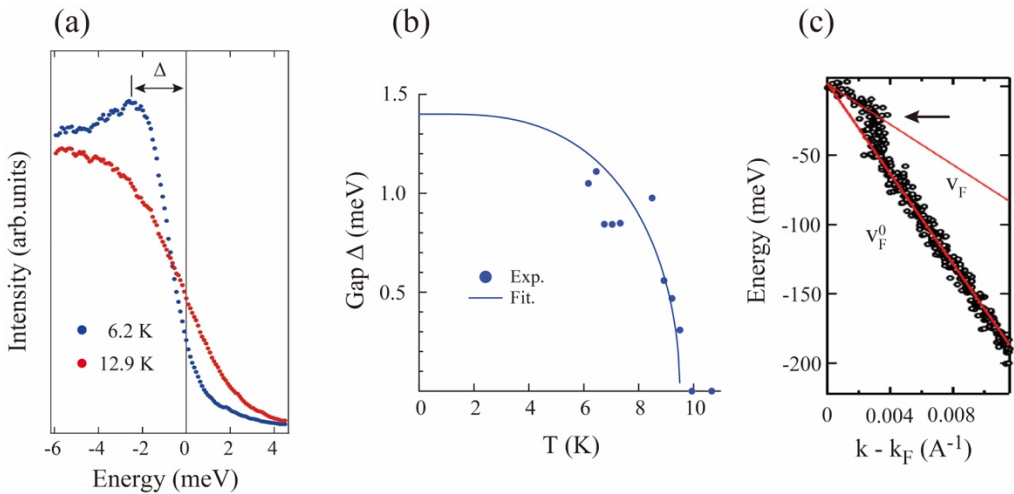


Fig. 1 (a) Energy distribution curves taken by the laser at $h\nu=6.3$ eV above and below the superconducting transition temperature. The superconducting gap is clearly visible at 6.2 K. (b) The superconducting gap Δ evaluated by the fit of photoemission spectra using a Dynes function. The solid line shows the fit using the interpolation function for the BCS gap function. (c) Band points determined by the MDC analyses. A kink around -25 meV is clearly visible.

REFERENCES

1. J. P. Carbotte, Rev. Mod. Phys. **62**, 1027 (1990).
2. J. Shen *et al.*, PNAS **117**, 238 (2020).
3. D. Thonig *et al.*, Phys. Rev. B **94**, 155132 (2016).
4. A. Odobesko *et al.*, Phys. Rev. B **99**, 115437 (2019).
5. H. Iwasawa *et al.*, J. Synchrotron Rad. **24**, 836 (2017).
6. H. Iwasawa *et al.*, Ultramicroscopy **182**, 85 (2017).
7. F. Herman and R. Hlubina, Phys. Rev. B **94**, 144508 (2016).
8. T. Yokoya *et al.*, J. Electron Spectrosc. Relat. Phenomen. **124**, 99 (2002).

High-resolution polarization-dependent angle-resolved photoemission spectroscopy study of O-Fe(100) thin films grown on MgO(100)

Mingtian Zheng^a, Eike F. Schwier^b, and Kenya Shimada^b

^a*Graduate School of Science, Hiroshima University, Kagamiyama 1-3-1, Higashi-Hiroshima 739-8526, Japan*

^b*Hiroshima Synchrotron Radiation Center, Hiroshima University, Kagamiyama 2-313, Higashi-Hiroshima 739-0046, Japan*

Keywords: Fe(001)/MgO(001)-p(1×1)-O, ARPES, electron correlation, p-d hybridization

The p(1×1) oxygen adsorbed ferromagnetic Fe(001) surface has been extensively studied so far [1-6]. On this surface, the oxygen atoms occupy the four-fold hollow sites of the Fe(001) surface [1]. The low-energy electron diffraction (LEED) [1] and surface x-ray diffraction experiments [2] revealed that the distance between the topmost and second Fe layers is enhanced after oxygen adsorption, and the distance between the oxygen and topmost Fe atoms is much smaller than the Fe-Fe atomic distance in the bulk [1,2]. The spin- and angle-resolved photoemission spectroscopy clarified exchange split O 2p bands extending from -4 eV to -9 eV below the Fermi level (E_F), as well as the momentum-dependent exchange splitting [3]. Inverse photoemission spectroscopy indicated an appearance of the image-potential state and suppression of the minority-spin Fe 3d_{3z2-r2} state located just above E_F after the oxygen adsorption [4]. Owing to the high spin-dependent electron reflectivity and chemical stability, the Fe(001)-p(1×1)-O surface has been successfully applied to the target material in the highly efficient VLEED-type spin detector [5]. The magnetic and transport properties of the surface is directly related to the electronic states near E_F near the surface region. The scanning tunneling spectroscopy study combined with the density-functional theory (DFT) calculation has clarified the peak in the local density of state at -0.7 eV below E_F derives from the hybridization between Fe 3d_{xz}, 3d_{yz} and O 2p_x, 2p_y, and the peak just above E_F is from the hybridization between Fe 3d_{3z2-r2} and O 2p_z [2]. However, detailed energy dispersions near E_F have not been elucidated so far.

In this study, therefore, we have done polarization-dependent angle-resolved photoemission spectroscopy (ARPES) of the Fe(001)-p(1×1)-O surface in order to understand the electronic states near E_F near the surface region. In this report we describe some of our major results. For more details, please refer to our paper [6].

We prepared clean Fe(001) single crystalline films by depositing Fe on MgO(001) substrate and subsequent annealing at 800 K for 30 min. The oxygen adsorbed surface was fabricated by dosing 1500 L O₂ at room temperature and heated by flash annealing to 900 K. The obtained surfaces were checked by LEED and Auger electron spectroscopy. Figs. 1(a) and (b) show obtained LEED images for pure Fe(001) and Fe(001)-p(1×1)-O surfaces, respectively. One can see sharp 1×1 LEED spots indicating high quality of the sample surface. The polarization-dependent ARPES experiments were performed at HiSOR BL-1 with a photon energy of $h\nu=55$ eV for enhanced surface sensitivity. The sample temperature was set at 12 K, energy and momentum resolutions were 16 meV and 0.051 Å⁻¹. In Figs. 1(d)-(g), one can clearly see polarization dependence of the ARPES spectral features.

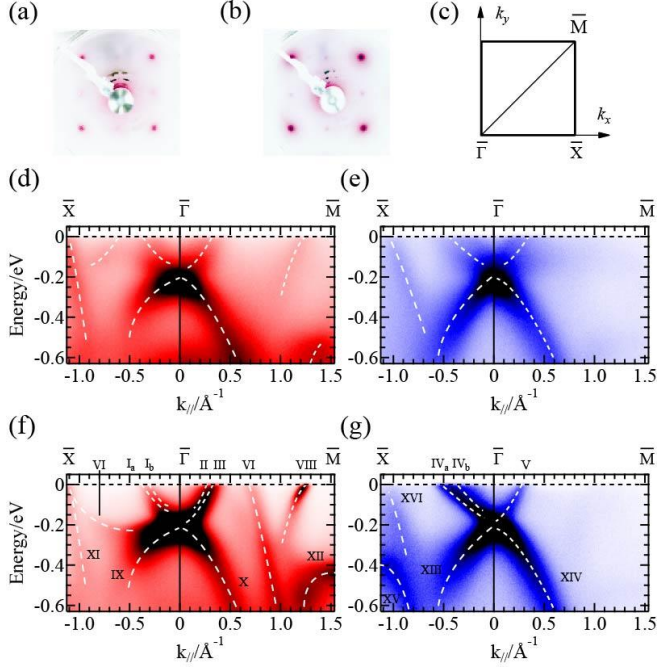


FIGURE 1 (a) and (b) respectively show LEED images of clean Fe(001) and Fe(001)-p(1×1)-O surfaces taken at an incident electron energy of 39 eV. (c) Surface Brillouin zone. (d) and (e) respectively show ARPES image plots taken with p- and s-polarization geometries for clean Fe(001) surface. (f) and (g) respectively show ARPES image plots taken with p- and s-polarization geometries for Fe(001)-p(1×1)-O surface. ARPES spectra were taken at $h\nu=55$ eV at 12 K. Dashed lines are guides for the band dispersions. Figures are from [6].

To interpret these spectral features, we have done extensive DFT calculations using the openMX code for a 41 monolayer thick Fe(001) slab covered with a p(1×1) O layer on both surfaces [6]. We extracted the layer-, orbital-, and spin-resolved contributions to each eigenenergy of the electron band dispersion, which allows us to understand the origin of the ARPES spectral features. We have assumed that the mid-st Fe layer (the central Fe layer in the slab) has the bulk electronic property. Based on the DFT results, the deviation from the bulk electronic states is significant for 1st and 2nd Fe layers, and much smaller below 3rd Fe layers. Therefore, we compare our ARPES results with the DFT results for the 1st, 2nd and bulk Fe layers.

Fig. 2(b) shows ARPES intensity plot taken with the p-polarization geometry along the $\bar{\Gamma}-\bar{M}$ high symmetry line. In the p-polarization geometry, we can selectively detect the electronic states having even symmetry with respect to the $\bar{\Gamma}-\bar{M}$ high symmetry line. There exist 6 bands (II, III, VII, VIII, X, XII) in Fig. 2(b), and 4 bands (II, III, VII, VIII) are crossing E_F in Fig. 2(a). Figs. 2(c)-(m) show the results of layer- and orbital-resolved DFT calculations compatible with the p-polarization geometry. Here we have added spin-up and spin-down contributions. While the DFT results look complicated, one can see some spectral features corresponding to the ARPES features. For example, the band II and III in the ARPES image plot are mainly derived from the Fe $3d_{(x+y)z}$ orbitals on the 1st and 2nd Fe layers as shown in Figs. 2 (f)-(g). One can also identify corresponding features in O $2p_{x+y}$ orbital indicating the hybridization between Fe $3d_{(x+y)z}$ and O $2p_{x+y}$ orbitals. On the other hand, the band XII is mainly derived from the Fe $3d_{3z^2-r^2}$ orbital on the 2nd Fe layer, and some contribution from the Fe $3d_{xy}$ orbital on the 1st layer. One can also see a corresponding spectral feature in O $2p_z$ which is consistent with the p-d hybridization along the z axis (perpendicular to the surface). It looks also reasonable there exist a contribution from the Fe $3d_{xy}$ orbital because O is situated on the hollow site of the Fe(001) surface, where the Fe $3d_{xy}$ orbital has a large amplitude.

The observed Fermi wavenumber is, however, only \sim 50% of the DFT results. At the $\bar{\Gamma}$ point, furthermore, the band II and III take the minimum energy of -0.2 eV, whereas the DFT calculations give -0.7 eV implying a band renormalization effect as in the pure Fe [7]. In the case of band XII, on the other hand, the maximum energy is located at -0.4 eV at the \bar{M} point, whereas the DFT calculation gives -0.2 eV. In this case, the energy shift is away from E_F . We also found that the magnitudes of deviation from the DFT results are different depending on the high symmetry directions. These results suggest anisotropic interplay of electron correlation and p-d hybridization in the near surface region. These effects modify the surface carrier density and shapes of the Fermi surface, and lead to the orbital dependent effective mass enhancement. In this study, we have fully clarified the electronic structures of Fe(001)-p(1 \times 1)-O surface [6], providing a foundation to understand spin-dependent magnetic and transport properties of the surface.

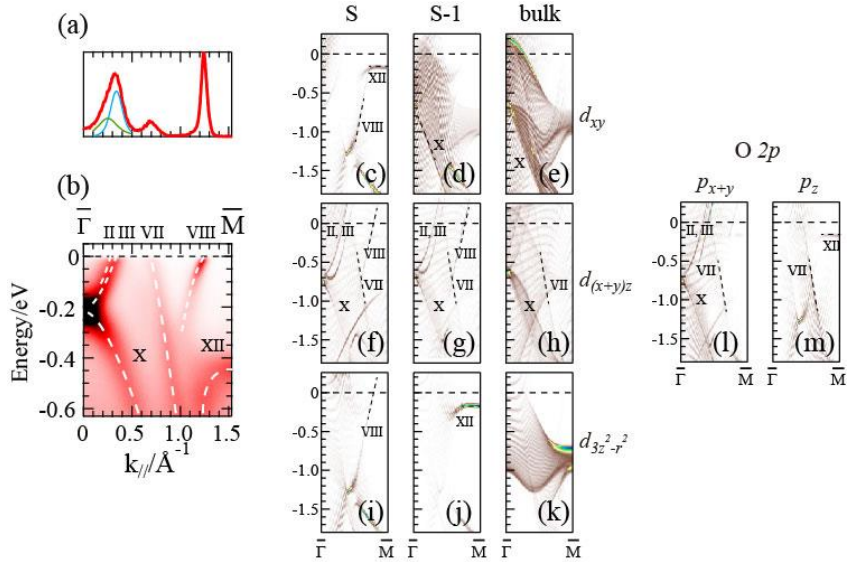


FIGURE 2 (a) Momentum distribution curve at E_F . (b) ARPES image plot with p-polarization geometry along the $\bar{\Gamma}-\bar{M}$ direction. (c)-(m) Layer- and orbital-resolved DFT results along the $\bar{\Gamma}-\bar{M}$ direction. Spin-up and spin-down states are added. S, S-1 denote the 1st and 2nd Fe layer. (c)-(e) Fe $3d_{xy}$ orbital. (f)-(h) Fe $3d_{(x+y)z}$ orbital. (i)-(k) Fe $3d_{3z^2-r^2}$ orbital. (l) O $2p_{x+y}$ orbital. (m) O $2p_z$ orbital. Dashed lines in the figures are guides for the band dispersions. These figures are after [6].

REFERENCES

1. F. Jona and P.M. Marcus, Solid State Commun. 64, 667 (1987).
2. S.S. Parihar, H.L. Meyerheim, K. Mohseni, S. Ostanin, A. Ernst, N. Jedrecy, R. Felici, J. Kirschner, Phys. Rev. B 81, 075428 (2010).
3. P.D. Johnson, A. Clarke, N.B. Brookes, S.L. Hulbert, B. Sinkovic, N.V. Smith, Phys. Rev. Lett. 61 2257 (1988).
4. C. Eibl, A.B. Schmidt, M. Donath, Phys. Rev. B 86 161414 (2012).
5. T. Okuda, Y. Takeichi, Y. Maeda, A. Harasawa, I. Matsuda, T. Kinoshita, A. Kakizaki, Rev. Sci. Instrum. 79 123117 (2008).
6. M. Zheng, E.F. Schwier, H. Iwasawa, K. Shimada, Chin. Phys. B 29, 067901 (2020).
7. X.Y. Cui, K. Shimada, Y. Sakisaka, H. Kato, M. Hoesch, T. Oguchi, Y. Aiura, H. Namatame, M. Taniguchi, Phys. Rev. B 82 195132 (2010).

Electronic Structure and H-T Phase Diagram of Eu(Fe_{1-x}Rh_x)₂As₂

Shaozhu Xiao^a, Darren C. Peets^a, Ya Feng^a, Wen-He Jiao^b, Eike F. Schwier^c, Kenya Shimada^c and Shaolong He^a,

^a*Ningbo Institute of Materials Technology and Engineering, Chinese Academy of Sciences, Ningbo, Zhejiang 315201, China*

^b*Department of Physics, Zhejiang University of Science and Technology, Hangzhou, Zhejiang 310023, China*

^c*Hiroshima Synchrotron Radiation Center, Hiroshima University, Higashi-Hiroshima 739-0046, Japan*

Keywords: ARPES, EuFe₂As₂, iron-based superconductor.

Superconductivity and magnetic order are normally antagonistic and often vie for the same unpaired electrons. More generally, the zero-field ground state of a superconductor with singlet pairing is perfectly diamagnetic, and magnetism within the material reduces the energy saved through pairing as the pair condensate is forced to adapt or compensate. Given the complex relationship between magnetism and high-temperature superconductivity, the interactions of magnetic order with these superconductors offers an important opportunity to shed light on the pairing in these systems, which remains among the greatest unsolved problems in condensed matter physics.

Doped EuFe₂As₂[1-3] offers a unique opportunity to study this interaction. It consists of high-temperature-superconducting FeAs layers, but the intermediate layer is a square lattice of magnetic Eu. The FeAs and Eu layers both order magnetically in the undoped parent material [1], but their magnetism is nearly decoupled [3,4]. Superconductivity can be induced by pressure [5] or by chemical substitution [6]. The latter can occur either on the Eu site, which frustrates the magnetic order while injecting charge carriers to the FeAs planes, or within the FeAs planes, which introduces disorder to the superconducting system but leaves the magnetic sublattice largely untouched. Doped EuFe₂As₂ has a number of very unconventional properties, including a reentrant superconducting transition in the resistivity [6] and a reentrant spin-glass phase [7], most likely as a result of the competition between superconductivity and magnetism.

The electronic structure of Eu(Fe_{0.88}Rh_{0.12})₂As₂ measured by ARPES with a helium lamp ($h\nu = 21.2$ eV) is displayed in Fig. 1. Figs. 1(a-d) show the Fermi surface and constant-energy contours at binding energies $E_b = 0, 20, 40$, and 60 meV taken at a temperature of 15 K, just below the critical temperature. Similar to EuFe₂As₂ with other dopants [8,9], there are hole pockets around the point and electron pockets around the M points. The band dispersions centered around the $\bar{\Gamma}$ point [along cut #1 in Fig. 1(a)] and M [along cut #2 in Fig. 1(a)] at different temperatures are shown in Figs. 1(e-h) and Figs. 1(i-l), respectively. Energy distribution curves (EDCs) are shown as a function of temperature at Fermi momenta near $\bar{\Gamma}$ and M in Figs. 1(m) and 1(n), respectively. Upon increasing temperature through the critical temperature T_c (from 15 to 50 K), no significant changes in the band structure can be observed around the $\bar{\Gamma}$ or M point, we do not observe a gap opening, and no features near the Fermi level EF can be unambiguously identified as coherence peaks. This is most likely a consequence of being too close to T_c .

To improve the energy resolution and avoid any inhomogeneity of the cleaved surface, laser-ARPES with a spot size below 5 μ m was also used to measure the band structure around the $\bar{\Gamma}$ point (Fig. 2 shows data at 13 K). Despite an energy resolution better than 5 meV, there are still no significant changes with temperature and no visible gap. A superconductor with a high transition temperature would normally have a sizeable gap, but this close to the transition temperature it would be very small. The lack of observable signatures of a pairing gap may also arise from space charge effects, which we cannot completely rule out in the laser-ARPES data, or Eu acting as a magnetic impurity. The pair-breaking induced by magnetic impurities can lead to “gapless superconductivity” [10, 11], a state which was discussed extensively in connection with BCS superconductors.

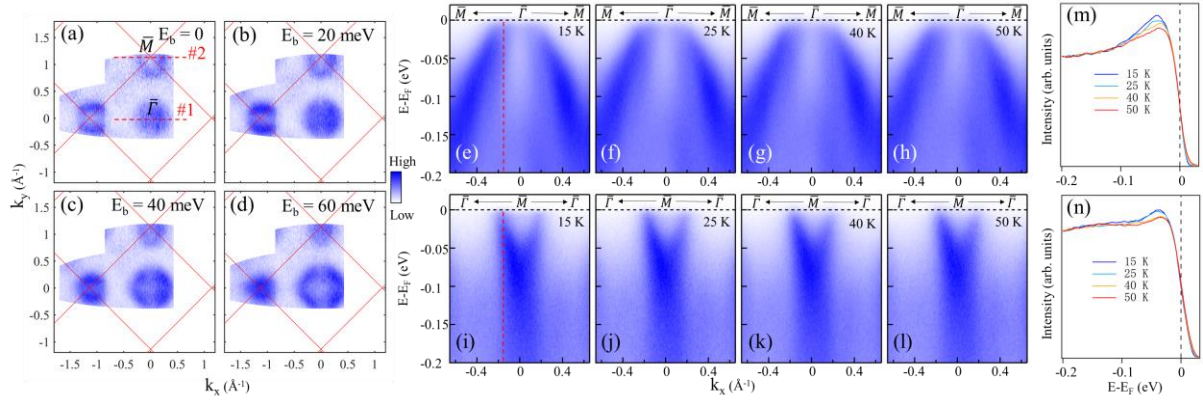


FIGURE 1. Electronic structure of $\text{Eu}(\text{Fe}_{0.88}\text{Rh}_{0.12})_2\text{As}_2$ measured by ARPES with a photon energy $h\nu = 21.2$ eV. (a-d) Constant energy contours at 15 K at different binding energies as labeled. (e-l) Energy-momentum images taken at different temperatures along the (e-h) $\bar{M} - \bar{\Gamma} - \bar{M}$ direction as indicated by dashed line #1 in (a), and (i-l) along the $\bar{\Gamma} - \bar{M} - \bar{\Gamma}$ direction as indicated by dashed line #2 in (a). (m) Temperature-dependent EDCs extracted from images (e-h) at the Fermi momentum of the hole pocket, shown by the dashed line in (e). (n) Temperature-dependent EDCs extracted from images (i-l) at the Fermi momentum of the electron pocket, identified by the dashed line in (i).

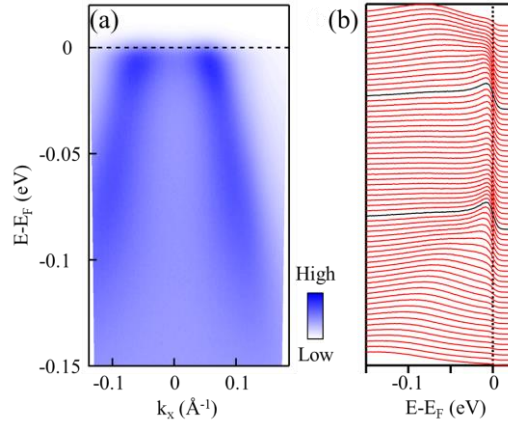


FIGURE 2. (a) Band structure of $\text{Eu}(\text{Fe}_{0.88}\text{Rh}_{0.12})_2\text{As}_2$ crossing the $\bar{\Gamma}$ point along the $\bar{M} - \bar{\Gamma} - \bar{M}$ direction measured by μ -laser ARPES ($h\nu = 6.3$ eV) at 13 K. (b) Energy distribution curves (EDCs) extracted from (a). EDCs at the Fermi momenta are plotted in black.

The band dispersion measured at 13 K in the s polarization geometry (electric field perpendicular to the plane of incidence) is shown in Fig. 2(a). This geometry will selectively detect d_{xy} and d_{yz} orbitals, for polarization along y with z being the surface normal. The difference in the Fermi wavevector k_F between Figs. 2(a) and 1(e-h) is mostly likely due to either k_z dispersion or differences in carrier doping at the surface — the material cleaves through the Eu charge reservoir layer. As seen more clearly in the EDCs shown in Fig. 2(b), there is a feature suggestive of a at band near the Fermi level, reminiscent of heavy fermion physics. Such a feature can arise from a at 4f band interacting with the regular electrons at low temperature (and having dipole symmetry that matches d_{xy} and d_{yz}), or it can appear when a band top or bottom is just above the Fermi level. A parabolic fit indicates that the top of the hole pocket at $\bar{\Gamma}$ should lie 30 meV above the Fermi level, and this apparent at band is most likely a tail from that band top, cut off by the Fermi function.

Based on specific heat and susceptibility measurements, an H-T phase diagram for $\text{Eu}(\text{Fe}_{0.88}\text{Rh}_{0.12})_2\text{As}_2$ is obtained and shown in Fig. 3. The phase diagram combines the results of our measurements on $\text{Eu}(\text{Fe}_{0.88}\text{Rh}_{0.12})_2\text{As}_2$ for both orientations. The antiferromagnetic transition has been expanded by a factor of 5. Aside from the inclusion of superconductivity, this phase diagram bears a very close resemblance to that of $(\text{Eu}_{0.88}\text{Ca}_{0.12})\text{Fe}_2\text{As}_2$ [12]. Such a high degree of similarity is surprising given that the dopants in the latter case are on the Eu site, disrupting the magnetic order, while here the Rh is in the superconducting FeAs planes, weakening the competing superconductivity.

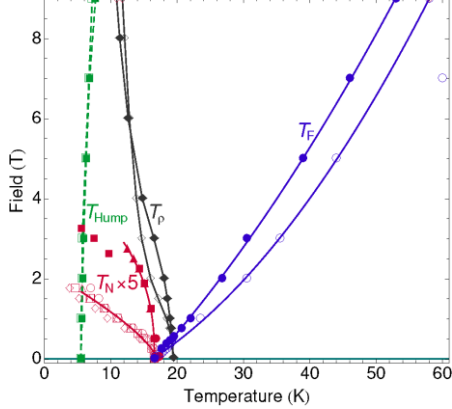


FIGURE 3. H-T phase diagram of $\text{Eu}(\text{Fe}_{0.88}\text{Rh}_{0.12})_2\text{As}_2$ obtained from our specific heat and susceptibility data. Filled symbols are for $H \parallel c$, and open symbols are for $H \perp c$; lines are guides to the eye. T_F represents field-induced ferromagnetism, T_{Hump} identifies the low-temperature hump in the specific heat, T_p marks the resistive superconducting transition, and T_N represents the bulk antiferromagnetic transition. T_N , which has been expanded by a factor of 5 for clarity, includes points based on the specific heat jump (triangles), susceptibility peak (squares), resistivity (diamonds), and susceptibility jump (circles).

In summary, the antagonistic relationship between the Eu and FeAs layers in EuFe_2As_2 disrupts both the long-range magnetic order and bulk superconductivity. The consequence for the magnetism is that the ground state can be tuned by doping the FeAs layers, likely disrupting the interlayer coupling, and our work indicates that the magnetism's H-T phase diagram can be traversed with laboratory magnets. The superconductivity may also be tunable — our data suggest that the FeAs layers may feel a strong field even under zero applied field. The upper critical fields in the iron-based superconductors are normally very high and difficult to access, but the EuFe_2As_2 family may make the high-field region far more accessible. In particular, ARPES is a strictly zero-field technique due to the immediate destruction of momentum information by any applied magnetic field, so field-dependent ARPES is ordinarily completely impossible. Our results suggest that in the EuFe_2As_2 system, ARPES can be performed at a higher effective magnetic field. Tuning the magnetic layers, for instance by Ca or Sr doping, should return the system to lower effective field, allowing an effective-magnetic-field-dependent ARPES study and directly accessing the electronic structure under conditions that are ordinarily inaccessible to ARPES.

REFERENCES

1. H. Raffius et. al., J. Phys. Chem. Solids **54**, 135 (1993).
2. Z. Ren et. al., Phys. Rev. B **78**, 052501 (2008).
3. H. S. Jeevan et. al., Phys. Rev. B **78**, 052502 (2008).
4. Y. Xiao et. al., Phys. Rev. B **80**, 174424 (2009).
5. K. Matsubayashi et. al., J. Phys.: Conf. Ser. **215**, 012187 (2010).
6. W.-H. Jiao et. al., Supercond. Sci. Technol. **30**, 025012 (2017).
7. A. Baumgartner et. al., Phys. Rev. B **95**, 174522 (2017).
8. S. Thirupathaiah et. al., Phys. Rev. B **84**, 014531 (2011).
9. M. Xia et. al., J. Phys.: Condens. Matter **26**, 265701 (2014).
10. A. A. Abrikosov and P. Gor'kov, Soviet Physics JETP **12**, 1243 (1961).
11. J. C. Phillips, Phys. Rev. Lett. **10**, 96 (1963).
12. L. M. Tran et. al., Phys. Rev. B **98**, 104412 (2018).

Direct Band Structure Study of Magnetic Weyl Semimetal Candidate V_3S_4 Using ARPES

Xiao-Ming Ma, Yu-Jie Hao, Yue Feng, Chunsheng Zhou and Chang Liu

Shenzhen Institute for Quantum Science and Engineering (SIQSE) and Department of Physics, Southern University of Science and Technology (SUSTech), Shenzhen 518055, China.

Keywords: Magnetic Weyl Semimetal, Angle-Resolved Photoemission Spectroscopy, V_3S_4 .

Topological semimetals received explosive research interest due to their novel dispersion relation analogous to k-space magnetic monopoles, and the associated exotic transport behaviors that lead to possible spintronic applications [1-6]. Thereinto, Weyl semimetals are semimetals or metals whose quasi-particle excitations is the Weyl fermion. Before the experimental discovery of the Weyl semimetallic phase in TaAs [5, 6], it is theoretically proposed that this phase can occur in circumstances where the time reversal symmetry is broken instead of the crystallographic inversion symmetry [3, 4]. Topological semimetals with non-collinear magnetic order is first discussed in the pyrochlore iridates [3], but experimental evidences for magnetic Weyl semimetals have yet to be found. Recently, Kapildeb Dolui and Tanmoy Das proposed several families of Weyl orbital semimetals. According to their calculation results, the existing V_3S_4 compound is a promising magnetic Weyl semimetal candidate and may host novel electronic structure. Therefore, we use the high-resolution angle-resolved photoemission spectroscopy (ARPES) setups at BL-1, HiSOR to investigate the V_3S_4 system.

Single crystals of V_3S_4 are grown by the chemical vapor transport (CVT) method, and the size of the single crystal are $\sim 3 \times 1 \times 0.5$ mm³. The purity and lattice structure of the grown samples are confirmed by X-ray diffraction (XRD) measurement [see Fig. 1 (a)]. The V_3S_4 has a hexagonal phase in space group of P 63/m (No.176) with $a = 9.104$ Å and $c = 3.0973$ Å. We have carried out the general band measurement on V_3S_4 at BL-01. The cleaved surface of the crystal is give in Fig.1 (b). Due to the 3 dimensional crystal structure of V_3S_4 , the cleaved surface surface is not very flat. We were still able to do a constant energy contours measurement. The constant energy contours mapping results collected with 80 eV photon are presented in Fig. 2.

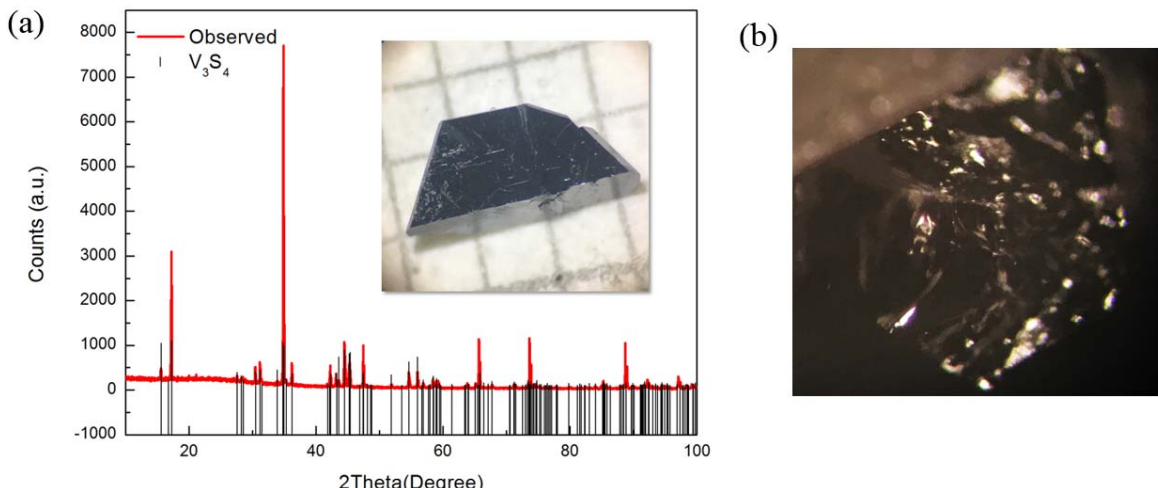


FIGURE 1. (a) XRD result of V_3S_4 single crystal powder. The inset is a picture of V_3S_4 crystals in size around 3 mm prepared by CVT method. (b) The picture of the cleaved surface of V_3S_4 .

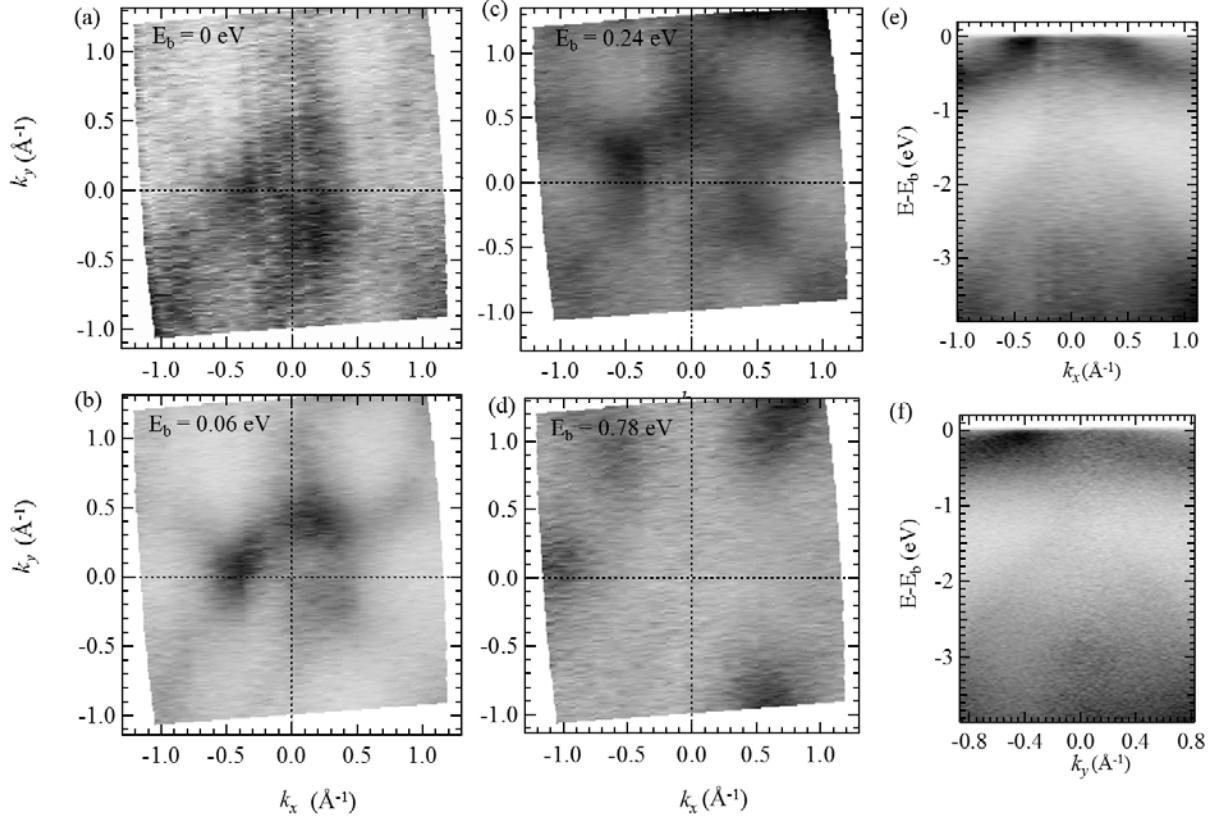


FIGURE 2. ARPES results of V_3S_4 . (a) - (d) are the constant energy contours results with indicated E_b . (e) and (f) are the k - E cuts accross the $(0, 0)$ position along the x and y directions, respectively.

As shown in Fig. 2 (b) to (d), the mapping patterns appear hexagonal symmetry, which consists with the symmetry of the $(00l)$ surface of the V_3S_4 . We also intercepted two k - E cuts along the x and y directions pass the Γ position at $(0, 0)$. Our ARPES results suggests that the V_3S_4 is in metallic state. At the Fermi suface of the Γ position, there is an hole pocket.

In all, we have not found the predicated features of the Weyl Semimetal this time. We need more beamline time to do further more systematically mesurments on V_3S_4 .

REFERENCES

- 1 H. Johnston, Physics World (2015).
- 2 L. Balents, Physics 4, 36 (2011).
- 3 X. Wan, A. M. Turner, A. Vishwanath, and S. Y. Savrasov, Phys. Rev. B 83, 205101 (2011).
- 4 A. A. Burkov and L. Balents, Phys. Rev. Lett. 107, 127205 (2011).
- 5 S.-Y. Xu et al., Science 349, 613 (2015).
- 6 B. Q. Lv et al., Phys. Rev. X 5, 031013 (2015).

Observation of topological surface state in palladium-bismuth superconductor

M. Sakano^a, Y. Kubota^a, K. Okawa^b, K. Sumida^c, E. F. Schwier^c, K. Shimada^c, T. Okuda^d, T. Sasagawa^b, and K. Ishizaka^{a,e}

^a*Quantum-Phase Electronics Center (QPEC) and Department of Applied Physics, The University of Tokyo, Bunkyo-ku, Tokyo, 113-8656, Japan*

^b*Materials and Structures Laboratory (MSL), Tokyo Institute of Technology, Yokohama, Kanagawa, 226-8503, Japan.*

^c*Graduate School of Science, Hiroshima University, Higashi-Hiroshima, Hiroshima, 739-8526, Japan*

^d*Hiroshima Synchrotron Radiation Center (HiSOR), Hiroshima University, Higashi-Hiroshima, Hiroshima, 739-0046, Japan*

^e*RIKEN Center for Emergent Matter Science (CEMS), Wako, Saitama, 351-0198, Japan*

Keywords: Topological surface state, spin-resolved ARPES

Topological superconductors are a peculiar class of superconductors defined by the nonzero topological invariant of bulk wave functions. On their surfaces (or edges), Majorana fermions, which are their own antiparticles, obeying non-Abelian statistics can emerge as a topologically protected zero-energy excitation in the gapless Andreev surface states and enable an naturally fault-tolerant topological quantum computing [1, 2]. One of the strategies to realize topological superconductivity in condensed matter systems is to utilize the coexistence of the two-dimensional helical spin states and the proximity-induced *s*-wave superconductivity [3].

In this study, we investigate the spin and electronic structures of a superconductor α -PdBi₂ ($T_c = 1.7$ K) [4,5] in detail, which is a candidate topological superconductor, by the spin-resolved angle-resolved photoemission spectroscopy (SARPES) performed at BL-9B of HiSOR and photon-energy-($h\nu$)dependent ARPES at BL-1 of HiSOR. Recently, the first principles calculation [6] and ARPES [5] studies have demonstrated the surface band dispersions in the α -PdBi₂. Some of them are well isolated from the bulk bands crossing the Fermi level. However, the topological nature of these bands is still unrevealed.

The clear ARPES image recorded along the k_x direction is obtained for the single crystalline α -PdBi₂ as shown in Fig. 1(a). We perform the SARPES measurement for the regions represented by the purple linens (A1-A18) in Fig.1(a). The SARPES results are shown Fig. 1(b) for the A1-A11 and 1(c) for the A12-A18. The spin y components, which is reversed with respect to the time-reversal invariant momenta $\bar{\Gamma}$ -point (A4) and \bar{A} -point (A15), are clearly observed as indicated by the red (spin up) and blue (down) colored circular markers above the peak positions of the SARPES spectra. The observed peak positions are overlaid on the ARPES image in Fig. 1(a). Significantly, the markers overlap just on the particular bands, some of which cross the Fermi level. Because the bulk bands in a material with the inversion symmetry are spin degenerate, it indicates that the spin-polarized surface states are realized in the superconductor α -PdBi₂.

To confirm the two-dimensionality for the observed spin-polarized bands, we performed the photon-energy-($h\nu$ -) dependent ARPES, which can measure the band dispersion along the k_z direction perpendicular to the surface of sample. The $h\nu$ -dependent momentum distribution curves ($h\nu = 90\text{-}63$ eV) are shown in Figs. (e)-(h). The measured regions are represented by the red, orange, green, and blue colored cuts on the ARPES images recorded by $h\nu = 84$ eV in Fig. 1(d), respectively. The broken lines clearly show that the peak positions of the momentum distribution curves are independent on the photon energy. Thus, since the observed surfaces states do not show any k_z dispersions, we have concluded that the spin-polarized surface states, some of which cross the Femi level, are realized in the superconductor α -PdBi₂.

In addition, further calculational studies have proceeded to determine whether the bulk electronic structure in the α -PdBi₂ is topologically nontrivial or trivial. It concludes that the observed surface states are topologically protected surface states, possibly leading to the topological superconductivity.

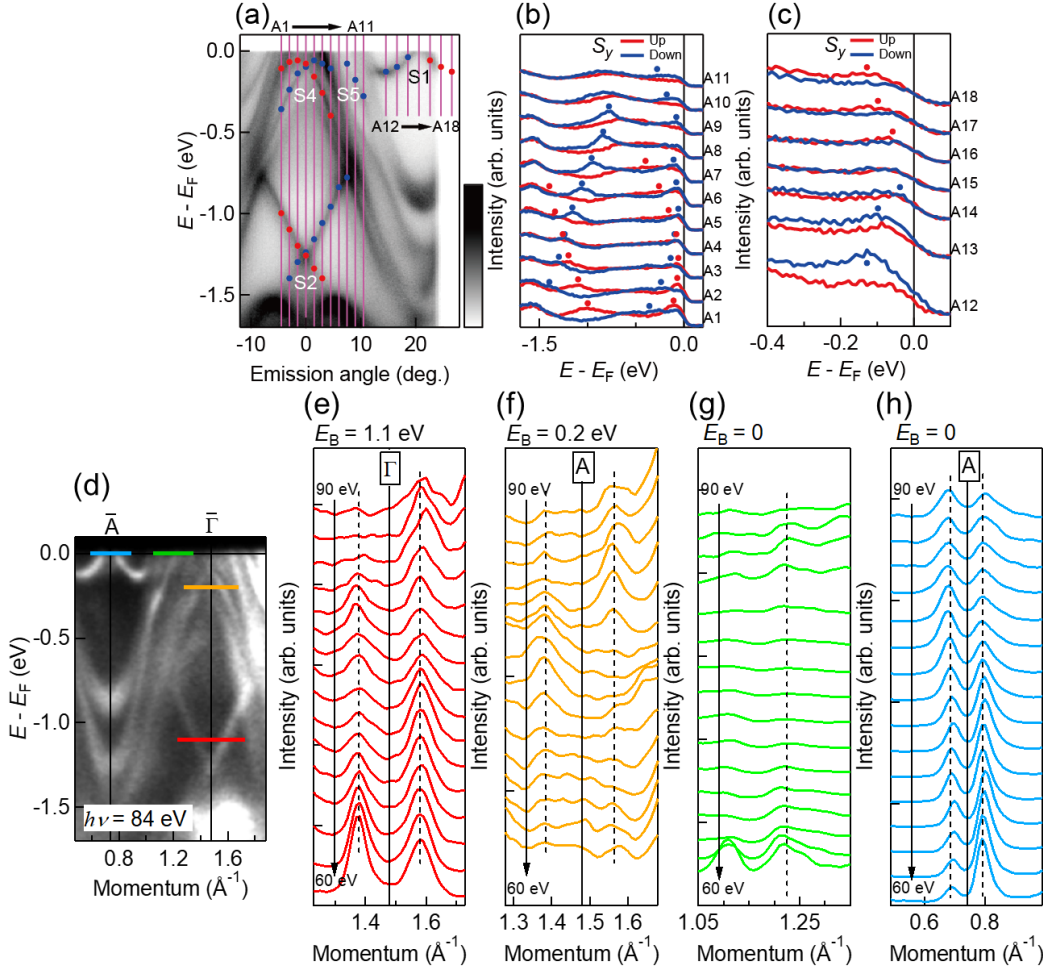


FIGURE 1. (a) ARPES image recorded by HeI α light source ($h\nu = 21.2$ eV) with respect to the emission angle of the photoelectron along the k_x direction. The purple lines A1–A11 and A12–A18 represent the measurement cuts for the spin-resolved ARPES spectra in (b) and (c), respectively. The red and blue circles indicate the peak positions in (b) and (c). Hereafter, red (blue) indicates the spin-up (down) component. (b), (c) Spin-resolved spectra for A1–A11 and A12–A18 lines in (a) for the spin magnetic moments along the y direction, respectively. The circular markers indicate the peak positions. (d) ARPES image recorded by $h\nu = 84$ eV along the k_x direction. The red, orange, green and blue lines indicate the measured momentum cuts for the $h\nu$ -dependence of ARPES spectra shown in (e)–(h), respectively. (e)–(h) The $h\nu$ -dependence of ARPES spectra recorded by synchrotron light source of $h\nu = 90$ –60 eV. The broken lines indicate the photon-energy-independent peak positions for the surface states.

To summarize, the combination of the SARPES and hn-dependent ARPES has clarified that the two-dimensional spin-polarized surface states, some of which are cross the Fermi level, are realized in the superconductor α -PdBi₂. This result indicates that the α -PdBi₂ is likely to be an ideal electronic structure to realize the topological superconductivity accompanying the Majorana Fermions in the vortices.

REFERENCES

1. C. Nayak *et al.*, Rev. Mod. Phys. **80**, 1083 (2008).
2. A. Y. Kitaev, Ann. Phys. (N.Y.) **303**, 2 (2003).
3. L. Fu and C. L. Kane Phys. Rev. Lett. **100**, 096407 (2008).
4. N. N. Zhuravlev, Zh. Eksp. Teor. Fiz. **32**, 1305 (1957).
5. K. Dimitri *et al.*, Phys. Rev. B **97**, 144514 (2018).
6. H. Choi *et al.*, Phys. Rev. Mater. **1**, 034201 (2017).

Band Structures of Cubic PtBi₂ studied by ARPES

Ya Feng^a, Shaolong He^a, Shaozhu Xiao^a and Baojie Feng^b

^a*Ningbo Institute of Materials Technology and Engineering,*

Chinese Academy of Sciences, Ningbo 315201, China

^b*Institute of Physics, Chinese Academy of Sciences, Beijing 100190, China*

Keywords: Dirac semimetal, PtBi₂, XMR, band structure.

Recently, Dirac semimetals and Weyl semimetals have attracted much attention. The low energy electrons in these materials behave like Dirac fermions without effective mass, which can be considered as 3D “graphene” with linear band dispersion for all momentum directions. On the one hand, Dirac semimetals can be evolved into Weyl semimetals after time inversion symmetry breaking or space inversion symmetry breaking. On the other hand, if the gap opens at the Dirac points with strong spin-orbital interactions, Dirac semimetals will become topological insulators. So the Dirac semimetal is an ideal platform for realizing different states of topological quantum matter. However, until now, only a few of Dirac semimetals are experimentally realized such as Na₃Bi[1-2], Cd₃As₂[3-4], and so on.

Moreover, there are peculiar quantum phenomena such as very large non-saturating magnetoresistance (MR) and ultra-high carrier mobility in most of Dirac semimetals and Weyl semimetals. Such large non-saturating magnetoresistance phenomenon in nonmagnetic materials has arisen much interest due to both their potential applications and the novel physical mechanism. So discovering new Dirac materials with unique quantum properties has become more and more important in both condensed matter physics and material science.

PtBi₂ has different phases such as hexagonal and cubic structures both of which have been experimentally detected with extremely large unsaturated magnetoresistance (XMR) [5-6]. What's more, the cubic structure of PtBi₂ has been theoretically predicted to be a new 3D Dirac semimetal (DSM) [7]. By measuring the band structures of PtBi₂ with ARPES, we can confirm whether it is a Dirac semimetal, which is helpful to study the origin of XMR in this material.

Figure 1 shows the Fermi surface of cubic PtBi₂ measured on BL-1 with $h\nu=35\text{eV}$. The theorist predicted that there were two Dirac cones along Γ -M direction. We measured the bands along Γ -M direction using different photon energies, from $h\nu=35\text{eV}$ to $h\nu=85\text{eV}$. However, we didn't observe the Dirac cones unfortunately. Figure 2 shows the compare of experimental data (left) and theoretical data (right). The Dirac cones predicted by theorists are shown in right highlighted by green circles. We can see clearly that there are no band structures at the same position for the experimental data (left). The data under other photon energies are the same as the one in Figure 2.

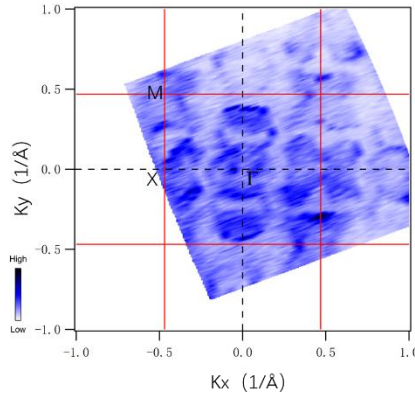


FIGURE 1. The Fermi surface of cubic PtBi₂ measured on BL-1 with $h\nu=35\text{eV}$.

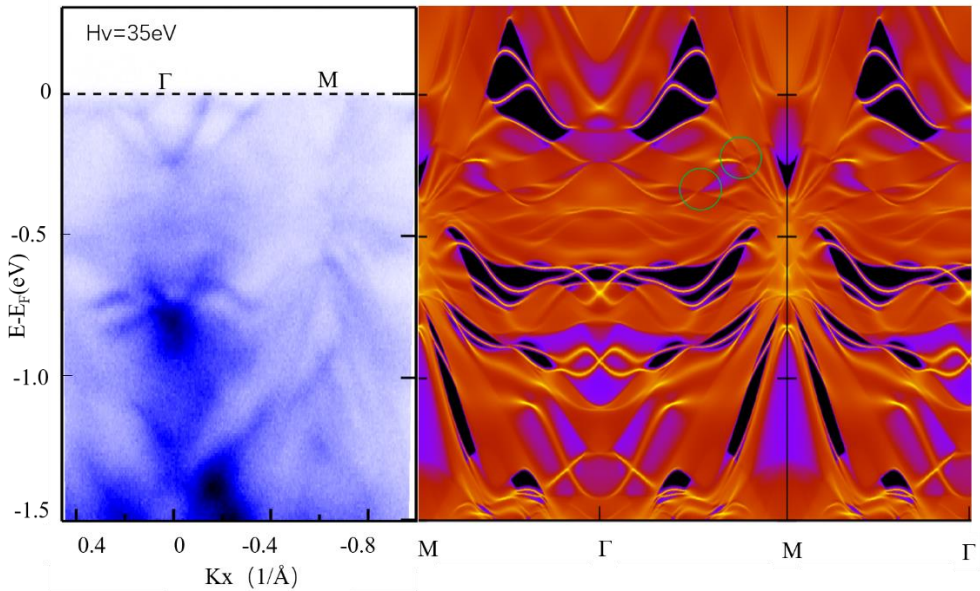


FIGURE 2. Bands along Γ -M direction measured by ARPES (left) and calculated by theorists (right). The green circles point to two Dirac cones (right).

In summary, we measured band structures of cubic PtBi_2 under different photon energies. Unfortunately, we didn't observe the predicted Dirac cones. More efforts on experiments will be needed in the future.

REFERENCES

1. Zhijun Wang, et al. PHYSICAL REVIEW B 85, 195320 (2012)
2. Z. K. Liu, et al. Science Express, January 16 (2014)
3. Zhijun Wang, et al. PHYSICAL REVIEW B 88, 125427 (2013)
4. Z. K. Liu, et al. Nature Materials volume 13, pages677–681(2014)
5. Xiaojun Yang, et al. Appl. Phys. Lett. 108, 252401 (2016)
6. Wenshuai Gao, et al. Phys. Rev. Lett. 118, 256601 (2017)
7. Q. D. Gibson , et al. Phys. Rev. B 91, 205128 (2015)

Changing Band Alignment with Adsorbed Palladium on MoS₂ and WSe₂

Takashi Komesu^a, Eike F. Schwier^b, Prescott E. Evans^a, Shiv Kumar^b, Kenya Shimada^b, and P. A. Dowben^a

^aDepartment of Physics and Astronomy, Nebraska Center for Materials and Nanoscience, Theodore Jorgensen Hall, 855 N 16th, University of Nebraska, 880299, Lincoln, NE 68588-0299, U.S.A.

^bHiroshima Synchrotron Radiation Center, Hiroshima University, Higashi-Hiroshima 739-0046, Japan

Keywords: High Resolution Angle Resolved Photoemission Spectroscopy, band bending, contacts to transition metal dichalcogenides.

Palladium has been seen to be a more efficient contact for hole injection into WSe₂ [1,2]. In this context, the extent band bending at the interface between the transition metal dichalcogenide and the contact metal palladium is key.

After performing *in situ* cleaving of MoS₂ and WSe₂ bulk crystals, the occupied valence electronic states of TMDs systems before and after Pd deposition were measured by

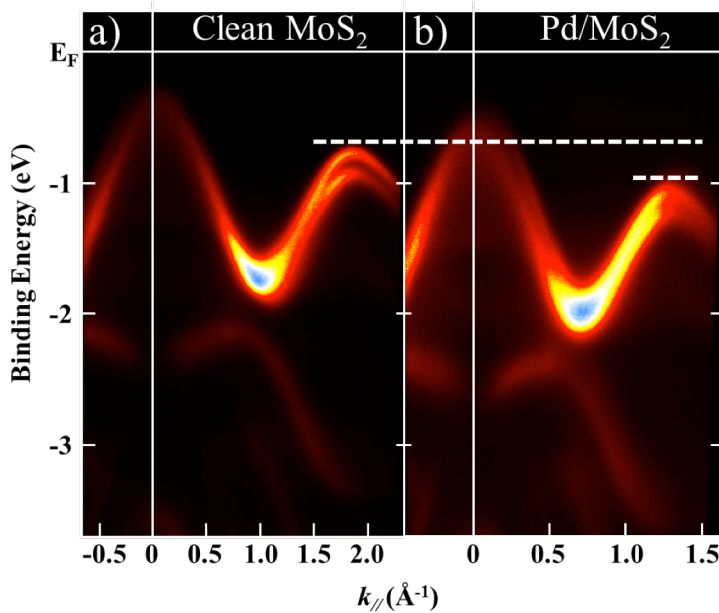


Figure 1. Valence band measurement spectra of MoS₂ before (a), and after (b), palladium deposition on the surface, here the dotted line highlights the shift of occupied states towards higher binding energies. Binding energies are denoted as $E - E_F$.

semiconductor was also found for Na adsorption on MoS₂(0001) [3,4]. On the other hand, Pd deposition on the WSe₂(0001) surface, as shown in Figure 2, leads to a shift of the top of valence band towards the Fermi level. There is a decrease in the band bending near the WSe₂(0001) surface to a band placement more characteristic of a p-type semiconductor. This was also found for Co metal adsorption on WSe₂(0001) [4].

high-resolution angle-resolved photoemission spectroscopy (ARPES) at the linear undulator beamline (BL-1) at HiSOR, Hiroshima University in Japan, as detailed elsewhere [13,14]. All measurements were taken at a photon energy of $h\nu = 34$ eV, with p-polarized light along the $\bar{F} - \bar{K}$ direction of the surface Brillouin zone. Submonolayer Pd deposition was accomplished through use of an e-beam evaporator.

Pd deposition on the MoS₂(0001) surface, as shown in Figure 1, leads to a shift of the top of valence band away from the Fermi level (E_F). This decrease in the band bending near the surface, upon metal adsorption, to a band placement more characteristic of an n-type

The changes in band alignment of the WSe₂(0001) valence bands, inferred from angle-resolved photoemission (Figure 2) is schematically indicated in Figure 3 for before and after palladium deposition. These band shifts are very consistent with a substantive decrease to the barrier to hole injection into WSe₂(0001) and a validation of the metal to WSe₂ interface band models proposed to explain the origin of Pd as efficient contact for hole injection [1,2].

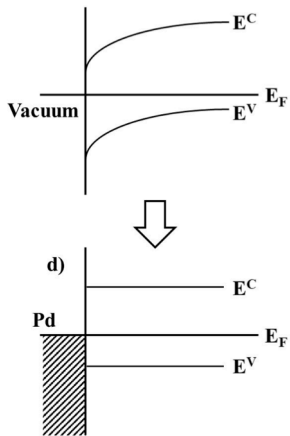


Figure 3. A schematic diagrams of the band realignment after palladium deposition on nominally p-type WSe₂(0001)

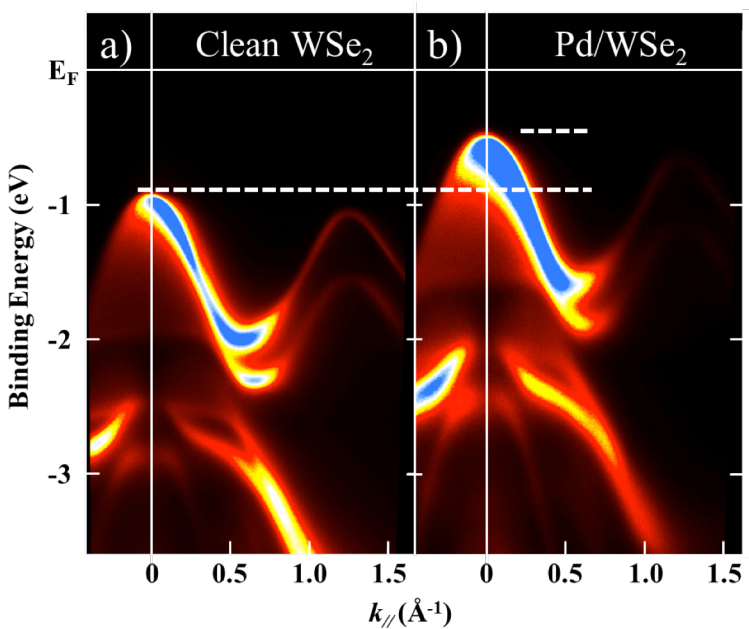


Figure 2. Valence band measurement spectra of WSe₂ before (a), and after (b), palladium deposition on the surface. Here again, the dotted line highlights the shift of occupied states towards lower binding energies. Binding energies are denoted as $E - E_F$.

These results are generally expected as Pd is a large work function metal (with a work function (W_M) in the region of 5.55 eV to 5.95 eV and WSe₂ is a p-type semiconductor. As MoS₂ is generally an n-type semiconductor, we would expect that Pd would be a blocking contact.

References

- [1] H. Fang, S. Chuang, T. C. Chang, K. Takei, T. Takahashi, and A. Javey, *Nano Lett.* **12**, 3788–3792 (2012).
- [2] S. Das J. Appenzeller, *Appl. Phys. Lett.* **103**, 103501 (2013).
- [3] T. Komesu, D. Le, X. Zhang, Q. Ma, E. F. Schwier, Y. Kojima, M. Zheng, H. Iwasawa, K. Shimada, M. Taniguchi, L. Bartels, T. S. Rahman and P. A. Dowben, *Appl. Phys. Lett.* **105**, 241602 (2014)
- [4] T. Komesu, D. Le, I. Tanabe, E. F. Schwier, Y. Kojima, M. Zheng, K. Taguchi, K. Miyamoto, T. Okuda, H. Iwasawa, K. Shimada, T. S. Rahman and P. A. Dowben, *J. Phys. Cond. Matter* **29**, 285501 (2017)

Resonance photoemission study of the energy gap open at the Dirac point and the reasons of the gap formation in Gd-doped magnetic topological insulators

D.A. Estyunin^a, A.M. Shikin^a, E.F. Schwier^b, S. Kumar^b and A. Kimura^c

^aSaint-Petersburg State University, Saint-Petersburg, Russia

^bHiroshima Synchrotron Radiation Center, Hiroshima University, Hiroshima 739-0046, Japan

^cDepartment of Physical Sciences, Graduate School of Science, Hiroshima University, Hiroshima 739-8526, Japan

Keywords: Magnetically doped topological insulators.

Recent exciting observation of the Majorana particles in topological insulator-based structure [1] promises the realization of the topologically protected qubits and efficient quantum computations. The key element for these effects is magnetically doped TI in Quantum Anomalous Hall regime. For this case magnetic metals-doping leads to breaking of the time-reversal symmetry and opening the energy gap at the Dirac point. In numerous works transition metals doping was applied for this purpose. [2,3] However, until now, magnetic ordering in topological insulators has been observed only below 20K, temperatures too low for any large-scale application. Moreover, transition metals act as not only magnetic dopants but also electric dopants because they are usually divalent. This problem can be solved by the rare-earth metals doping of TIs in stead of transition metals. In Refs. [4,5] theoretical calculations and magnetic measurements predict a robust QAH phase in Gd-doped bismuth telluride. Moreover, among the rare-earth elements, Gd has large magnetic moment with half-filled 4f shell.

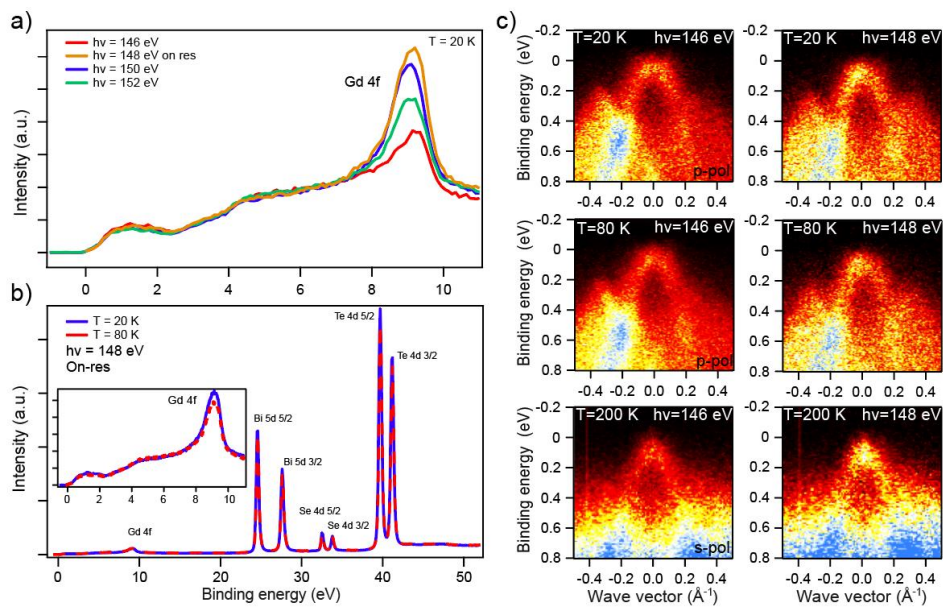


FIGURE 1. In the panel (a) spectra for photon energies 146 eV, 148 eV, 150 eV and 152 eV are presented. The peaks correspond to Gd 4f level. Here resonant energy is 148 eV. Panel (b) shows core levels of $\text{Gd}_{0.06}(\text{Bi},\text{Sb})_{1.94}\text{Te}_3$, measured with $h\nu=148$ eV at $T=20$ K (blue line) and $T=80$ K (red line). In the inset the region between the Fermi level and Gd 4f level is shown closer. Panel (c) demonstrates the valence band measured at 146 eV (off resonance) and 148 eV (on resonance) for different temperatures $T=20$, 80 and 200 K.

A question about an origin of the energy band gap at the Dirac point in magnetically doped TIs remains to be open. In Refs [6,7] a possibility of non-magnetic gap at the Dirac point in Mn-doped TIs related to avoided-crossing effects due to hybridization between the DC states and impurity d-states was discussed.

Actual project was devoted to comparative ARPES analysis of the Dirac cones in topological insulators $(\text{Bi},\text{Sb})_2\text{Te}_3$ doped with rare-earth metal (Gd). Resonant photoemission spectroscopy has been used to match the location and contribution of the bands of the magnetic impurities. Hereby it gives information of their bonding with atoms of TI. We analyzed temperature dependence of Gd f-states density in the valence band and the topological surface states for the purpose of understanding 2D surface magnetism. Based on these experimental measurements we have examined influence of the Gd states in the valence band on the band gap opening in magnetically doped TIs.

For the studing of the influence of magnetic impurities on TIs we measured samples $(\text{Bi},\text{Sb})_2\text{Te}_3$ doped with 6% concentration of Gd. For the QAHE realization TI should possess band gap at the Fermi level. From our previous studies we found out that required stoichiometry is $\text{Bi}_{1.09}\text{Sb}_{0.85}\text{Gd}_{0.06}\text{Te}_3$. In the fig.2 spectra measured at photon energies around Gd 4d adsorption level are presented. From the fig.2.a one can see that intensity of the Gd 4f level increases at the photon energy of 148 eV, which correspond to the Gd 4d level (Gd 4d-4f resonance). With lower (146 eV) and higher (150 eV and 152 eV) photon energies intensity of the Gd 4f level appears lower. Spectra of the core levels are shown in the fig.2b. Blue and red spectra were measured at 20 K and 80 K correspondently. One can clearly see that both curves looks sufficiently similar. Though small difference in intensity of the Gd 4f level is presented for $T=20$ K and $T = 80$ K (see inset). Nevertheless, the same mismatch was observed for another core levels, which may be related to spectra normalization. Here we use normalization to the background away from spectral components. With higher temperatures intensity of the background can increase due to rise of electron scattering. Therefore, ratio between background and peaks intensity can be not constant. In fig.2c band maps of the valence band and the Dirac cone are shown. Spectra in the left column were measured with photon energy of 146 eV (off resonance) and in the right column with 148 eV (on resonance). Each line corresponds to various temperatures of 20, 80 and 200 K. The intensity of the valence band significantly increases on resonance. It is important to notice that intensity increase evenly along the valance band states and no impurity levels appears.

In conclusion, we study Gd influence on electronic structure of $\text{Bi}_{1.09}\text{Sb}_{0.85}\text{Gd}_{0.06}\text{Te}_3$ topological insulator by means resonant photoemission spectroscopy. From our preliminary results estimated size of the Dirac point band gap was about 25 – 40 meV. Here we observed availability of Gd states in the valence band without any impurity band at the Fermi level. Therefore, mechanism of the band gap opening due to hybridization less plausible than mechanism with breaking of time reversal symmetry.

REFERENCES

1. Q.L. He, L. Pan, A.L. Stern et al., “Chiral Majorana fermion modes in a quantum anomalous Hall insulator-superconductor structure”, *Science* 357, 294 (2017)
2. A. M. Shikin, A. A. Rybkina, D. A. Estyunin et al., “Signatures of in-plane and out-of-plane magnetization generated by synchrotron radiation in magnetically doped and pristine topological insulators”, *PRB* 97, 245407 (2018)
3. I. I. Klimovskikh, A. M. Shikin, M. M. Otrakov et al., “Giant Magnetic Band Gap in the Rashba-Split Surface State of Vanadium-Doped BiTeI: A Combined Photoemission and Ab Initio Study”, *Scientific Reports* 7, 3353 (2017)
4. J. Kim, K. Lee, T. Takabatake et al., “Magnetic Transition to Antiferromagnetic Phase in Gadolinium Substituted Topological Insulator Bi₂Te₃”, *Scientific Reports* 5, 10309 (2015)
5. Hai-Jun Zhang, Xiao Zhang, Shou-Cheng Zhang, “Quantum Anomalous Hall Effect in Magnetic Topological Insulator GdB₂Te₃”, *ArXiV*, arXiv:1108.4857 (2011)
6. J. Sánchez-Barriga, A. Varykhalov, G. Springholz et al., “Nonmagnetic band gap at the Dirac point of the magnetic topological insulator (Bi_{1-x}Mn_x)₂Se₃”, *Nature Commun.* 7, 10559 (2016)
7. R.R. Biswas and A. V. Balatsky , “Impurity-induced states on the surface of three-dimensional topological insulators”, *PRB* 81, 233405 (2010)

Exchange vs. spin-orbit interaction at magnet/heavy-metal interfaces

Marcel Holtmann^a, Pascal J. Grenz^a, Shiv Kumar^b, Eike F. Schwier^b,
Koji Miyamoto^b, Taichi Okuda^b and Markus Donath^a

^a*Physikalisches Institut, University of Münster, Wilhelm-Klemm-Straße 10, 48149 Münster, Germany*
^b*Hiroshima Synchrotron Radiation Center, University of Hiroshima, Higashi-Hiroshima 739-0047, Japan*

Keywords: ARPES, Cobalt, Tungsten, Electronic structure, Dirac-cone-like surface state.

The surface of W(110) exhibits a topologically nontrivial Dirac-cone-like surface state (DSS) within a spin-orbit-induced symmetry gap [1, 2]. When depositing ultrathin Fe films, the state was found to behave differently depending on the film thickness, allowing for manipulation of the "Dirac-fermion mass" via magnetic influence [3]. In order to systematically study the impact of the magnetic adsorbate material, we have investigated the influence of cobalt on the occupied band structure of W(110) by means of angle-resolved photoelectron spectroscopy (ARPES) at BL-1 and spin- and angle-resolved photoelectron spectroscopy (SARPES) at BL-9B.

Figure 1a shows ARPES measurements of different Co coverages on W(110) obtained with linear *p*-polarized synchrotron radiation of 43 eV photon energy. In Fig. 1b, the second derivatives of the data are displayed. In order to trace the position of the Dirac point, we have schematically extracted the dispersion of the DSS in the vicinity of the Dirac Point, which is shown in Fig. 1c. From this, we conclude that the DSS gradually shifts towards higher binding energies by up to about 120 meV at a coverage of less than 0.5 Co monolayers. With further Cobalt deposition, the DSS fades away until it is no longer visible (not shown here).

A SARPES measurement for 0.7 monolayers of Co on W(110) at a sample temperature of 53 K, conducted at BL-9B using *p*-polarized light with a photon energy of 43 eV, is shown in Fig. 2. Spin-resolved spectra were taken symmetrically with respect to the Γ point and are shown in Fig. 1b and Fig. 1c. The quantization axis of the measured spin polarization coincides with the Rashba direction and the direction of the easy magnetization axis. However, we do not expect any ferromagnetic order at the given coverage and temperature.

At a binding energy of about 1.0 eV, we identify the typical spin-polarization pattern of the DSS, i.e., asymmetric with respect to the Γ Point. Towards lower binding energies, at about 0.7 eV and 0.55 eV, we observe a pair of Rashba-type spin polarized electronic states, which are highlighted by black arrows. We attribute these states to the influence of the Cobalt adatoms.

REFERENCES

1. K. Miyamoto *et al.*, Phys. Rev. Lett. **108**, 066808 (2012).
2. D. Thonig *et al.*, Phys. Rev. B **94**, 1155132 (2016).
3. K. Honma *et al.*, Phys. Rev. Lett. **115**, 266401 (2015).

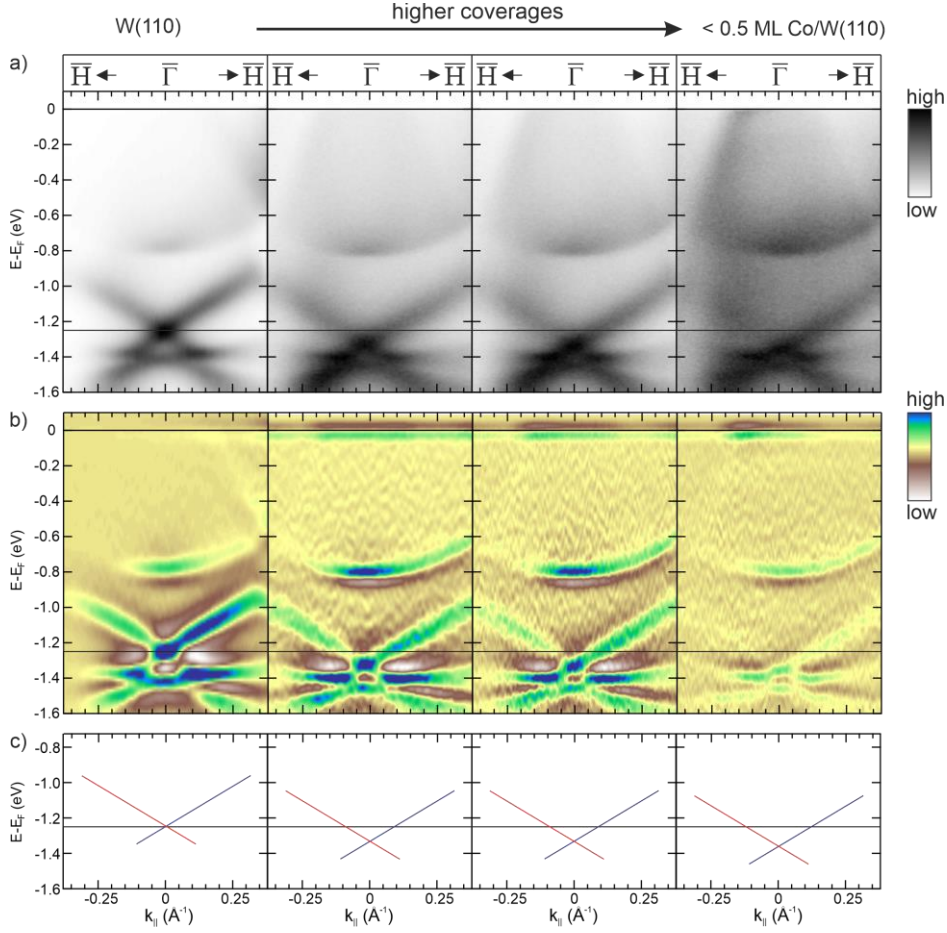


Figure 1. (a) ARPES measurements for ultrathin Co films on W(110) along Γ H at $T=23\text{K}$. (b) Second derivative of the data of Fig. 1a. (c) Position of the Dirac point (schematically).

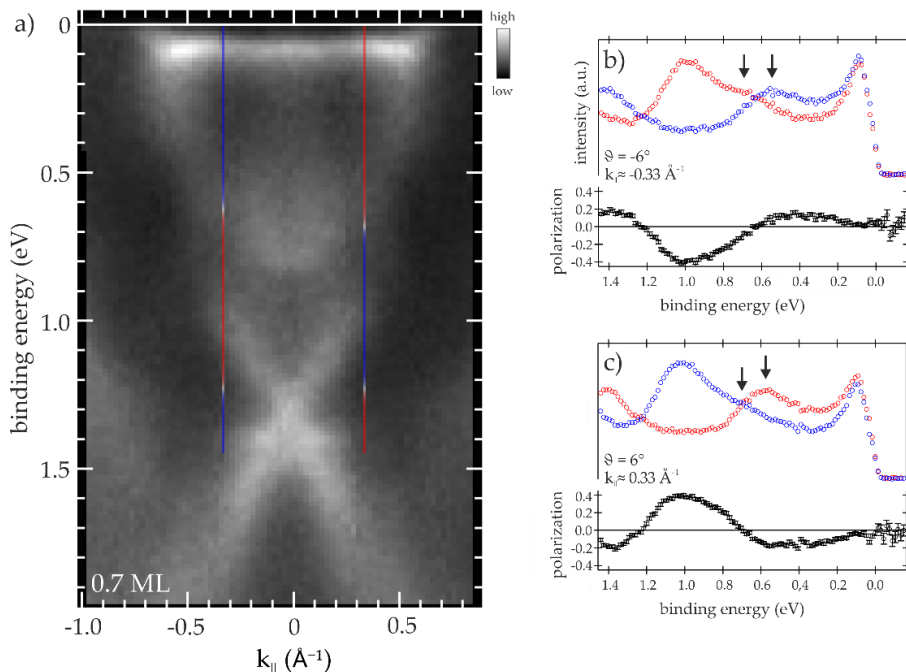


Figure 2. ARPES and SARPES measurements of 0.7 monolayers of Co on W(110) along Γ H at $T=53\text{K}$. The spin-resolved measurements in b) and c) are sensitive to the Rashba direction.

Angle-resolved Photoelectron Spectroscopy Study of (Ce,La)Ru₂Al₁₀

H. Yamaoka^a, H. Tanida^b, E. F. Schwier^c, S. Kumar^c, M. Arita^c,
and K. Shimada^c,

^aRIKEN SPring-8 Center, Sayo, Hyogo 679-5148, Japan

^bToyama Prefecture University, Imizu, Toyama 939-0398, Japan

^cHiroshima Synchrotron Radiation Center, Hiroshima University, Higashi-Hiroshima, Hiroshima 739-0046, Japan

Keywords: electronic structure, photoelectron spectroscopy, Ce1-2-10, hybridization

Ternary intermetallic compounds of CeM₂Al₁₀ ($M = \text{Ru, Os, Fe}$) have attracted many interests because of their unusual physical properties [1,2]. An anomaly in CeT₂Al₁₀ was observed due to its anisotropic magnetic order. In CeM₂Al₁₀ ($M = \text{Ru, Os, Fe}$) paramagnetic susceptibility (χ) exhibits large anisotropy $\chi_a > \chi_c > \chi_b$ at $T > T_0$, where χ_i is the susceptibility along i -axis T_0 being the transition temperature to the antiferromagnetic (AFM) state. Interestingly, at $T < T_0$ the AFM order occurs along the c axis, not along the easy a -axis. As a possible origin of this anomaly, anisotropy of the $c-f$ hybridization strength has been suggested [3]. We have been studying the electronic structures of CeM₂Al₁₀ with angle-resolved photoelectron spectroscopy (ARPES) for a few years. The results show the anisotropy of the hybridization strength; the hybridization along the magnetic axis is stronger than others. In this study we extend our ARPES to La-doped CeRu₂Al₁₀ sample. 10% La-substitution to the Ce site is known to change the magnetic axis from the c axis to the b axis [4] and thus the (Ce,La)Ru₂Al₁₀ system is another good example to study the correlation between the hybridization and magnetism.

Figure 1 shows the ARPES results of (Ce_{0.9}La_{0.1})Ru₂Al₁₀ at $h\nu = 115$ eV (off resonance) and 122 eV (on resonance) along the a and b axes. Complex electronic structures are observed. The angle-integrated spectra are shown in Fig. 2. It is known that the intensity ratio of $4f^1$ near the Fermi level to $4f^0$ around the binding energy of 2.5 eV is a measure of the $c-f$ hybridization strength. The hybridization strength along ΓB (nearly along the b -axis) is stronger than that along ΓA (nearly along the a -axis) as shown in Fig. 2(c) for the 10% La-doped sample. Figure 2(d) shows that that along ΓC is comparable to that along ΓA . On the other hand, in CeRu₂Al₁₀ the hybridization strength along ΓB is stronger compared to that along ΓA . Thus, our results show the direct observation of the anisotropy of the hybridization strength and, in general, the hybridization strength along the magnetic axis is always stronger than others in Ce1-2-10 systems.

Present results deny the scenario that a larger $c-f$ hybridization along the a -axis could flip the magnetization easy axis towards the c -axis in CeRu₂Al₁₀ [3]. Our finding is that the coexistence of the larger $c-f$ hybridization and the AFM order. This suggests that the itinerant character in

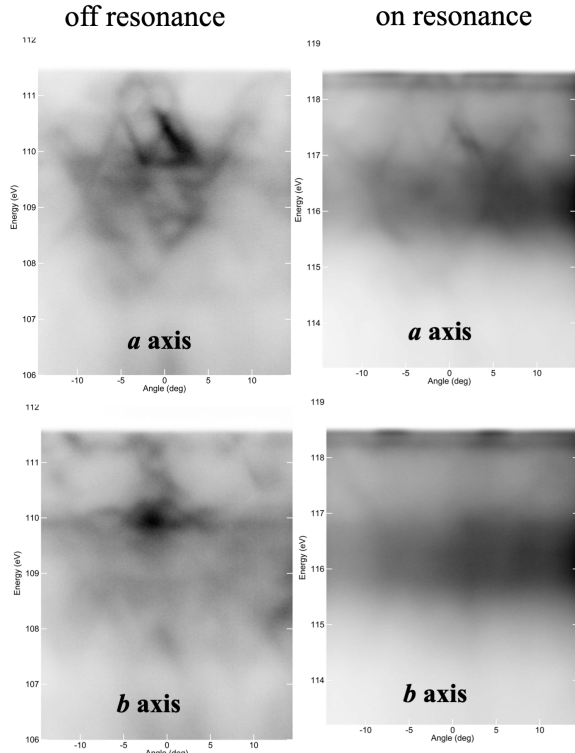


FIGURE 1. ARPES results of (Ce_{0.9}La_{0.1})Ru₂Al₁₀ at $h\nu = 115$ eV (off resonance) and 122 eV (on resonance) along the a and b axes.

magnetism and the $c-f$ hybridization is possibly a driving force of the itinerant magnetism [5,6].

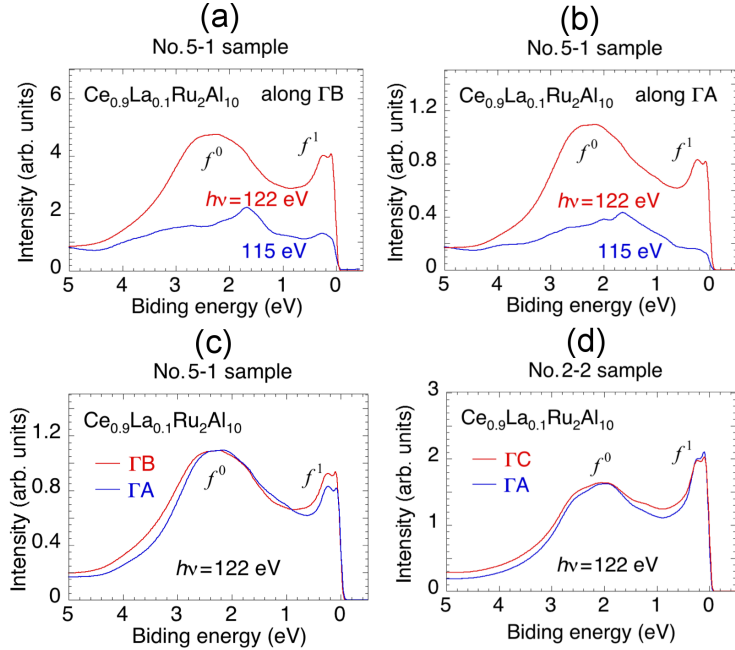


FIGURE 2. Angle-integrated spectra obtained from the angle-resolved spectra of $(Ce_{0.9}La_{0.1})Ru_2Al_{10}$. (a) Spectra along ΓB at 122 and 115 eV. (b) Spectra along ΓA at 122 and 115 eV. (c) Comparison of the spectra between the directions along ΓB and ΓA . (d) Comparison of the spectra between the directions along ΓC and ΓA .

REFERENCES

1. V. M. T. Thiede, T. Ebel, and W. Jeitschko, *J. Mater. Chem.* **8**, 125 (1998).
2. T. Nishioka, Y. Kawamura, T. Takesaka, R. Kobayashi, H. Kato, M. Matsumura, K. Kodama, K. Matsubayashi, and Y. Uwatoko, *J. Phys. Soc. Jpn.* **78**, 123705 (2009).
3. A. Kondo, J. Wang, K. Kindo, Y. Oogane, Y. Kawamura, S. Tanimoto, T. Nishioka, D. Tanaka, H. Tanida, and M. Sera, *Phys. Rev. B* **83**, 180415 (2011).
4. K. Yoshida, R. Okubo, H. Tanida, T. Matsumura, M. Sera, T. Nishioka, M. Matsumura, C. Moriyoshi, and Y. Kuroiwa, *Phys. Rev. B* **91**, 235124 (2015).
5. S. Hoshino and Y. Kuramoto, *Phys. Rev. Lett.* **111**, 026401 (2013).
6. K. Chen, M. Sundermann, F. Strigari, J. Kawabata, T. Takabatake, A. Tanaka, P. Bencok, F. Choueikani, and A. Severing, *Phys. Rev. B* **97**, 155106 (2018).

Electronic Structure of Elementary Excitation in Quantum Spin Liquid

Cai Liu,^{a,*} Yuan Wang,^{a,*} Liang-Long Huang,^a Xiao-Ming Ma,^a Yu-Jie Hao,^b Ke Deng,^a Chang Liu,^{a,b} Zhan-Yang Hao,^b Eike F. Schwier,^c Shiv Kumar,^c Hitoshi Sato,^c Kenya Shimada,^c Le Wang,^{a,#} Jiawei Mei,^{a,b#} and Chaoyu Chen^{a#}

^a Guangdong Provincial Key Laboratory of Quantum Science and Engineering, Shenzhen Institute for Quantum Science and Engineering, Southern University of Science and Technology, Shenzhen 518055, Guangdong, China

^b Department of Physics, Southern University of Science and Technology, Shenzhen 518055, Guangdong, China

^c Hiroshima Synchrotron Radiation Center, Hiroshima University, Higashi-Hiroshima, Hiroshima 739-0046, Japan

Keywords: angle-resolved photoemission spectroscopy; quantum spin liquid; $\alpha\text{-Li}_2\text{IrO}_3$; electron structure

In parallel with the study of nontrivial topology in band insulators [1], there has recently been a growing interest in realizing topologically nontrivial states of matter in strongly or intermediately correlated materials [2]. Despite these aforementioned intensive theoretical efforts, the experimental evidence of correlation-driven topological phases remains rare. So far, the only convincing example is a Kondo insulator SmB_6 [3] in which the correlation and hybridization of $4f$ and $5d$ electrons play on equal footing, resulting in negative gap opening and nontrivial band topology. However, in addition to the complexity of driving forces in topological Kondo insulators, a clear topological surface Dirac cone remain elusive experimentally in correlation-driven topological insulators. $5d$ transition metal oxides are promising materials for it.

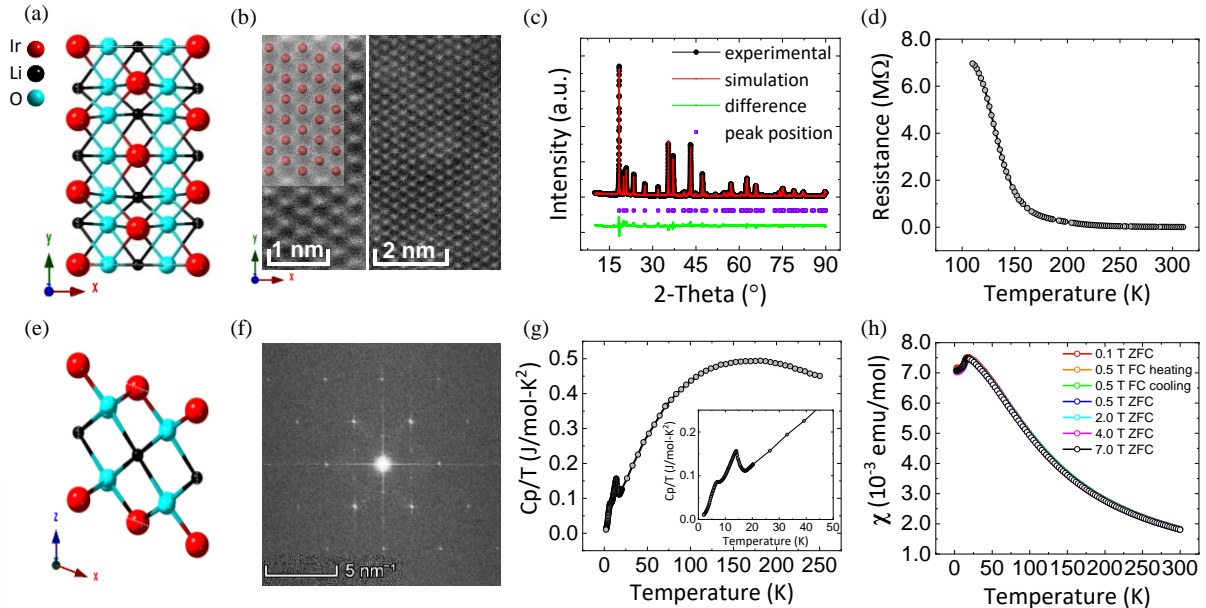


FIGURE 1. Structure and basic physical properties of single-crystalline $\alpha\text{-Li}_2\text{IrO}_3$. (a) xy plane structure. (b) STEM images of xy plane. (c) Refinement of powder X-ray diffraction result. (d) Temperature dependence of resistance. (e) xz plane structure. (f) Electron diffraction pattern in TEM of xy plane in figure 1b. (g) Temperature dependence of C_p/T . Inset: enlarged in temperature range 2–45 K. (h) Temperature dependence of magnetic susceptibility, H/xy -plane.

We chose $\alpha\text{-Li}_2\text{IrO}_3$ as the start, and firstly measured the basic physical properties, observed the xy plane structure by STEM. Due to the light mass of Li and oxygen atoms, only Ir atoms and their lattice could be

observed clearly in Fig. 1b. There are two positions of Ir atoms with different occupation. Ir(1) atoms form the honeycomb and the atoms in the honeycomb center are Ir(2). By investigating the comprehensive band structure of α -Li₂IrO₃, we report its clear band structure for the first time in Fig. 2, to the best of our knowledge. In Fig.3 there exists a possible surface 2D Dirac cone in its valence band gap between Ir 5d and O 2p bands. It needs further theoretical and experimental investigation to clarify the physical origin of the bands. It is hopeful that in exploring the nontrivial topology in correlated materials, 5d iridates would be a novel platform for exploring exotic phenomena from the interplay of correlation, SOC, topology, superconductivity and so on.

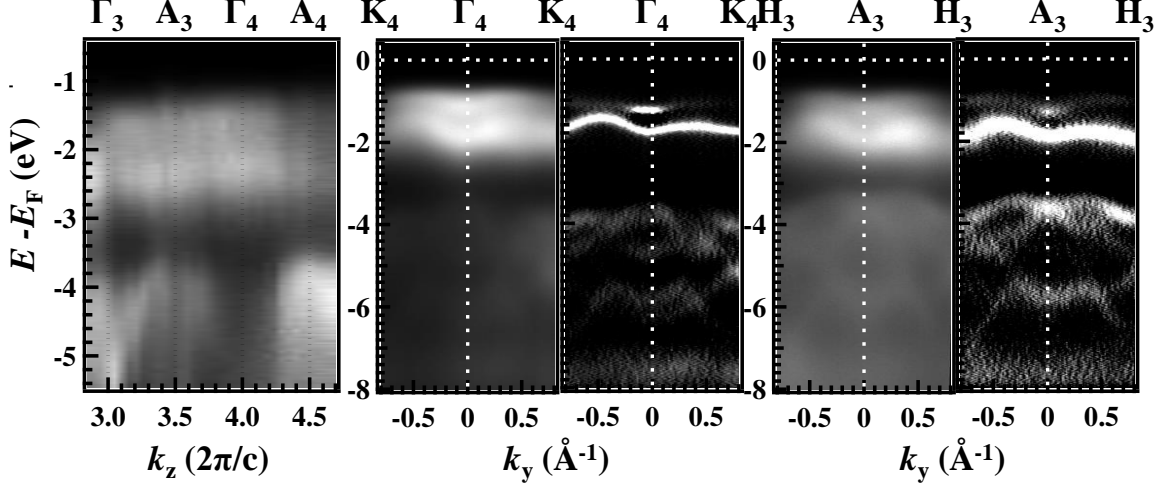


FIGURE 2. General dispersion of α -Li₂IrO₃ at 300 K.

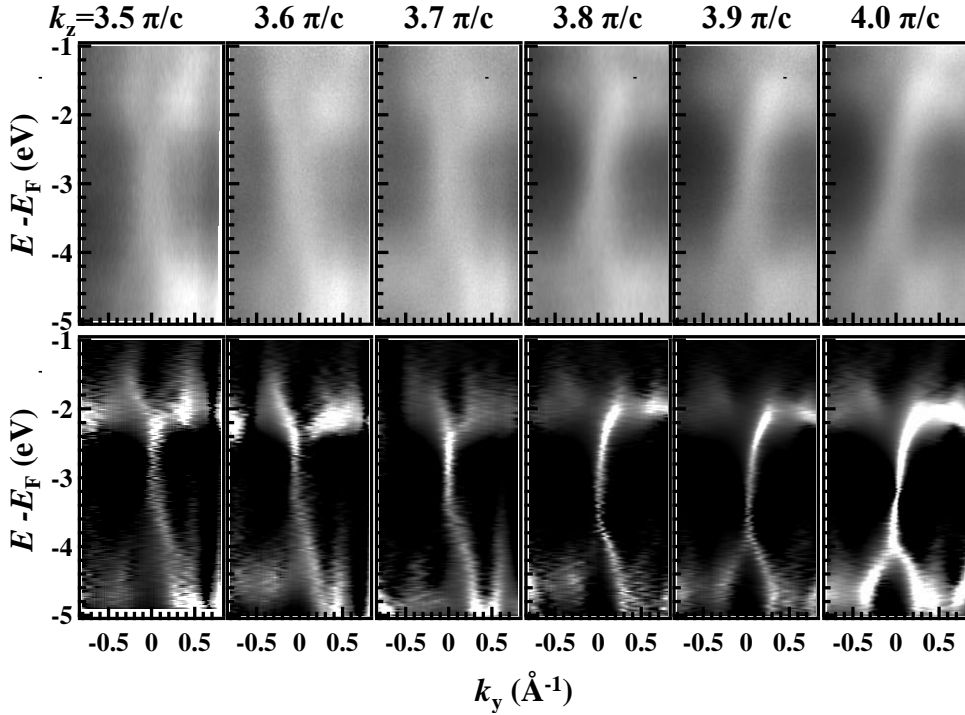


FIGURE 3. Possible 2D Dirac cone of α -Li₂IrO₃ at 300 K.

REFERENCES

1. Ando, Y. & Fu, L. Topological Crystalline Insulators and Topological Superconductors: From Concepts to Materials. Annual Review of Condensed Matter Physics 6, 361-381 (2015).
2. Weng, H. et al. Topological crystalline Kondo insulator in mixed valence ytterbium borides. Phys Rev Lett 112, 016403 (2014).
3. Ohtsubo, Y. et al. Non-trivial surface states of samarium hexaboride at the (111) surface. Nat Commun 10, 2298 (2019).

Experimental evidence of monolayer AlB₂ with symmetry-protected Dirac cones

D. Geng^{a,b}, K. Yu^c, S. Yue^{a,b}, J. Cao^c, W. Li^{a,b}, D. Ma^c, C. Cui^c, M. Arita^d, S. Kumar^d, E. Schwier^d, K. Shimada^d, P. Cheng^{a,b}, L. Chen^{a,b,e}, K. Wu^{a,b,e}, Y. Yao^c, and B. Feng^{a,b}

^aInstitute of Physics, Chinese Academy of Sciences, Beijing 100190, China

^bSchool of Physical Sciences, University of Chinese Academy of Sciences, Beijing 100049, China

^cKey Lab of Advanced Optoelectronic Quantum Architecture and Measurement(MOE), School of Physics, Beijing Institute of Technology, Beijing 100081, China

^dHiroshima Synchrotron Radiation Center, Hiroshima University, 2-313 Kagamiyama, Higashi-Hiroshima 739-0046, Japan

^eSongshan Lake Materials Laboratory, Dongguan, Guangdong 523808, China

Keywords: monolayer AlB₂, Dirac cones, ARPES, molecular beam epitaxy, density functional theory

The discovery of the high-temperature superconductor MgB₂ ($T_c \approx 39$ K) has stimulated significant research interest in the AlB₂ family of materials [1,2]. In MgB₂, the σ -bonding boron orbitals couple strongly with the in-plane B-B stretching phonon modes [3–6], which is crucial for the occurrence of high-temperature superconductivity. However, in AlB₂, an isostructural compound of MgB₂, the boron σ state is located far below the Fermi level and lacks effective coupling with phonons in the boron layer [3,7]. Therefore, no experimental evidence for AlB₂ superconductivity has been reported to date. Recently, the desire to miniaturize quantum devices has driven significant research interest in two-dimensional (2D) materials [8,9]. In the 2D limit, monolayer AlB₂ has been predicted to be a superconductor with an intriguing multigap character [10,11], which is in stark contrast with the non-superconducting properties of bulk AlB₂. In addition, bulk AlB₂ has been found to host Dirac nodal lines [12], which indicates the possible existence of topological band structures in monolayer AlB₂. However, the synthesis of monolayer AlB₂ has remained a challenge to date and little is known about the topological properties of monolayer AlB₂.

Recently, various synthetic 2D materials have been realized via molecular beam epitaxy (MBE), including silicene, stanene, and borophene. In particular, honeycomb borophene, an important constituent of monolayer AlB₂, has been realized on Al(111). Notably, the topmost atomic layer of Al(111) has a flat triangular lattice that can constitute monolayer AlB₂ with honeycomb borophene. However, in the previously proposed structure model, the lattice of borophene was compressed to fit the lattice constant of Al(111), and thus the topmost triangular Al lattice was inseparable from the underlying Al(111) substrate. This results in strong hybridization of the electronic structure of AlB₂ with the substrate.

Here, however, our combined low-energy electron diffraction (LEED) and scanning tunneling microscopy (STM) measurements show that the lattice constant of the surface AlB₂ layer is slightly larger than that of Al(111), which indicates relatively weak coupling between AlB₂ and Al(111). We also studied the electronic structures and topological properties of monolayer AlB₂ via angle-resolved photoemission spectroscopy (ARPES) and first-principles calculations. Several symmetry-protected Dirac cones were observed in a freestanding AlB₂ monolayer, and most of them were preserved on Al(111). Moreover, some of the Dirac bands cross the Fermi level and may contribute to electron-phonon coupling. Therefore, the realization of monolayer AlB₂ provides an ideal platform to study the exotic properties that arise from the coexistence of Dirac fermions and superconductivity.

The growth of boron on Al(111) leads to the formation of an ordered structure with triangular corrugations,

as shown in Fig. 1(a). The period of the triangular corrugation is ~ 7 nm. From the high-resolution STM image in Fig. 1(b), a honeycomblike structure can be observed with a lattice constant of ~ 3.0 Å, which indicates the formation of the honeycomb borophene. These results agree well with previous reports. LEED measurements were performed to study the atomic structure of this system. Figures 1(c) and 1(d) show the LEED patterns of pristine Al(111) and B/Al(111), respectively. It was found that the lattice constant of the surface structure was slightly larger than that of Al(111), as shown in the inset of Fig. 1(d). Based on the LEED pattern, the lattice constant of the surface structure was estimated to be 2.98 Å, which was in qualitative agreement with the STM results. Because of the different lattice constants of the surface structure and the underlying substrate, moiré patterns form because of the lattice mismatch. A simple analysis shows that the 25×25 superstructure of Al(111) ($a_{\text{Al}} = 2.86$ Å) corresponds to the 24×24 superstructure of the surface layer ($a_s = 2.98$ Å). The period of the superstructure is ~ 7.15 nm, which is in agreement with the period of the triangular corrugations (~ 7 nm). Therefore, our results confirmed that the triangular corrugations originate from the moiré patterns of the system.

After establishing the synthesis of the AlB₂ monolayer, we move on to studying its electronic structure. Figure 2(d) shows the calculated band structure of freestanding AlB₂, which agrees with recent calculation results [11]. In proximity to the $\bar{\Gamma}$ point, there are several bands that cross the Fermi level: α , β , and γ . Interestingly, these bands host two Dirac cones along the $\bar{\Gamma}$ -K and $\bar{\Gamma}$ -M directions, respectively, as indicated by the red arrows in Fig. 2(d). The mirror eigenvalues of these bands are indicated by the “+” and “-” signs. The crossing bands of these Dirac cones have opposite eigenvalues, which indicates that these Dirac cones are protected by the mirror reflection symmetry: the $\bar{\Gamma}$ -K-k_z plane and $\bar{\Gamma}$ -M-k_z plane, respectively. Another Dirac cone is centered at the K point, as indicated by the red circle in Fig. 2(d). This Dirac cone derives from the p_z orbitals of boron, analogous to the Dirac cone of the honeycomb lattice. Therefore, the Dirac cone at the K point originates from the honeycomb borophene and survives in the monolayer AlB₂ despite the inclusion of a hexagonal Al layer.

ARPES measurements were performed to verify the intriguing electronic structures of the monolayer AlB₂ and the results are shown in Fig. 3. The α , β , and γ bands near the $\bar{\Gamma}$ point of freestanding AlB₂ can be clearly observed in the ARPES results. In particular, the Dirac cones survive without any obvious gap opening, as indicated by the black arrows. The persistence of these bands on Al(111) indicates a weak interaction between AlB₂ and Al(111). There was no discernible k_z dispersion on changing the incident photon energy, which agrees with the 2D character of these bands. Furthermore, an additional γ band was observed, which was located 1 eV above the γ band. It should be noted that two electronlike bands were observed at the $\bar{\Gamma}$ and K points of Al(111), as indicated by the red arrows. These bands originate from the surface states of Al(111) because the coverage of AlB₂ was less than one monolayer. The observation of the Al(111) surface state indicates the high order and cleanliness of the sample surface.

This work has been published in Physical Review B **101**, 161407 (2020).

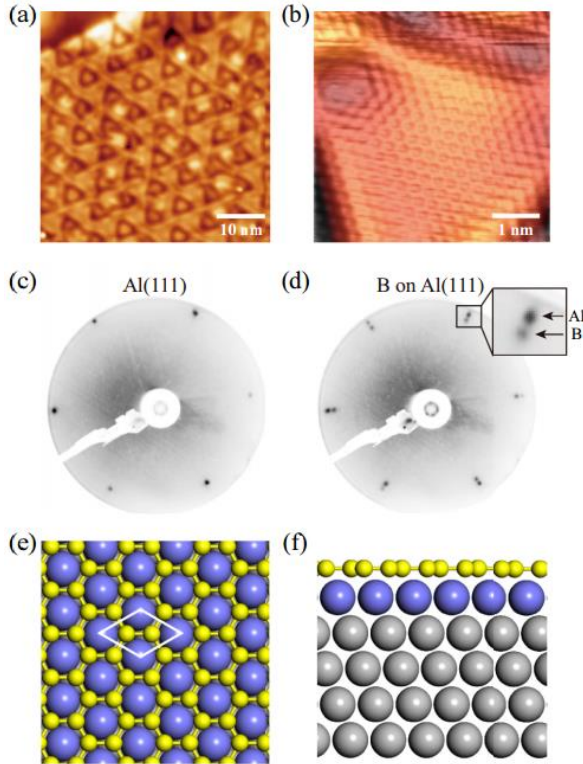


FIGURE 1. (a) An STM image of boron on Al(111) showing the triangular corrugations. (b) Magnified STM image showing the honeycomb lattice of boron. (c) and (d) LEED patterns of Al(111) and B/Al(111), respectively. (e) and (f) Top and side views of the structure model of B/Al(111). The white rhombus indicates a unit cell of honeycomb borophene or monolayer AlB₂. The boron and topmost Al atoms are indicated by yellow and blue balls, respectively. The underlying Al atoms are indicated by gray balls.

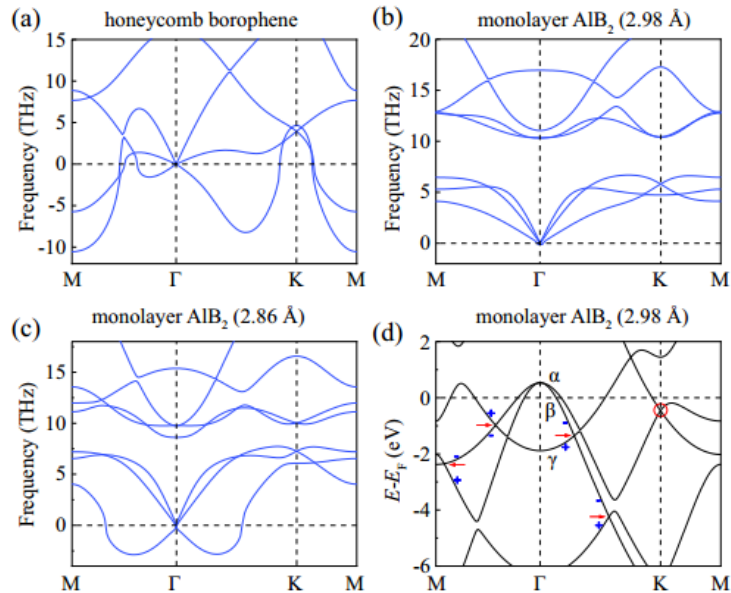


FIGURE 2: (a) Calculated phonon spectrum of the honeycomb borophene. (b), (c) Calculated phonon spectrum of the monolayer AlB₂ with lattice constants of 2.98 and 2.86 Å, respectively. The optimized lattice constant of the freestanding AlB₂ monolayer is 2.98 Å. (d) Calculated band structure of the monolayer AlB₂. The three characteristic bands are indicated by α , β , and γ . Red arrows indicate the Dirac cones protected by mirror symmetry along the high-symmetry lines. The “+” and “-” signs (in blue) along $\bar{\Gamma}$ -M and $\bar{\Gamma}$ -K are the mirror eigenvalues of M_M and M_K, respectively. The red circle indicates the Dirac cone derived from the p_z orbitals of boron.

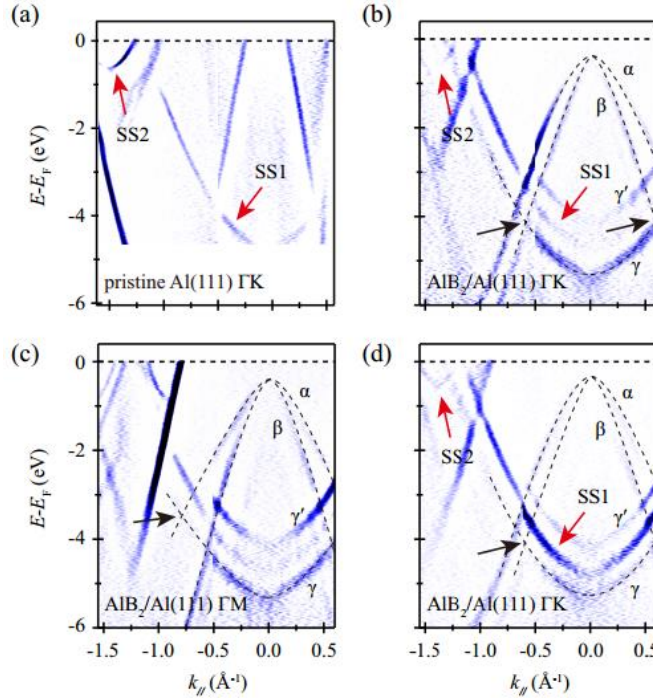


FIGURE 3: (a) ARPES second derivative image of pristine Al(111) measured with 25-eV photons. (b) and (c) ARPES second derivative images of AlB₂/Al(111) along the $\bar{\Gamma}$ -K and $\bar{\Gamma}$ -M directions, respectively. α , β , and γ indicate the three characteristic bands of freestanding AlB₂. The Dirac points are indicated by black arrows. The incident photon energy is 35 eV. (d) ARPES second derivative image of AlB₂/Al(111) along the -K direction measured with 40-eV photons. Red arrows indicate the surface states of Al(111); black arrows indicate the Dirac points of the monolayer AlB₂. The black dashed lines are guides for the eye.

REFERENCES

1. W. N. Kang, H.-J. Kim, E.-M. Choi, C. U. Jung, and S.-I. Lee, Science 292, 1521 (2001).
2. J. Nagamatsu, N. Nakagawa, T. Muranaka, Y. Zenitani, and J. Akimitsu, Nature (London) 410, 63 (2001).
3. K.-P. Bohnen, R. Heid, and B. Renker, Phys. Rev. Lett. 86, 5771 (2001).
4. T. Yildirim, O. Gülsen, J. W. Lynn, C. M. Brown, T. J. Udovic, Q. Huang, N. Rogado, K. A. Regan, M. A. Hayward, J. S. Slusky, T. He, M. K. Haas, P. Khalifah, K. Inumaru, and R. J. Cava, Phys. Rev. Lett. 87, 037001 (2001).
5. Y. Kong, O. V. Dolgov, O. Jepsen, and O. K. Andersen, Phys. Rev. B 64, 020501(R) (2001).
6. H. J. Choi, D. Roundy, H. Sun, M. L. Cohen, and S. G. Louie, Nature (London) 418, 758 (2002).
7. N. I. Medvedeva, A. L. Ivanovskii, J. E. Medvedeva, and A. J. Freeman, Phys. Rev. B 64, 020502(R) (2001).
8. A. H. Castro Neto, F. Guinea, N. M. R. Peres, K. S. Novoselov, and A. K. Geim, Rev. Mod. Phys. 81, 109 (2009).
9. M. Xu, T. Liang, M. Shi, and H. Chen, Chem. Rev. 113, 3766 (2013).
10. M. Gao, X.-W. Yan, J. Wang, Z.-Y. Lu, and T. Xiang, Phys. Rev. B 100, 024503 (2019).
11. Y. Zhao, C. Lian, S. Zeng, Z. Dai, S. Meng, and J. Ni, Phys. Rev. B 100, 094516 (2019).
12. D. Takane, S. Souma, K. Nakayama, T. Nakamura, H. Oinuma, K. Hori, K. Horiba, H. Kumigashira, N. Kimura, T. Takahashi, and T. Sato, Phys. Rev. B 98, 041105(R) (2018).

ARPES Study of a new type-II Dirac semimetal candidate NiTe_2

Shaozhu Xiao^a, Ya Feng^a, Eike F. Schwier^b, Kenya Shimada^b and Shaolong He^a,

^a*Ningbo Institute of Materials Technology and Engineering, Chinese Academy of Sciences, Ningbo, Zhejiang 315201, China*

^b*Hiroshima Synchrotron Radiation Center, Hiroshima University, Higashi-Hiroshima 739-0046, Japan*

Keywords: ARPES, NiTe_2 , Dirac node.

Since the discovery of topological insulators, quantum materials with special topological band structures, e.g., topological semimetals, have attracted a tremendous research interest due to the rich physics therein. Topological semimetals can be classified into Dirac semimetals, Weyl semimetals, nodal-line semimetals and etc. [1, 2]. The Dirac semimetal is particularly important since it stands at the critical point of topological phase transition and can be tuned to Weyl semimetal or topological insulator via crystal distortions or magnetic doping. In some Dirac semimetals, as a result of the broken Lorentz symmetry, the Dirac cone is strongly tilted and these materials are called type-II Dirac semimetal. Compared to type-I Dirac semimetal, the special band topology in type-II Dirac semimetal is expected to result in many interesting phenomena, such as direction-dependent chiral anomaly [3], anisotropic electrical transport [4] and so on.

Recently, some transition metal dichalcogenides, include PdTe_2 , PtTe_2 , and PtSe_2 , has been theoretically predicted and experimentally confirmed to be type-II Dirac semimetals [5-7]. However, the experimentally confirmed type-II Dirac semimetals are still very rare and the Dirac nodes observed in these materials are quite far away from the Fermi level, making Dirac fermions less contribute to the transport properties.

More recently, the nickel ditelluride (NiTe_2) with a CdI₂-type trigonal structure, has been theoretically pointed out to be a new candidate for type-II Dirac semimetals [8-10]. Compared to other reported type-II Dirac semimetals, the Dirac nodes in NiTe_2 are much close to the Fermi level, which will make Dirac fermions in NiTe_2 more prominently contribute to the transport properties and the NiTe_2 may represent an improved platform to study the type-II Dirac physics.

The predicted 3D type-II Dirac node of NiTe_2 locates on the Γ -A direction [8], which is perpendicular to the easy cleavage surface of NiTe_2 . In order to determine the inner potential and search out the predicted Dirac node, we have performed photon energy dependent ARPES measurements at HiSOR BL-1. As shown in Fig. 1, in addition to the bulk bands, many surface states appear. By extracted the EDCs at Γ point taken with different photon energies, rough band dispersions along Γ -A (k_z) direction was obtained, as shown in Fig. 2(a). It can be determined that $h\nu = 42$ eV corresponds to Γ point and $h\nu = 60$ eV corresponds to A point. Thus, the inner potential can be determined to be 10.1 eV. By comparing the experimental and calculated results (see yellow box in Fig. 2(a) and Fig. 2(b)), the band marked with red line seems to be one of the two bands which intersect to form the type-II Dirac point. However, there is not any evidence of another band, which may be due to the poor resolution along k_z direction or the band stay above the Fermi level.

Using μ -Laser ARPES, which could focus light to the micron size and avoid the influence of domains, spin-polarized surface state of NiTe_2 was also observed, as shown in Fig. 3.

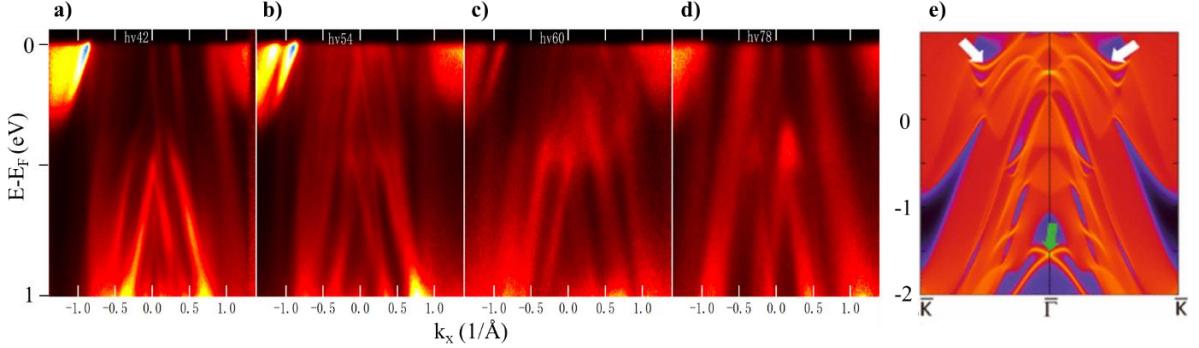


FIGURE 1. Band structures along Γ -K taken with different energies: (a) 42 eV, (b) 54 eV, (c) 60 eV, (d) 78 eV; (e) Calculated surface band structure[8].

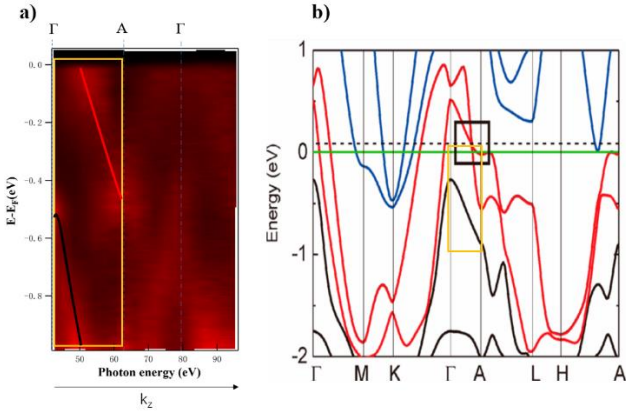


FIGURE 2. (a) Band dispersion along Γ -A- Γ (k_z) direction. (b) Calculated band structure [8]. The yellow box corresponds to that in image (a).

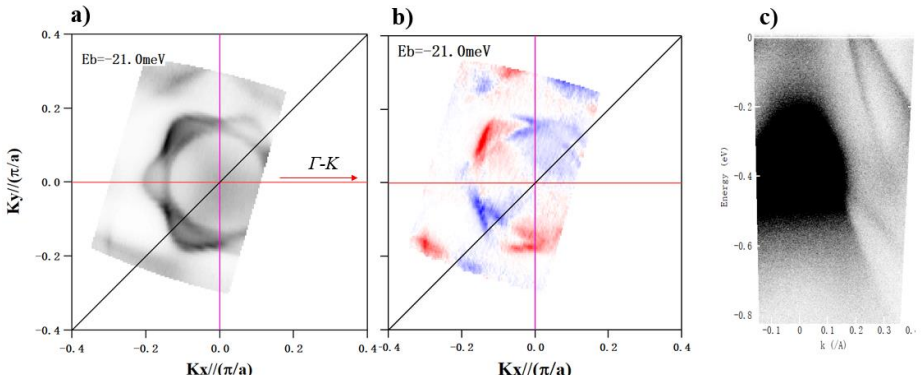


FIGURE 3. (a) Constant energy surface at $E_b = 21$ meV obtained using Laser ARPES ($h\nu = 6.3$ eV). (b) Circular dichroism of constant energy surface at $E_b = 21$ meV. (c) Band structure around Γ point along Γ -K direction.

REFERENCES

1. Burkov, A. A., Nat. Mater. 15, 1145–1148 (2016)
2. N. P. Armitage, E. J. Mele, and A. Vishwanath, Rev. Mod. Phys. 90, 015001 (2018)
3. Lv, Y. Y. et al., Phys. Rev. Lett. 118, 096603 (2017)
4. M. N. Ali, et al., Nature 514, 205 (2014)
5. Liu, Y., et al., Chin. Phys. Lett. 32, 067303 (2015)
6. Yan, M., et al., Nat. Commun. 8, 257 (2017)
7. Zhang K., et al., Phys. Rev. B 96, 125102 (2017).
8. C. Xu, et al., Chemistry of Materials 30, 4823 (2018).
9. B. S. de Lima, et al., Solid State Commun. 283, 27 (2018).
10. Q. Liu, et al., arXiv:1901.01749 (2019).

ARPES Study on Zintl Phase $\text{Ba}_3\text{Cd}_2\text{As}_4$ - A Proposed Topological Crystalline Insulator Protected by C_2 Rotational Symmetry

Xiao-Ming Ma^a, Yu-Jie Hao^a, Yue Feng^a, Ni Ni^b and Chang Liu^a

^a Shenzhen Institute for Quantum Science and Engineering (SIQSE) and Department of Physics, Southern University of Science and Technology (SUSTech), Shenzhen 518055, China.

^b Department of Physics and Astronomy and California NanoSystems Institute, University of California, Los Angeles, California 90095, USA

Keywords: Topological Crystalline Insulators, $\text{Ba}_4\text{Cd}_2\text{As}_3$, Angle Resolved Photoelectron Spectroscopy.

Topological insulators (TIs) which possess an insulating bulk yet metallic surface states protected by a nontrivial band topology have attracted much attentions since their discovery [1,2]. However, TIs are very limited in real materials because the realization of TI phases requires strong spin-orbit coupling (SOC) and time-reversal symmetry (TRS) [3,4]. To extend the topological family much effort has been devoted to exploit new TIs. Theoretical studies have proposed the idea of a new class of topological insulators, topological crystalline insulators (TCIs), in which specific crystalline symmetries warrant the topological protection of metallic surface states [5]. Our first principal calculations suggest that the charge-balanced Zintl phase $\text{Ba}_4\text{Cd}_2\text{As}_3$ is another TCI candidate. The $\text{Ba}_4\text{Cd}_2\text{As}_3$ compound crystallize in monoclinic $C2/m$ space group (No. 12) with cell parameters of $a = 17.089 \text{ \AA}$, $b = 4.6076 \text{ \AA}$ and $c = 7.3039 \text{ \AA}$ and the crystal structure schematic and is shown in FIG. 1 (a) [6]. The first principal calculated band structure and the temperature dependent resistivity are also given in Fig. 1 (d) and (e), respectively. Therefore, we employed the high-resolution angle-resolved photoemission spectroscopy (ARPES) setup at BL-01 of HiSOR to investigate the electronic structure of $\text{Ba}_4\text{Cd}_2\text{As}_3$. We did a Fermi mapping of $\text{Ba}_4\text{Cd}_2\text{As}_3$ with 130 eV photon to search the characteristic band structure and Dirac cone surface state predicated by the band calculation.

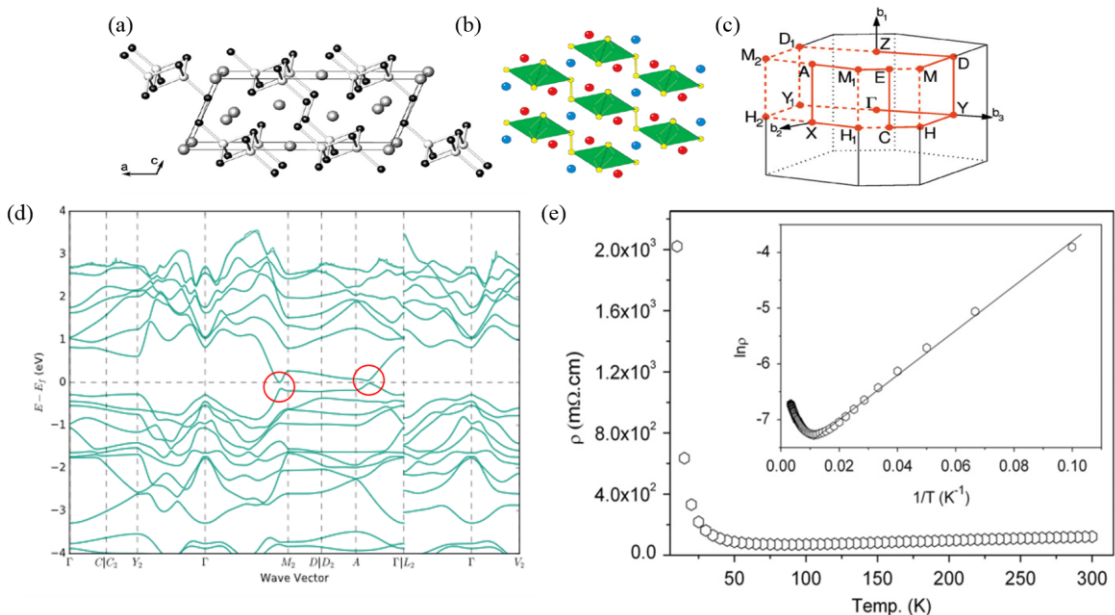


FIGURE 1. FIG.1 (a) Crystal structure of $\text{Ba}_4\text{Cd}_2\text{As}_3$, viewed down the b -axis [6]. (b) Schematic of $\text{Ba}_4\text{Cd}_2\text{As}_3$ structure [7]. (c) Brillouin zone (BZ) of $\text{Ba}_4\text{Cd}_2\text{As}_3$ [8]. (d) First principles bulk band calculation for $\text{Ba}_4\text{Cd}_2\text{As}_3$. It is clear from the calculation that the band touching happens along the Γ -A and Γ -M₂ direction close to the zone center [9]. (e) The temperature-

dependent resistivity measurements on the $\text{Ba}_4\text{Cd}_2\text{As}_3$ single crystal [6].

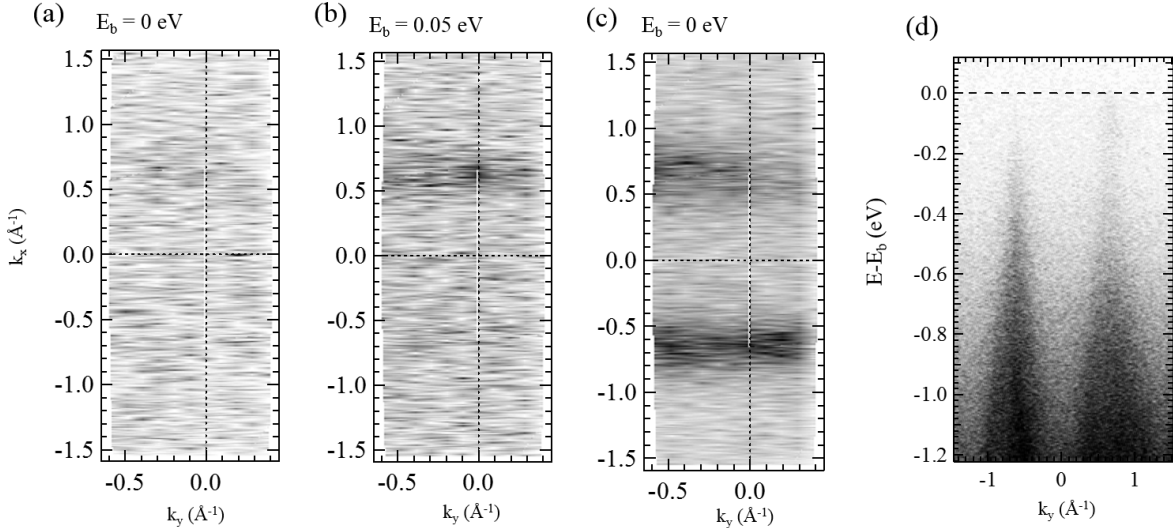


FIGURE 2. ARPES results of V_3S_4 . (a) - (c) are the constant energy contours results with indicated E_b . (d) is the k - E cuts accross the $(0, 0)$ position along the y direction.

As shown in Fig. 2 (a) to (c), the mapping patterns appear rectangle symmetry, which consists with the symmetry of the (100) surface of the $\text{Ba}_4\text{Cd}_2\text{As}_3$. We intercepted one k - E cuts along the y direction pass the Γ position at $(0, 0)$. As shown in Fig. 2 (d), two linear energy bands can be observed on both sides of the Γ point, which are likely to be the predicated Dirac cone.

In all, we have observed Dirac cone shape bands in $\text{Ba}_4\text{Cd}_2\text{As}_3$ but further more detailed and systematically ARPES measurements are still demanded.

REFERENCES

- 1 B. A. Bernevig, T. L. Hughes, and S.-C. Zhang, *Science* 2006, 314, 1757.
- 2 M. König, S. Wiedmann, C. Brüne, et al. *Science* 2007, 318, 766.
- 3 S. Murakami, *Phys. Rev. Lett.* 2006, 97, 236805.
- 4 L. Fu, C. L. Kane, and E. J. Mele, *Phys. Rev. Lett.* 2007, 98, 106803.
- 5 L. Fu, *Phys. Rev. Lett.* 2011, 106, 106802.
- 6 J. Wang, S.Q. Xia, and X.T. Tao, *Cheminform*, 2013, 44(16):6-9.
- 7 B. Saparov, S.Q. Xia, and S. Bobev, *Inorganic Chemistry*, 2008, 47(23):11237.
- 8 W. Setyawan, and S. Curtarolo, *Computational Materials Science*, 2010, 49(2):0-312.
- 9 Institute of Physics Chinese Academy of Sciences, Computer Network Information Center Chinese Academy of Sciences, 2018, <http://materiae.iphy.ac.cn/materials/MAT00003018>

ARPES Measurements on Thin Films of Topological Crystalline Insulator $Pb_xSn_{1-x}Te$

Takuto Watanabe^a, Takeru Shimano^a, Yuta Tomohiro^a, Kota Hiwatari^b, Ryota Akiyama^b, Shiv Kumar^c, Akio Kimura^d, Kenya Shimada^c, Shuji Hasegawa^b, and Shinji Kuroda^a

^a*Institute of Materials Science, University of Tsukuba, 1-1-1 Tennoudai, Tsukuba 305-8573, Japan*

^b*Department of Physics, The University of Tokyo, 7-3-1 Hongo, Bunkyo, Tokyo 113-8654, Japan*

^c*Hiroshima Synchrotron Radiation Center, Hiroshima University, 1-3-2 Kagamiyama, Higashi-Hiroshima 739-8511, Japan*

^d*Department of Physics, Hiroshima University, 1-3-2 Kagamiyama, Higashi-Hiroshima 739-8511, Japan*

Keywords: Topological crystalline insulators, Dirac cone, Gap opening, Mirror reflection symmetry

Topological crystalline insulator (TCI) has been attracting attention as a new class of topological materials, in which the topological surface state (TSS) is protected by the mirror reflection symmetry[1], instead of the time-reversal symmetry (TRS) in the conventional Z_2 topological insulator (TI). SnTe has been known as a typical material of TCI[2] while PbTe belongs to a trivial insulator even with the same crystal structure as SnTe. Accordingly, a mixed crystal $Pb_xSn_{1-x}Te$ exhibits the transition from topological to trivial phase at a Pb content $x \sim 0.7$ [3-5]. In order to investigate how the TSS in $Pb_xSn_{1-x}Te$ changes with the Pb content x , we have been doing the angle-resolved photoemission spectroscopy (ARPES) measurement on $Pb_xSn_{1-x}Te$ thin films. In our previous measurement, we performed the ARPES measurement on a series of $Pb_xSn_{1-x}Te$ films with relatively low Pb content $x = 0 \sim 0.23$ [6]. In the present study, we have done the same measurement on a series of films with higher Pb content of $x = 0.5 \sim 0.8$.

We prepared a series of $Pb_xSn_{1-x}Te$ (111) thin films with nominal Pb contents of $x = 0.5, 0.6, 0.7, 0.8$ grown by molecular beam epitaxy (MBE) on a conductive CdTe template[7]. In some of the films, Sb was doped as a donor impurity with a concentration about 1% in order to compensate the Sn vacancies formed in the crystal. We performed the ARPES measurement at BL-1 of HiSOR. We used a home-made portable vacuum chamber in order to bring the grown films without exposure to air. After having transferred the grown films into the preparation chamber of BL-1, we annealed them at around 200°C to clean the surface. Then we observed the unreconstructed diffraction pattern by low-energy electron diffraction (LEED).

Figure 1 shows the result of ARPES measurements on the $Pb_xSn_{1-x}Te$ (111) film with $x = 0.5$ co-doped with 1% Sb; the $E-k_x$ plots of ARPES intensity and the Fermi-surface mapping around the $\bar{\Gamma}$ and \bar{M} points, where k_x was taken along the $\bar{\Gamma}-\bar{M}$ direction. The measurement was done at $T = 30$ K with an incident photon energy of 30 eV. As shown in the figure, there exist the band dispersions reaching the Fermi level ($E - E_F = 0$) both at the \bar{M} and $\bar{\Gamma}$ points. These band dispersions are assigned as the surface states. Figure 2 compares the $E-k_x$ plots around the $\bar{\Gamma}$ and \bar{M} points for the series of $Pb_xSn_{1-x}Te$ (111) films with $x = 0.5 \sim 0.8$ (1% Sb). At $x = 0.6$, there still exist the band dispersions reaching the Fermi level both at the \bar{M} and $\bar{\Gamma}$ points, but for higher Pb contents $x = 0.7$ and 0.8 , they do not reach the Fermi level, with apparently no states at the Fermi level. This corresponds to the transition from topological to trivial phase at around $x = 0.7$.

In our previous measurement on low Pb-content films ($x = 0.17, 0.23$), we observed the gap-opening at the $\bar{\Gamma}$ point while the gap remains closed at the \bar{M} point[6]. In the present study, however, gap-opening at the $\bar{\Gamma}$ point was not observed at high Pb-content films ($x = 0.5, 0.6$) on the topological side. In a similar ARPES study on another TCI material $Pb_xSn_{1-x}Se$ doped with Bi[8], it was reported that the gap opens at the $\bar{\Gamma}$ point in the surface state while the gap remains closed at the \bar{M} point. In that study[8], the gap-opening at the $\bar{\Gamma}$ point was attributed to the phase transition from the TCI phase to the Z_2 topological phase due to a lattice distortion upon Bi-doping which induces the breaking of the mirror reflection symmetry. In our study on $Pb_xSn_{1-x}Te$, we observed the gap-opening only the $\bar{\Gamma}$ point in the region of low Pb content ($x = 0.17, 0.23$). Further studies including details analysis of the lattice distortion would be needed in order to

understand the origin of the observed gap-opening.

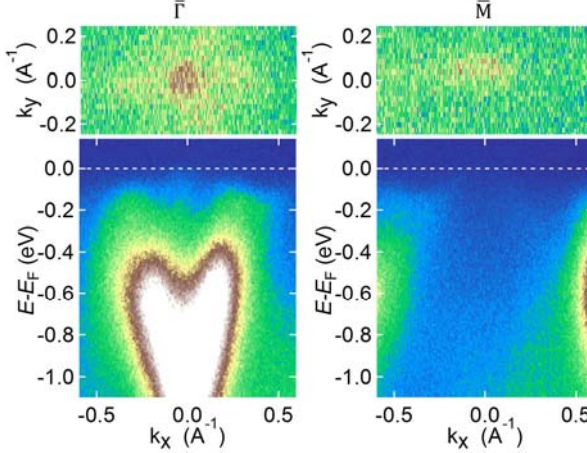


FIGURE 1. The result of ARPES measurements on a $\text{Pb}_x\text{Sn}_{1-x}\text{Te}$ (111) film ($x = 0.5$) with 1% Sb. The $E-k_x$ plots of ARPES intensity (below) and the Fermi-surface mapping (top) around the $\bar{\Gamma}$ and \bar{M} points, respectively. Here k_x was taken along the $\bar{\Gamma}-\bar{M}$ direction. The measurement was done at $T = 30$ K with an incident photon energy of 30 eV.

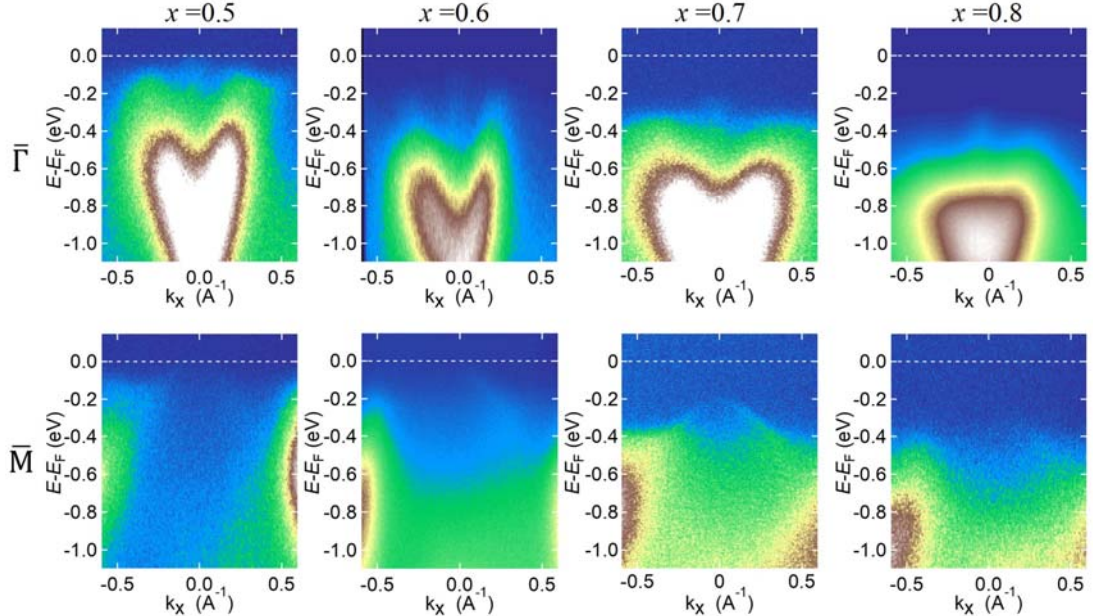


FIGURE 2. The $E-k_x$ plots around the $\bar{\Gamma}$ and \bar{M} points for the $\text{Pb}_x\text{Sn}_{1-x}\text{Te}$ (111) films (doped with 1% Sb) with $x = 0 \sim 0.8$. The measurements were done with the same condition as in Fig. 1.

REFERENCES

1. T. H. Hsieh, H. Lin, J. Liu, W. Duan, A. Bansil, and L. Fu, Nat. Commun. **3**, 982 (2012).
2. Y. Tanaka, Z. Ren, T. Sato, K. Nakayama, S. Souma, T. Takahashi, K. Segawa, and Y. Ando, Nat. Phys. **8**, 800 (2012).
3. S.-Y. Xu *et al.*, Nat. Commun. **3**, 1192 (2012).
4. Y. Tanaka, T. Sato, K. Nakayama, S. Souma, T. Takahashi, Z. Ren, M. Novak, K. Segawa, and Y. Ando, Phys. Rev. B **87**, 155105 (2013).
5. C. Yan *et al.*, Phys. Rev. Lett. **112**, 186801 (2014).
6. Y. Tomohiro *et al.*, HiSOR Activity Report 2018.
7. R. Ishikawa, T. Yamaguchi, Y. Ohtaki, R. Akiyama, S. Kuroda, J. Cryst. Growth **453**, 124 (2016).
8. P. S. Mandal *et al.*, Nat. Commun. **8**, 68 (2017).

ARPES Study of type-II nodal loop in trigonal layered PtBi₂

Shaozhu Xiao^a, Ya Feng^a, Xianxin Wu^b, Eike F. Schwier^c, Masashi Arita^c, Kenya Shimada^c and Shaolong He^a

^aNingbo Institute of Materials Technology and Engineering, Chinese Academy of Sciences, Ningbo, Zhejiang 315201, China

^bInstitute for Theoretical Physics and Astrophysics, Julius-Maximilians University of Wurzburg, Am Hubland, D-97074 Wurzburg, Germany

^cHiroshima Synchrotron Radiation Center, Hiroshima University, Higashi-Hiroshima 739-0046, Japan

Keywords: ARPES, PtBi₂, nodal loop.

PtBi₂ has rich phases, and the best-known ones are β -PtBi₂ and γ -PtBi₂, which crystallize in pyrite type cubic space group Pa $\bar{3}$ and in the trigonal space group P31m [1, 2], respectively. Both β -PtBi₂ and γ -PtBi₂ exhibit unconventional large linear magneto-resistance [3-5], especially the β -PtBi₂, with MR value up to 10⁷ [3]. Motived by the fascinating transport properties, PtBi₂ has attracted interests in both theory and experiment field. β -PtBi₂ has been predicted to be a 3D Dirac semimetal [3,6] but lacking direct experimental evidence. For trigonal layered γ -PtBi₂, previous ARPES studies have revealed the existence of complicated but nontrivial band structures: surface Dirac states at M point [7] and Γ point [8], giant three-dimensional Rashba spin splitting at the M point of Brillouin zone [9].

Recently, our calculation pointed out that there is a nontrivial type-II nodal loop in the trigonal layered γ -PtBi₂. As shown in Fig. 1(a) and Fig. 1(b), there are two nontrivial nodal points along $\bar{\Gamma}$ - \bar{K} direction. The distance between these two points is largest at $k_z = 0.5$ ($2\pi/c$) and shrinks when varying k_z . The two nodal points merge into one point and then disappear around $k_z = 0.35$ and $k_z = 0.7$ ($2\pi/c$). Thus, these nontrivial nodal points form a nontrivial type-II nodal loop in Γ -A-H-K plane, as shown in Fig. 1(c) and Fig. 1(d). The nodal loop might be related to the fascinating transport properties of PtBi₂ and is yet to be studied by ARPES for direct evidence.

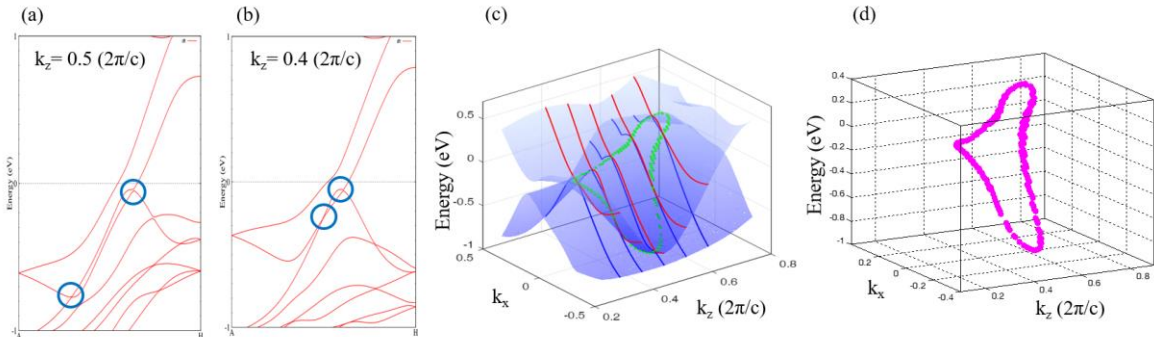


FIGURE 1. (a) and (b) Calculated band structures along $\bar{\Gamma}$ - \bar{K} direction at different k_z as labelled. The blue circles indicate the nontrivial nodal points. (c) and (d) The nontrivial nodal points form a type-II nodal loop in Γ -A-H-K plane.

To find out the evidence of the nodal loop, the band structures along the high symmetry $\bar{\Gamma}$ - \bar{K} direction have been measured with various photon energies, and partial results are shown in Fig. 2. It seems that most of the spectral weights are from the surface states and show no clear k_z dependence. That is, what were observed in our measurements are almost all surface states. The bulk bands with very weak spectral weight are buried and covered by the strong surface states.

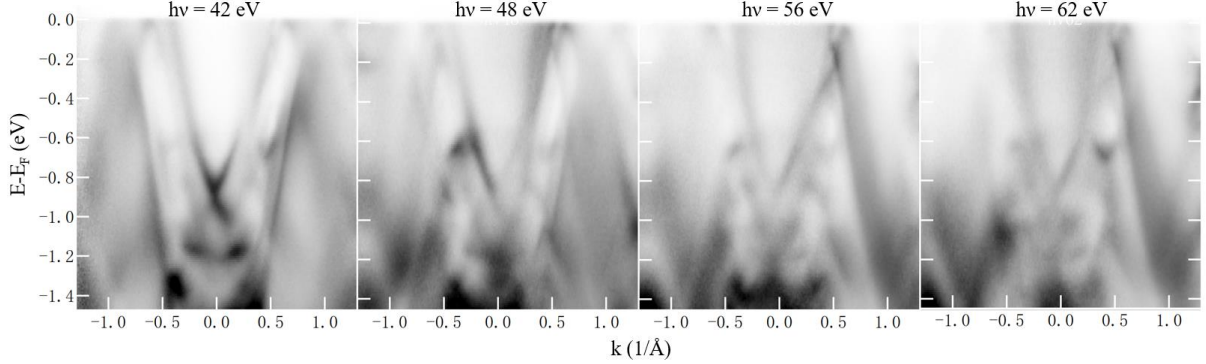


FIGURE 2. Band structures along $\bar{\Gamma}$ - \bar{K} direction obtained using different photon energies as labelled.

In order to see the bulk bands and test the validity of the calculated results, high symmetry cut along $\bar{\Gamma}$ - \bar{K} direction was also measured using the Laser ARPES ($h\nu = 6.3$ eV) that is more bulk sensitive than BL-1 and BL-9, and the results are shown in Fig. 3. The calculated surface states in Fig. 3(b) show good match with the experimental result shown in Fig. 3(a). In addition to the surface states, the photon energy of Laser ARPES has the ability to see the bulk bands, which are clearly shown in the blue box in Fig. 3(c), showing good agreement with the calculated bulk bands in Fig. 3(d). However, in contrast with the surface states, the bulk bands are still very weak. And it is still hard to identify the nodal points predicted by the calculation.

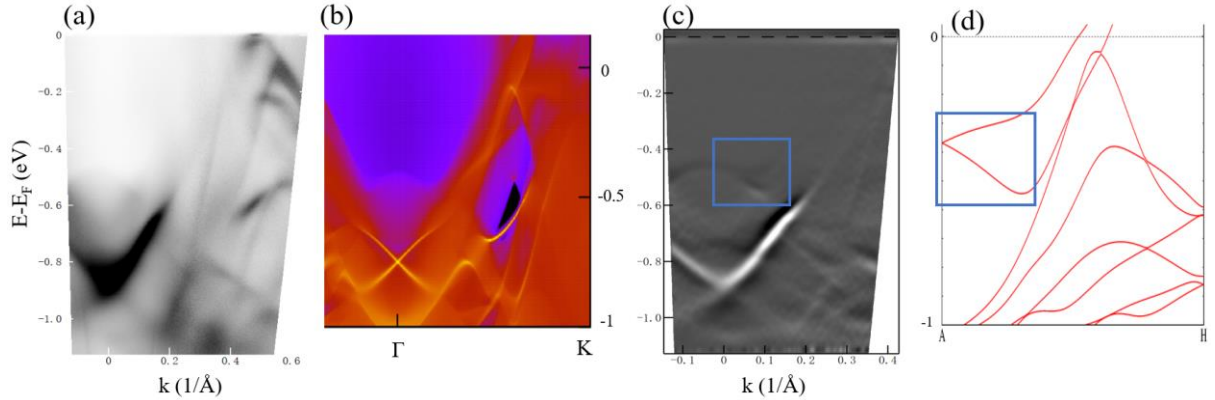


FIGURE 3. (a) Band structures along $\bar{\Gamma}$ - \bar{K} direction obtained using Laser ARPES ($h\nu = 6.3$ eV). (b) Calculated surface states. (c) Second derivative with respect to energy of partial image (a). (d) Calculated bulk band structure along $\bar{\Gamma}$ - \bar{K} direction.

REFERENCES

1. Biswas, T. et al., J. Less-Common Met. 19, 223 (1969).
2. Martin, K. et al., Z. Anorg. Allg. Chem. 640, 2742-2746 (2014).
3. Gao W. et al., Physical Review Letters 118, 256601 (2017).
4. C. Q. Xu, et al., Physical Review B 94, 165119 (2016).
5. Gao W. et al., Nat. Commun. 9, 3249 (2018).
6. Q. D. Gibson, et al., Physical Review B 91, 205128 (2015).
7. Yao Q. et al., Phys. Rev. B 94, 235140 (2016).
8. Thirupathaiah S. et al., Phys. Rev. B 97, 035133 (2018).
9. Feng Y. et al., Nat Commun 10, 4765 (2019).

Evidence of a Bulk Band Structure for SrIrO₃ Thin Films

Takashi Komesu^a, Shiv Kumar^b, Prescott E. Evans^a, Andrew J. Yost^a
 Eike F. Schwier^b, Kenya Shimada^b,
 Le Zhang^a, Xia Hong^a and P. A. Dowben^a

^a*Department of Physics and Astronomy, Nebraska Center for Materials and Nanoscience,
 Theodore Jorgensen Hall, 855 N 16th, University of Nebraska, 880299, Lincoln, NE 68588-0299, U.S.A.*
^b*Hiroshima Synchrotron Radiation Center, Hiroshima University, Higashi-Hiroshima 739-0046, Japan*

Keywords: High Resolution Angle Resolved Photoemission Spectroscopy, Electronic Structure, spin-orbit interaction.

We have previously established that there exists an evolving lattice distortion in high quality epitaxial orthorhombic SrIrO₃(001) thin films fully strained on SrTiO₃(001) [1]. Furthermore 5 nm thick SrIrO₃(001) thin films grown on SrTiO₃(001) are metallic, with itinerant bands crossing the Fermi level as seen in Figure 1. In the IrO₆, oxygen octahedra tilt significantly across the 12 monolayers film, then no bulk band structure should be possible as then there is no conserved wave vector.

As indicated in Figure 1, the surface Brillouin zone, evident from the experimental band structure, is consistent with the (001) surface, as determined by low energy electron diffraction (LEED), but not perturbed by IrO₆ oxygen octahedra that tilt reconstruction. This reconstruction is evident in the $(\sqrt{2}/4) \times (\sqrt{2}/4)$ R45° reciprocal space structure, as indicated by the extra diffraction spots in the LEED [1]. In spite of the $a(\sqrt{2}/4) \times (\sqrt{2}/4)$ R45° reciprocal space structure, as indicated by the extra diffraction spots in the LEED, we find strong evidence for a bulk band structure in 5 nm thick SrIrO₃(001) thin films grown on SrTiO₃(001). This evidence for band structure is seen in the binding energy shifts of the occupied states that are dependent on photon energy, as seen in Figure 2a. This is characteristic of bulk character. For the state near the top of the valence band, these disperse, i.e.

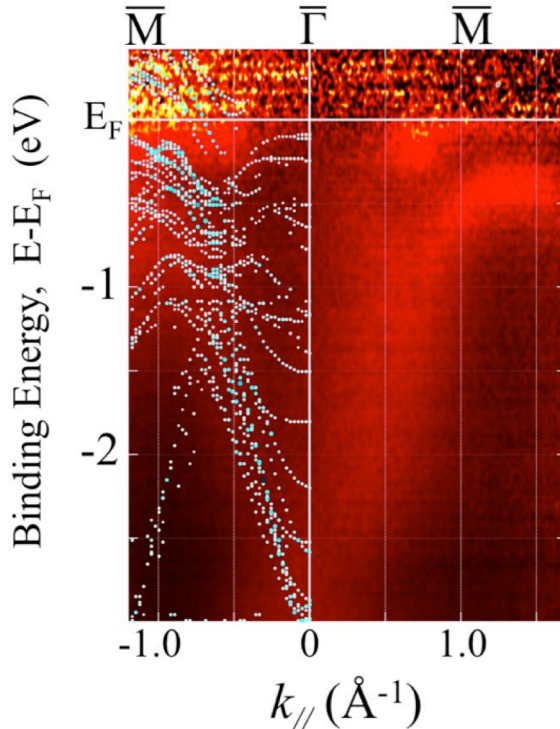


Figure 1. The experimental valence band electronic structure of a 5 nm thick orthorhombic SrIrO₃(001) thin film as derived from angle-resolved photoemission, taken at room temperature with a photon energy of 150 eV. Superimposed on experiment are the results from the DFT calculated band structure, on the left (light blue circles mark a large contribution to the spectral weight). Taken from [1].

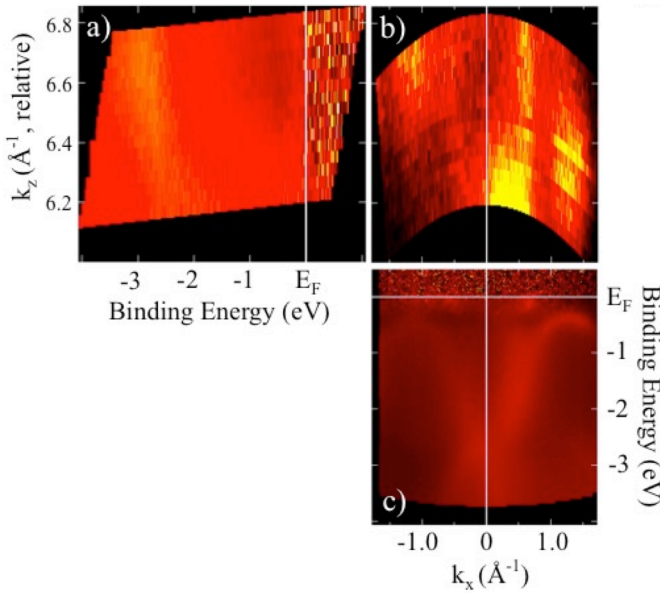


Figure 2. The photon energy dependence of $\text{SrIrO}_3(001)$ thin films clean surface, a) for k_z mapping, b) for k_x-k_z mapping, and c) for k_x -mapping. The measurement was performed at room temperature.

interacts with the $\text{SrIrO}_3(001)$ thin film. This is exactly what is observed with deposition of a Pd (palladium) overlayer deposited on $\text{SrIrO}_3(001)$ thin films grown on $\text{SrTiO}_3(001)$, as seen in Figure 3. Figure 3 shows the experimental electronic band structure for $\text{SrIrO}_3(001)$ thin films grown on $\text{SrTiO}_3(001)$ before and after the deposition of Pd deposited. The observed band structure before and after Pd deposition are very much the same. This indicates that the Pd

overlayer does not wet the SrIrO_3 interface and the interaction between Pd and SrIrO_3 surface layer, known to be dominated by Sr-O [1], is weak.

These measurements were taken on SrIrO_3 samples prepared by off-axis RF magnetron sputtering, grown on strontium titanate (SrTiO_3) as described in elsewhere [1]. The experimental band structure data were taken at the HiSOR, BL-1, using High Resolution Angle Resolved Photoemission Spectroscopy (HR-ARPES), at various photon energies.

References

- [1] Prescott E. Evans, Takashi Komesu, Le Zhang, Ding-Fu Shao, Andrew J. Yost, Shiv Kumar, Eike F. Schwier, Kenya Shimada, Evgeny Y. Tsymbal, Xia Hong, and P. A. Dowben, AIP Advances **10**, (2020) 045027

have a wave vector dependence that varies with photon energy indicative of a bulk character, as plotted in Figure 2b. The dispersions of these states match those bands seen near the top of the valence band as a function of polar angle, as in Figure 2c. Figure 2 shows the angle-resolved photoemission of $\text{SrIrO}_3(001)$ thin films grown on $\text{SrTiO}_3(001)$ has wave vector dependence both in-plane and out of plane; as a function of wave vector in-plane (i.e. k_x , as in Figure 2c), and also dependent on wave vector along the surface normal (i.e. k_z , as in Figure 2a).

If $\text{SrIrO}_3(001)$ thin films grown on $\text{SrTiO}_3(001)$ is metallic, then band offsets due to band bending are unlikely with a metal that weakly

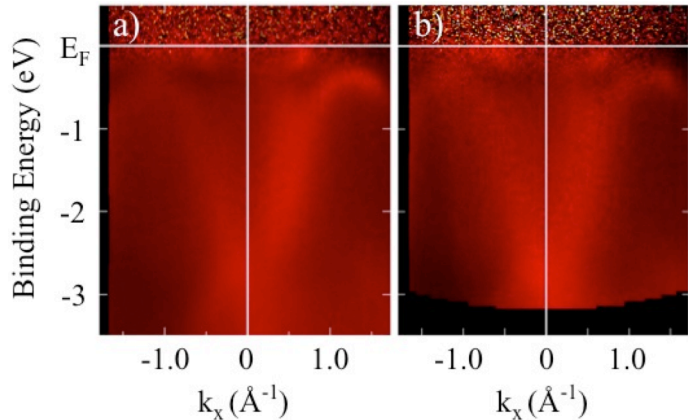


Figure 3. The comparison of electronic band structure of a) clean $\text{SrIrO}_3(001)$ before (a) and after (b) the deposition of a thin Pd adlayer.

High-resolution ARPES and Pressure Dependent Magneto-transport Study of BiSbTe₃

Vinod K. Gangwar^{a, #}, Shiv Kumar^{b, #}, Mahima Singh^a, Labanya Ghosh^a, Zhang Yufeng^{c, d}, Yogendra Kumar^{a,e}, Prashant Shahi^f, Swapnil Patil^a, Eike F. Schwier^b, Kenya Shimada^b, Yoshiya Uwatoko^c, Anup K. Ghosh and Sandip Chatterjee^{a,*}

^a*Department of Physics, Indian Institute of Technology (BHU) Varanasi 221005*

^b*Hiroshima Synchrotron Radiation Center, Hiroshima University, Higashi-Hiroshima City, 739-0046 Japan*

^c*Institute for Solid State Physics, University of Tokyo, Kashiwa, Chiba 277-8581, Japan*

^d*School of Physics and Key Laboratory of MEMS of the Ministry of Education, Southeast University, Nanjing 211189, China*

^e*School of Physical Sciences, University of Chinese Academy of Sciences, Beijing 100190, China*

^f*Department of Physics, D.D.U. Gorakhpur University, Gorakhpur 273009*

Keywords: Topological insulator, magnetism, pressure-induced superconductivity.

Topological insulator (TI) is a new quantum state of matter in condensed matter physics which has attracted huge attention because of their unique properties and potential technological applications such as quantum computation, spintronics and low power-dissipation electronic devices [1-6]. Bi₂Se₃, Bi₂Te₃ and Sb₂Te₃ are most studied 3D TIs, but so far very few reports are available on BiSbTe₃ TI compounds [7]. Usually, the conductivity of Bi₂Te₃ and Sb₂Te₃ shows n-type and p-type behavior respectively due to the formation of Te-vacancies and antisite defects [4, 8-10].

In this report, we have characterized the single crystal of BiSbTe₃ sample by ARPES technique to examine the surface states thoroughly and also measured transport properties with the variation of magnetic field and pressure. The single crystal BiSbTe₃ 3D TI sample was grown by a modified Bridgman method as has been reported elsewhere [11].

To probe the Dirac point and the surface states of BiSbTe₃, the ARPES experiment was performed by Laser-ARPES at the Hiroshima Synchrotron Radiation Center (HiSOR) using s-polarized light of 6.45 eV and measured with a hemispherical analyzer (VG Scienta SES R4000) at 20 K and 60 K [12]. The sample was cleaved in-situ at \sim 22 K in an ultrahigh vacuum below 5×10^{-9} Pa.

To investigate the electronic structure of this compound we have carried out the ARPES measurements as shown in Figs. 1 and 2. These measurements were carried out at 20 K and 60 K respectively. Fig. 1 and Fig. 2 represent the ARPES spectra as a coloured scale at 20 K and 60 K respectively. These images show the BVB of the compound forming a V-shaped valley like bulk bandgap region around the Γ -point in the Brillouin zone and the topological surface state (TSS) residing inside it as observed earlier [13-14]. The sharpness of the linear dispersion of the TSS reveals a good quality of the sample as well as the high energy and momentum resolution of the laser ARPES spectra. Quite interestingly we are able to discern the unoccupied part of the Dirac cone (DC) related to the TSS above E_F at 60 K due to the thermal broadening of the Fermi distribution function. The DP is seen to lie near E_F in this compound which happens to be an ideal condition for the technological exploitation of the topological properties of the TSS. This is important because the parent compounds Bi₂Te₃ and Sb₂Te₃ are mainly of n-type and p-type [8-10]. Doping Sb for Bi is expected to tune the DP at E_F for some of the intermediate composition. Accordingly, when we doped Sb in place of Bi halfway, we could realize a rare and important feat of tuning the DP to E_F . Thus the surface of this particular compound could potentially prove to be useful in realizing the promises of the TSS for practical applications. Surprisingly, the transport properties for this compound show a p-type behavior which is difficult to be understood entirely from the states near DP. From our ARPES spectra, we observe a finite contribution from the BVB towards E_F which is due to its specific band dispersion enclosing a valley type of bulk bandgap containing the DP. Thus when E_F is at the DP the surrounding peaks from the BVB simultaneously also cross E_F giving rise to a net p-type electrical transport in this compound since the states of the BVB have a p-type dispersion. Nevertheless, it is important to investigate further, the methods of tapping the DP towards technological applications.

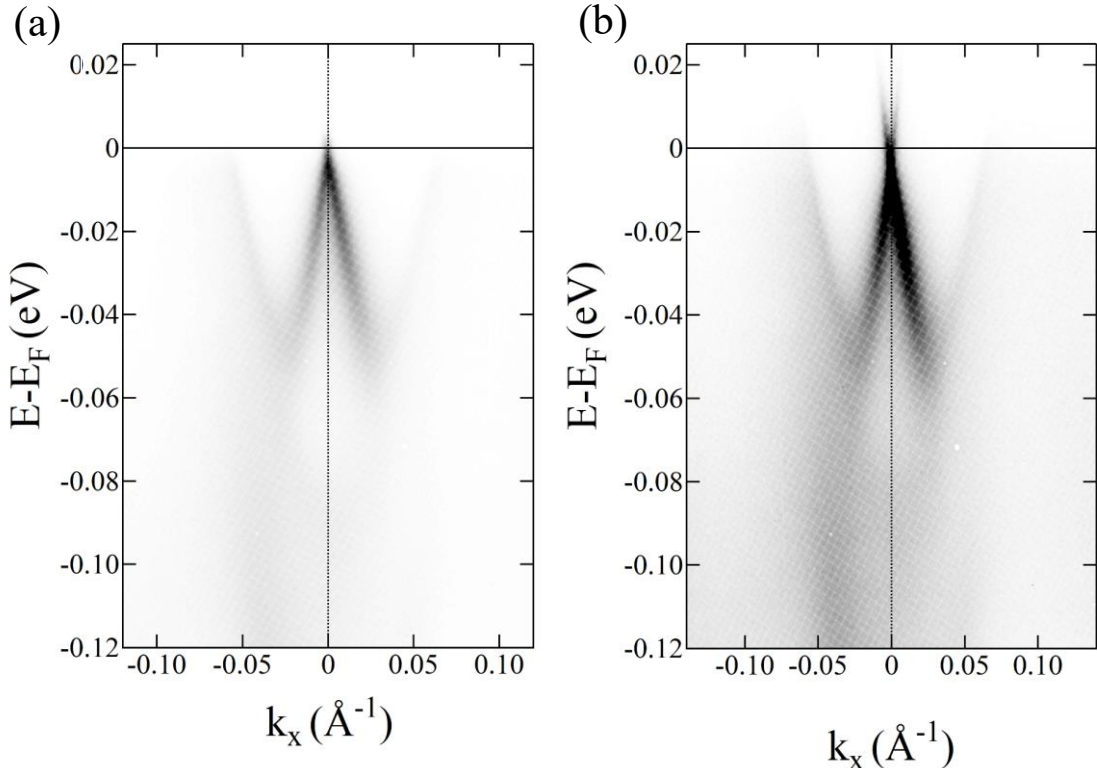


FIGURE 1. (a), (b) ARPES spectra displayed as a grayscale image at T=20K and 60K respectively.

In summary, we have synthesized and study the bulk and surface state electronic properties of BiSbTe₃ using Laser-ARPES. We have also investigated the magnetotransport properties and effect of external pressure on BiSbTe₃. It is observed that with the increase of pressure resistance decreases and at a value of 8 GPa a sharp drop in resistivity is observed which indicates the occurrence of superconductivity. With further increase of pressure, the superconducting transition temperature (T_c) increases and at 14 GPa it shows the maximum T_c (~3.3 K).

REFERENCES

1. M.Z. Hasan and C.L. Kane, *Reviews of Modern Physics* 82, 3045 (2010).
2. C.-Z. Chang, J. Zhang, X. Feng, J. Shen, Z. Zhang, M. Guo, K. Li, Y. Ou, P. Wei, L.-L. Wang, Z.-Q. Ji, Y. Feng, S. Ji, X. Chen, J. Jia, X. Dai, Z. Fang, S.-C. Zhang, K. He, Y. Wang, L. Lu, X.-C. Ma, and Q.-K. Xue, *Science* 340, 167 (2013).
3. J.E. Moore, *Nature* 464, 194 (2010).
4. Y. Xia, D. Qian, D. Hsieh, L. Wray, A. Pal, H. Lin, A. Bansil, D. Grauer, Y.S. Hor, R.J. Cava, and M.Z. Hasan, *Nature Physics* 5, 398 (2009).
5. D. Hsieh, Y. Xia, D. Qian, L. Wray, J.H. Dil, F. Meier, J. Osterwalder, L. Patthey, J.G. Checkelsky, N.P. Ong, A.V. Fedorov, H. Lin, A. Bansil, D. Grauer, Y.S. Hor, R.J. Cava, and M.Z. Hasan, *Nature* 460, 1101 (2009).
6. H. Zhang, C.-X. Liu, X.-L. Qi, X. Dai, Z. Fang, and S.-C. Zhang, *Nature Physics* 5, 438 (2009).
7. S.-M. Huang, P.-C. Wang, C. Lin, S.-Y. You, W.-C. Lin, L.-J. Lin, Y.-J. Yan, S.-H. Yu, and M.C. Chou, *Applied Physics Letters* 112, 203103 (2018).
8. D.O. Scanlon, P.D.C. King, R.P. Singh, A.D.L. Torre, S.M. Walker, G. Balakrishnan, F. Baumberger, and C.R.A. Catlow, *Advanced Materials* 24, 2154 (2012).
9. P. Lošťák, Z. Starý, J. Horák, and J. Pancíř, *Physica Status Solidi (a)* 115, 87 (1989).
10. D. Hsieh, Y. Xia, D. Qian, L. Wray, F. Meier, J.H. Dil, J. Osterwalder, L. Patthey, A.V. Fedorov, H. Lin, A. Bansil, D. Grauer, Y.S. Hor, R.J. Cava, and M.Z. Hasan, *Physical Review Letters* 103, (2009).
11. R. Singh, V.K. Gangwar, D.D. Daga, A. Singh, A.K. Ghosh, M. Kumar, A. Lakhani, R. Singh, and S. Chatterjee, *Applied Physics Letters* 112, 102401 (2018).
12. H. Iwasawa, E. F. Schwier, M. Arita, A. Ino, H. Namatame, M. Taniguchi, Y. Aiura, and K. Shimada, *Ultramicroscopy* 182, 85 (2017).
13. Zhang, C.-Z. Chang, Z. Zhang, J. Wen, X. Feng, K. Li, M. Liu, K. He, L. Wang, X. Chen, Q.-K. Xue, X. Ma, and Y. Wang, *Nature Communications* 2, (2011).
14. X. He, T. Guan, X. Wang, B. Feng, P. Cheng, L. Chen, Y. Li, and K. Wu, *Applied Physics Letters* 101, 123111 (2012).

Ex-situ/in-situ soft x-ray absorption investigation towards passivation behavior of Ti

Ying Jin^a, Qingrui Wang^a, FeiFei Huang^a, Yi-Tao Cui^b, Hiroaki Yoshida^c and Takashi Tokushima^d

^aNational Center for Materials Service Safety, University of Science and Technology Beijing, No.30, Xueyuan Road, Haidian District, Beijing P.R. CHINA

^bSANKA High Technology Co. Ltd. 90-1, Kurimachi, Shingu-machi, Tatsuno, Hyogo, 679-5155, Japan

^cDepartment of Physical Science, Hiroshima University, 1-3-1 Kagamiyama, Higashi-Hiroshima, 739-8526, Japan

^d MAX IV Laboratory Lund University, Box 117, 221 00 Lund, Sweden

Keywords: TA2, TA15, reference titanium oxides, passive film, corrosion resistance

Due to the superb properties like low density, high strength, excellent biocompatibility, super-plasticity, and high corrosion resistance, titanium and titanium alloys are widely used in dent implants[1], biomedicine[2,3], aviation industry[4,5], batteries[6], healthcare goods[7] and other fields. The good corrosion resistance of titanium and titanium alloys is attributed to the oxide film formed on the metal surface.

To investigate the properties and formation mechanism of oxide film of titanium and its alloys, the researches on the passivation and corrosion of titanium and titanium alloy were carried out. The nature, composition, and thickness of the oxide film depends on the environmental conditions[8]. In this study, the effects of potential and time on formation and dissolution mechanisms of oxide film were researched comprehensively. As shown in figure 1, we have chosen commercial samples of TA15 (Ti-6.5Al-2Zr-1Mo-1V) and TA2 to do potentiostatic control under different potentials and times in 0.5 M sulfuric and 0.1 M hydrochloric acid to form the oxide film.

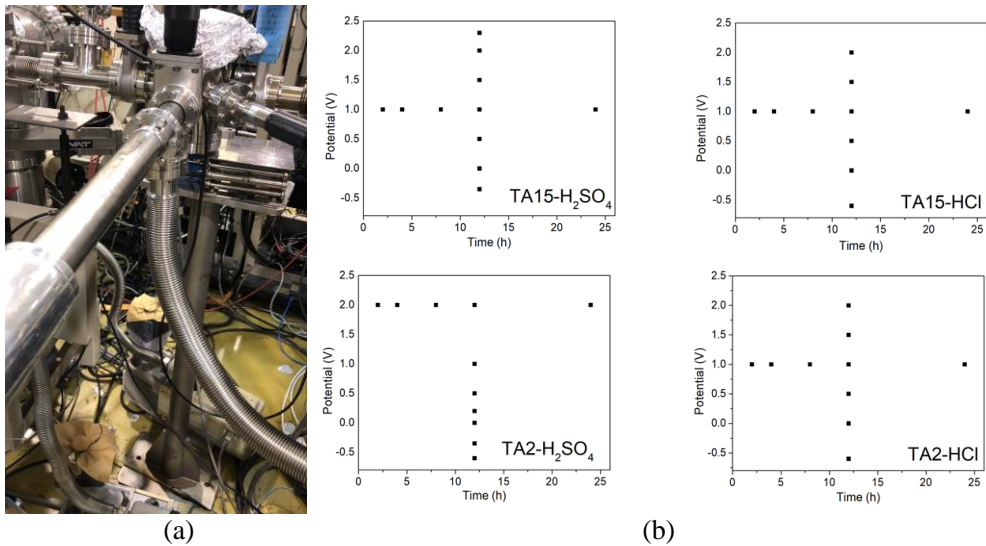


FIGURE 1. (a)The vacuum sample chamber installed at BL-6and (b) the potential and potentiostatic control conditions for TA15 and TA2.

A vacuum sample chamber was designed and installed on BL-6, which can greatly reduce the time for changing sample (8-10 samples for once) and enhance the signal noise ratio. By using this chamber, the quality of the spectra obtained has been improved a lot (Figure 2). X-ray Absorption Specctroscopy (XAS) was used to obtain the spectra of reference titanium oxides (as the figure 2 shows) and characterize the complex compositions and chemical states within the oxide film. Besides, X-ray Photoelectron Spectroscopy (XPS), Auger Electron Spectroscopy (AES), Electrochemical impedance spectroscopy (EIS) and Mott-schottky were employed to investigate the formation mechanism and properties of oxide film of titanium and its alloys. Corresponding results are under preparation for another manuscript.

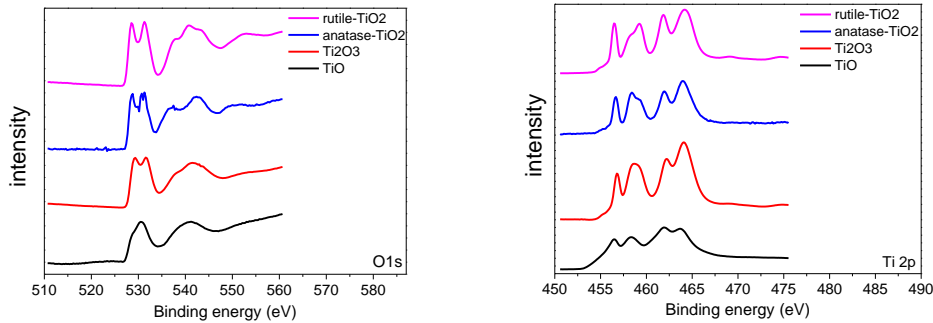


FIGURE 2. The XAS (Ti 2p and O 1s) of the prepared reference titanium oxides.

The main findings are summarized as follows:

- There is a positive correlation between the thickness of oxide films and applied potentials. However, thicker oxide film does not represent better corrosion resistance, the structure and valence state of the oxide film are of great importance.
- TiO₂ is the predominant oxide at the surface of oxide films, and the formation of that is promoted by the increase of applied potential.
- Anatase-TiO₂ is more dominant under natural solution environment or relatively low applied potential.
- The compact and stable passive film formed in passive region under higher applied potential has better corrosion resistance.

Besides, the XAS data of TC4 samples polarized in H₂SO₄ solution obtained last time (April 2019) have been summarized and illustrated in manuscript “Influences of formation potential on oxide film of TC4 in 0.5 M sulfuric acid”, and this manuscript has been submitted to the journal “Applied Surface Science” (Figure 3). The XAS data of other samples are analyzed, and preparing for other manuscripts.

| Applied Surface Science Influences of formation potential on oxide film of TC4 in 0.5 M sulfuric acid —Manuscript Draft— | |
|--|--|
| Manuscript Number: | |
| Article Type: | Full Length Article |
| Keywords: | surface passivation; titanium alloy TC4; electrochemical passivation; oxide film; Corrosion resistance; |
| Corresponding Author: | Ving-Jin Beijing University of Science and Technology Beijing Beijing, CHINA |
| First Author: | Gengru Wang |
| Order of Authors: | Fefei Huang Yi-Tao Cui Hiroaki Yoshida Lai Wen Ving-Jin |
| Abstract: | Correlation between film formation potential and the thickness, valence state and corrosion resistance of oxide film on TC4 (Ti-6Al-4V) in 0.5 M sulfuric acid is investigated. The results show that the formation potential has a significant influence on the oxide film properties. The X-ray photoelectron spectroscopy and Auger electron spectrum analyses illustrate that the formation of thicker and higher valence state oxide film at higher formation potential. The results also show that the oxide film generated at higher potentials in passive region show good protections, and the corrosion resistance of the passive film is significantly improved. The X-ray absorption spectra of the 1.50 V film in oxide films generated under above conditions transforms from anatase to rutile with the increasing of the formation potential, confirmed by comparing with the X-ray absorption spectroscopy of reference oxides. |

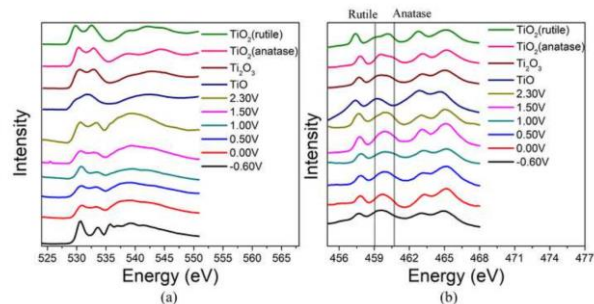


FIGURE 3. The detail information and XAS data of the submitted manuscript.

REFERENCES

- V.A. Alves, R.Q. Reis, I.C.B. Santos, D.G. Souza, T.D.F. Gonçalves, M.A. Pereira-Da-Silva, A. Rossi, L.A. Da Silva, In situ impedance spectroscopy study of the electrochemical corrosion of Ti and Ti-6Al-4V in simulated body fluid at 25 °C and 37 °C, Corros. Sci. 51 (2009) 2473–2482.
- N. Sakaguchi, M. Niinomi, T. Akahori, J. Takeda, H. Toda, Relationships between tensile deformation behavior and microstructure in Ti-Nb-Ta-Zr system alloys, Mater. Sci. Eng. C. 25 (2005) 363–369. <https://doi.org/10.1016/j.msec.2004.12.014>.
- G. He, J. Eckert, Q.L. Dai, M.L. Sui, W. Löser, M. Hagiwara, E. Ma, Nanostructured Ti-based multi-component alloys with potential for biomedical applications, Biomaterials. 24 (2003) 5115–5120. [https://doi.org/10.1016/S0142-9612\(03\)00440-X](https://doi.org/10.1016/S0142-9612(03)00440-X).
- C. Lin, Z. Liu, Y. Zhao, Theoretical research on phase transformations in metastable β-titanium alloys, Metall. Mater. Trans. A Phys. Metall. Mater. Sci. 40 (2009) 1049–1058. <https://doi.org/10.1007/s11661-009-9798-0>.
- Y.W. Xun, M.J. Tan, Applications of superplastic forming and diffusion bonding to hollow engine blades, J. Mater. Process. Technol. 99 (2000) 80–85. [https://doi.org/10.1016/S0924-0136\(99\)00377-5](https://doi.org/10.1016/S0924-0136(99)00377-5).
- T.B. Kim, W.H. Jung, H.S. Ryu, K.W. Kim, J.H. Ahn, K.K. Cho, G.B. Cho, T.H. Nam, I.S. Ahn, H.J. Ahn, Electrochemical characteristics of Na/FeS₂ battery by mechanical alloying, J. Alloys Compd. 449 (2008) 304–307. <https://doi.org/10.1016/j.jallcom.2006.02.113>.
- M. Niinomi, Recent research and development in titanium alloys for biomedical applications and healthcare goods, Sci. Technol. Adv. Mater. 4 (2003) 445–454.
- Perini N, Corradini P G, Nascimento V P, et al. Characterization of AISI 1005 corrosion films grown under cyclic voltammetry of low sulfide ion concentrations[J]. Corrosion Science, 2013, 74(Complete):214-222.

X-ray Absorption Spectroscopy of Single Layer Graphene on Metal Supports

Masaru Kato,^{a,b} Keisuke Nishiyama,^b Sayuki Oka,^b Satoshi Yasuda,^c
Shin-ichi Wada,^{d,e} Hiroaki Yoshida^{d,e} and Ichizo Yagi^{a,b}

^a*Faculty of Environmental Earth Science and ^bGraduate School of Environmental Science, Hokkaido University, N10W5, Kita-ku, Sapporo 060-0810, Japan*

^c*Research Group for Nanoscale Structure and Function of Advanced Materials,*

Advanced Science Research Center, Japan Atomic Energy Agency, Tokai, Ibaraki 319-1195, Japan

^d*Physics Program, Graduate School of Advanced Science and Engineering, 1-3-1 Kagamiyama, and*

^e*Hiroshima Synchrotron Radiation Center, Hiroshima University, 2-313 Kagamiyama, Higashi-Hiroshima, 739-0046 Japan*

Keywords: single layer graphene, chemical vapor deposition, gold, X-ray absorption spectroscopy.

Graphene is a two-dimensional carbon sheet and its electronic properties motivate us to develop new graphene-based electronic and optoelectronic devices. To produce such devices, the fabrication of large-area, defect-free graphene onto a desired substrate is necessary. Chemical vapor deposition (CVD) methods allow for the preparation of single layer graphene on metal substrates. The CVD-grown single layer graphene on Cu can be transferred to other substrates using a polymer film of poly(methyl methacrylate) (PMMA). The property of CVD and transferred graphene is strongly influenced by the underlying substrate, mechanical strain, charge densities and impurities from transfer processes, which can be investigated by Raman spectroscopy and C1s X-ray absorption spectroscopy (XAS) [3,4].

We prepared CVD and transferred graphene supported on gold and performed Raman spectroscopy, electrochemistry and C1s XAS of them to understand the impact of the different preparation procedure on the electronic property of graphene supported on gold. Gold substrates are relatively inert even in acidic media and would be used for covalent functionalization of graphene, which resulting in the opening of a bandgap and shifting of the Fermi level [4]. The CVD graphene on polycrystalline gold (CVD-Gr/Au) was prepared according to the literature [1]. To prepare the transferred graphene on gold (Tr-Gr/Au), graphene was synthesized on a copper foil by CVD and then transferred to a gold substrate using PMMA. The formation of single layer graphene for CVD-Gr/Au and Tr-Gr/Au were confirmed by Raman spectroscopy. Electrochemical measurements of CVD-Gr/Au and Tr-Gr/Au in an aqueous electrolyte solution containing 4-nitrobenzenediazonium, HCl and NaNO₂ revealed that more functional groups were tethered into Tr-Gr/Au than CVD-Gr/Au, indicating that Tr-Gr/Au is more reactive than CVD-Gr/Au. We also performed C1s angle-dependent XAS of CVD-Gr/Au and Tr-Gr/Au at BL-13, HiSOR. Two characteristic peaks at ca. 285.5 and 291.6 eV were observed and are associated with π^* C=C and σ^* C-C, respectively. The σ^* C-C peak position for Tr-Gr/Au is slightly shifted to lower photon energy than that for CVD-Gr/Au, which could be related to substrate-induced strain effects [3]. We also observed an intense peak of π^* C=O impurity states at 288.7 eV for Tr-Gr/Au. These findings suggest that mechanical strain and/or C=O impurities caused by the graphene transfer process could result in the higher electrochemical reactivity for Tr-Gr/Au.

REFERENCES

1. S. Yasuda, R. Kumagai, K. Nakashima, K. Murakoshi, *J. Phys. Chem. Lett.*, **6**, 3403 (2015).
2. S. Yasuda, K. Tamura, T. Terasawa, M. Yano, H. Nakajima, T. Morimoto, T. Okazaki, R. Agari, Y. Takahashi, M. Kato, I. Yagi, H. Asaoka, *J. Phys. Chem. C*, **124**, 5300 (2020).
3. W.Y. Rojas, A.D. Winter, J. Grote, S.S. Kim, R.R. Naik, A.D. Williams, C. Weiland, E. Principe, D.A. Fischer, S. Banerjee, D. Prendergast, E.M. Campo, *Langmuir*, **34**, 1783 (2018).
4. Q.H. Wang *et al.*, *Nature Chem.*, **4**, 724 (2012).

Soft X-ray absorption spectra of copper ion complexes included in cyclodextrin

Yoshihiko Nakamura^a, Ryuta Nobue^a and Hiroaki Yoshida^{a, b}

^a*Department of Physical Science, Hiroshima University,
1-3-1 Kagamiyama, Higashi-Hiroshima, 739-8526 Japan.*
^b*Hiroshima Synchrotron Radiation Center, Hiroshima University,
2-313 Kagamiyama, Higashi-Hiroshima, 739-0046 Japan.*

Keywords: Soft X-ray absorption spectroscopy, cyclodextrin, copper ion, inclusion

Cyclodextrin (CD) is one of polysaccharides composed of several D-glucoses. It has a cylindrical shape and the number of linked D-glucoses decides a toric diameter. The units of 6, 7, and 8 D-glucoses are well-known as α -, β - and γ -CD, respectively. The CD has a special property to take other materials into an internal cavity and such a phenomenon is called “inclusion”. Although a lot of studies on structures of CD inclusion compounds have been made up to now, there is little knowledge about the electronic states of them. $\text{Cu}_2(\text{OH})_2@\alpha\text{-CD}$ ($\text{Cu}@\alpha\text{-CD}$) and $\text{Cu}_2(\text{OH})\text{O}@\beta\text{-CD}$ ($\text{Cu}@\beta\text{-CD}$) are well-known CD inclusion compounds [1]. By measuring soft X-ray absorption spectra (SXAS) at both O K-edge and Cu L-edge, the difference in inclusion structures by CD size are discussed in detail.

Soft X-ray absorption experiments were performed at the end-station of BL6 [2]. The absorption spectra of α -, β - and γ -CD at the O K-edge are shown in Figure 1. These spectra resemble very much. The difference by the number of glucose which constitutes the CD ring is not observed. The absorption spectra of $\text{Cu}@\alpha\text{-CD}$, $\text{Cu}@\beta\text{-CD}$, and $\text{Cu}@\gamma\text{-CD}$ at the O K-edge are shown in Figure 2. On the low energy side of the spectra, the shoulder structures which are absent in the CD spectra are observed. This is regarded as contribution by the newly produced chemical bonds of copper ion complex included in CD.

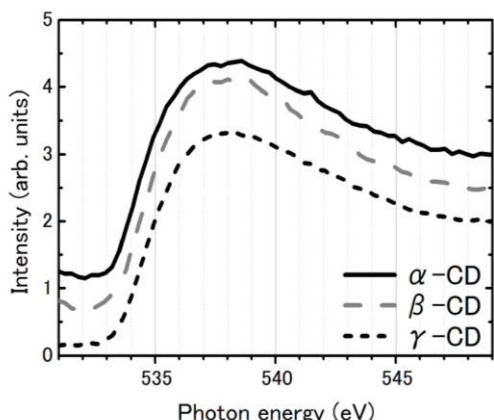


FIGURE 1. X-ray absorption spectra of α -, β - and γ -CD at the O K-edge.

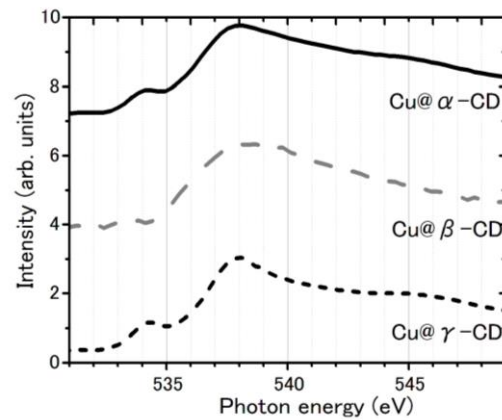


FIGURE 2. X-ray absorption spectra of $\text{Cu}@\alpha\text{-CD}$, $\text{Cu}@\beta\text{-CD}$, and $\text{Cu}@\gamma\text{-CD}$ at the O K-edge.

REFERENCES

1. Y. Matsui *et al.*, *Bull. Chem. Soc. Jpn.*, **48** (1975) 2187-2191.
2. H. Yoshida *et al.*, *J. Electron Spectrosc. Relat. Phenom.*, **144-147**(2005) 1105-1108.

Electronic Structures of Mg-Zn-Gd Alloys with Long-Periodic Stacking Order

Shinya Hosokawa,^a Jens Rüdiger Stellhorn,^{a,‡} Kentaro Kobayashi,^b
Kenji Maruyama,^b and Hitoshi Sato^c

^a*Department of Physics, Kumamoto University, Kumamoto 860-8555*

^b*Graduate School of Science and Technology, Niigata University, Niigata 950-2181*

^c*Hiroshima Synchrotron Radiation Center, Hiroshima University, Higashi-Hiroshima 739-0046*

[‡]*Present address: Department of Applied Chemistry, Hiroshima University, Higashi-Hiroshima 739-8527*

Keywords: LPSO structure, Impurities, Electronic structure, Chemical states

A series of Mg alloys [1] with the microstructures containing a synchronized long-period stacking ordered (LPSO) structure, the so-called KUMADAI Magnesium, has been attracted considerable attention owing to the excellent mechanical properties. By adding a small amount of Zn and rare-earth (Y or Gd) impurities, the soft, flammable, and light-weighted Mg metal becomes much strong and non-flammable. By taking such excellent properties, the new Mg alloys can be used for body materials of subways and even aircrafts.

For the microstructure of these materials, a scanning transmission electron microscope image was obtained by Abe et al. [2], which revealed that impurity atoms are enriched at the changes in the stacking order, i.e., the concentrations of the impurities are synchronized with the modulation of the lattice stacking order. Excellent mechanical properties of the LPSO phases were understood owing to such interesting microstructures, i.e., kink bands in the LPSO structures produce the hardness and durability of the Mg alloys.

In 2015 and 2016, we measured photoemission and inverse-photoemission spectroscopy (PES and IPES) at HisOR on polycrystalline Mg₇₅Zn₁₀Y₁₅, Mg₈₅Zn₆Y₉, and Mg₉₇Zn₁Y₂ LPSO alloys together with the reference pure polycrystalline Mg. Core-level PES experiments were also carried out to study the chemical nature of Mg, Zn, and Y elements [3]. The most prominent result was that the Y 3d core spectra exhibit three doublets in Mg₉₇Zn₁Y₂, while mostly only one in the heavier doped alloys, reflecting a coexistence of three different sites of the Y atoms concerning the Zn₆Y₈ L₁₂ clusters [4].

In this study, we investigate electronic structures of a different series of Mg-Zn-Gd LPSO alloys by using PES and IPES. Core-level PES measurements were also carried out to study the chemical nature of the constituent Mg, Zn, and Gd elements.

The Mg₉₇Zn₁Gd₂ and Mg₉₅Zn₂Gd₃ LPSO samples were manufactured at Magnesium Research Center, Kumamoto University using a usual slow cooling method in a cylindrical carbon crucible. The composition of the sample was confirmed to be nominal value by an electron-probe micro-analysis equipment. The PES measurements were carried out using high-resolution PES spectrometer installed at BL-7 of HisOR. The measurements were performed in the incident photon energy range of 40-400 eV to obtain valence-band DOS. We also measured core-level PES spectra for the Mg 2s (88.7 eV) and 2p (49.50-49.78 eV), Zn 3p (88.6-91.4 eV), and Gd 4d (142.6-147.5 eV) levels to examine the chemical states around each constituent element. The IPES spectra were also obtained using the RIPES spectrometer at HisOR to measure the conduction-band DOS.

Figure 1 shows PES and IPES spectra of polycrystalline Mg₉₅Zn₁Gd₂ (left panel) and Mg₉₇Zn₂Gd₃ (right panel) alloys. The PES spectra were displayed at the incident photon energy, $h\nu$, from 60 to 150 eV from bottom to top. The PES curves are shifted each other by 0.5 for the clarity. The magnitudes of the PES spectra are normalized to the maximum values at about -6 eV of each spectrum. The Zn 3d core level peaks are seen at about -10 eV, and the intensity rapidly increases with increasing $h\nu$ owing to the rapid increase of the Zn 3d photo-ionization cross-section and the decrease of the Mg 3s one. The IPES spectra are scaled so as to match the DOS at the Fermi energy, E_F , and the spectra are similar to that of pure Mg.

Figure 2 shows the Gd 4d core-level PES spectra of polycrystalline Mg₉₇Zn₁Gd₂ (lower) and Mg₉₅Zn₂Gd₃ (upper) alloys measured at $h\nu = 400$ eV. The spectra are rather broad and may be composed of plural sites. This tendency becomes clear with increasing the impurity concentration. The decomposition of the Gd 4d core-level PES spectra is now in progress.

The authors acknowledge Professor Y. Kawamura and Professor M. Yamasaki for providing the samples and

valuable discussion. This work was supported by a Grant-in-Aid for Scientific Research on Innovative Areas ‘Materials Science on Synchronized LPSO structure’ (No. 26109716) from the Japan Society for the Promotion of Science (JSPS). JRS gratefully acknowledges a financial support as Overseas Researcher under a JSPS fellowship (No. P16796).

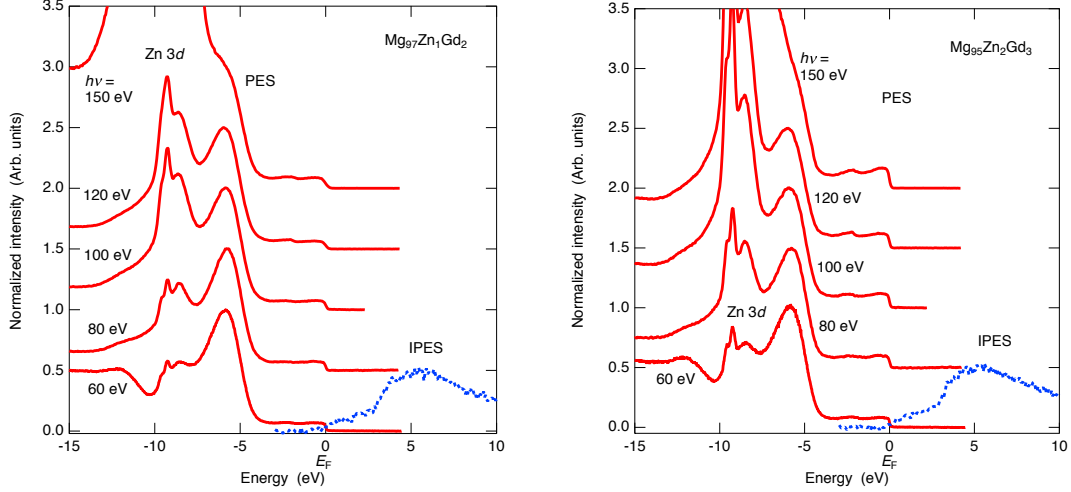


FIGURE 1. PES and IPES spectra of polycrystalline $\text{Mg}_{95}\text{Zn}_1\text{Gd}_2$ (left panel) and $\text{Mg}_{95}\text{Zn}_2\text{Gd}_3$ (right panel) alloys.

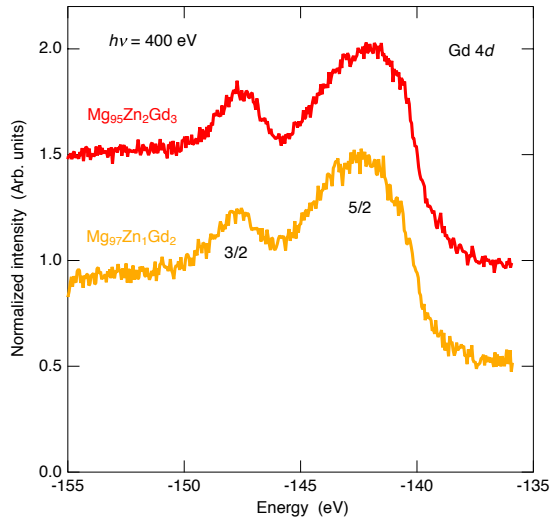


FIGURE 2. Gd 4d core-level PES spectra of polycrystalline $\text{Mg}_{97}\text{Zn}_1\text{Gd}_2$ (lower) and $\text{Mg}_{95}\text{Zn}_2\text{Gd}_3$ (upper) alloys.

REFERENCES

1. Y. Kawamura et al., *Mater. Trans.* **42**, 1172 (2001).
2. E. Abe et al., *Philos. Mag. Lett.* **91**, 690 (2011).
3. S. Hosokawa et al., *J. Alloys Compd.* **762**, 797 (2018).
4. D. Egusa and E. Abe, *Acta Mater.* **60**, 166 (2012).

Direct Observation of Electronic Structure of Cycloparaphenylenes

Kaname Kanai^a

^a Department of Physics, Faculty of Science and Technology, Tokyo University of Science, 2641 Yamazaki, Noda, Chiba 278-8510, Japan

Keywords: *n*-cycloparaphenylenes, Electronic structure

To date, countless π -conjugated molecules have been used in various electronic applications, such as in optoelectronic devices, light-harvesting devices and sensors. Most of these π -conjugated molecules are planar and have little diversity in their molecular backbones, limiting new molecular designs. The possibility of controlling the properties of molecules by employing non-planar backbones arose when *n*-cycloparaphenylenes ($[n]$ CPPs) (Fig. 1(a)) were first synthesized in 2008 [1].

Subsequent innovative synthesis strategies for this family of polycyclic aromatic hydrocarbons have been developed. $[n]$ CPP has a cyclic structure consisting of n benzene rings linked at their para-positions. These circularly aligned n phenylene units are the building blocks of armchair carbon nanotubes (CNTs) and have attracted much attention due to their potential for seeding the size-selective growth of CNTs. The $[n]$ CPP series is also fascinating for basic research, providing a good opportunity to study how the electronic structure of a π -conjugation system is modified by introducing strong strain into the molecular structure. The correlation between molecular structure and electronic structure is of great interest to both physical and synthetic chemists. The molecular structure of $[n]$ CPP is determined by the balance between energy gain due to delocalization of the π -electrons and the strain energy of the distorted molecular structure, resulting in conflict between stabilization of the electronic system and elastic strain of the molecular backbone. The distortion of each phenylene unit markedly influences their aromaticity, in analogy with fullerenes and CNTs, resulting in the unique reactivity of non-planar π -conjugated molecules. The mechanism by which the physical and chemical properties of a molecule are impacted by distortion can be understood from its electronic structure. $[n]$ CPP has an unusual electronic structure quite different from that of most other π -conjugated molecules and is due to its cyclic structure. For example, the energy gap between the highest occupied molecular orbital (HOMO) and the lowest unoccupied molecular orbital (LUMO) of $[n]$ CPP increases as the number of linked phenylene groups n increases. Density functional theory (DFT) calculations show that the HOMO-LUMO gap of $[n]$ CPP dramatically increases as n increases for n less than ~15, above which it approaches that of polyphenylenes (n P) (Fig. 1(b)). The evaluated HOMO-LUMO gaps of n P and $[n]$ CPPs are plotted as a function of n in Fig. 2. The HOMO-LUMO gap of $[n]$ CPP is dependent on the molecular size, which is opposite to that of n P. The HOMO-LUMO gap of $[n]$ CPP increases as n increases although that of n P decreases as n increases. The HOMO-LUMO gaps for n P and $[n]$ CPP begin to converge as n increases, indicating convergence at the limit of very long molecular chain lengths. Even-odd effects on the HOMO-LUMO gaps of n P and $[n]$ CPP were previously reported [2]. This n dependence of the HOMO-LUMO gap of $[n]$ CPP can be explained by considering the correlation between the degree of strain in the molecular structure and the degree of distortion of the wave functions of the π -orbitals in $[n]$ CPP.

Figure 3 shows the dihedral angle θ plotted against n for n P and $[n]$ CPP ($n = 8, 9$ and 12). The representation

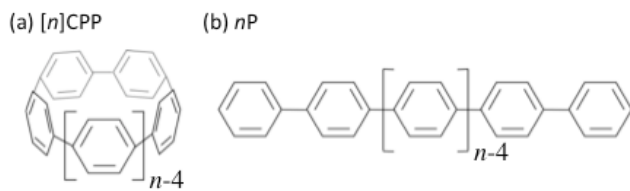


Figure 1. Molecular structure of $[n]$ CPP and n P.

of [8]CPP in the figure defines θ . Scatter data for each n represent the values of θ for each dihedral angle between two neighboring phenylene groups. The open diamonds connected by solid lines represent the average values of θ for each n . θ for nP remains around 36° and there is little dependence of θ , although the average value slightly decreases as the molecular size increases. In contrast, the average value of θ for $[n]CPP$ rapidly increases with increasing n and approaches the average value of θ for nP . This strange correlation between electronic states and molecular structure of $[n]CPPs$ will be clarified by photoelectron spectroscopy in this work.

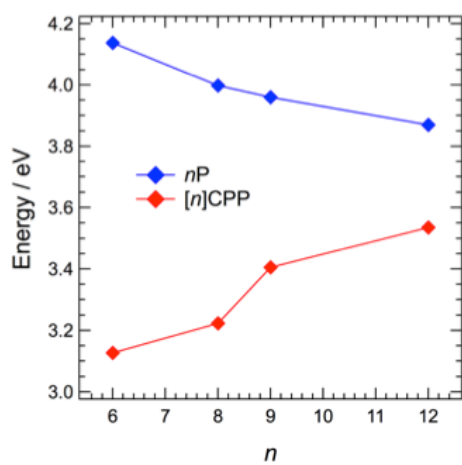


Figure 2. HOMO-LUMO gaps for nPs and $[n]CPPs$ calculated from the HOMO and LUMO energy levels.

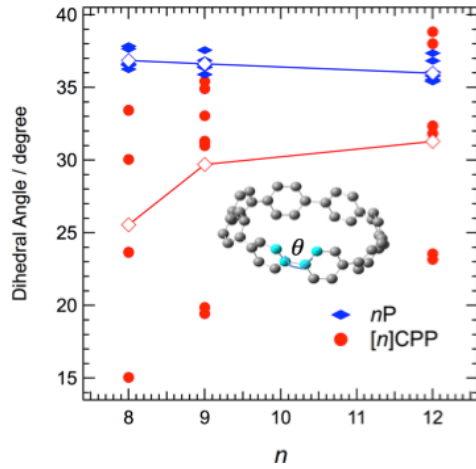


Figure 3. Calculated dihedral angle θ plotted as a function of n for nP (blue) and $[n]CPP$ (red). Open diamonds connected by solid lines represent the average values of θ for each n .

REFERENCES

1. R. Jasti, J. Bhattacharjee, J. B. Neaton and C. R. Bertozzi, *J. Am. Chem. Soc.*, 130, 17646–17647, (2008).
2. T. Iwamoto, Y. Watanabe, Y. Sakamoto, T. Suzuki and S. Yamago, *J. Am. Chem. Soc.*, 133, 8354–8361 (2011).

Electronic structures of Mn-based oxypnictides studied by photoemission spectroscopy

Atsushi Higashiya^a, Koya Nakagawa^b, Masashi Arita^c, Hitoshi Sato^c, Koichi Takase^d, and Atsushi Yamasaki^b

^a Faculty of Science and Engineering, Setsunan University, Neyagawa, Osaka 572-8508, Japan

^b Faculty of Science and Engineering, Konan University, Kobe, Hyogo 658-8501, Japan

^c Hiroshima Synchrotron Radiation Center, Hiroshima University, Higashihiroshima, Hiroshima 739-0046, Japan

^d College of Science and Technology, Nihon University, Chiyoda, Tokyo 101-8308, Japan

Keywords: manganese, oxypnictide, photoemission spectroscopy

Recently, mixed-anion compounds have been vigorously investigated as a candidate of new functional material. They have a large possibility to show new phenomena triggered by unique crystal structures which one can easily design in contrast to traditional oxides and nitrides. Most of the mixed-anion compounds are known to be artificially synthesized under controlled conditions. Meanwhile, their physical properties have not yet been cleared. A manganese-based oxypnictide LaOMnAs is one of mixed-anion compounds, which is composed of alternately stacked LaO/MnAs layers along the *c* axis. Mn ions are tetrahedrally surrounded by As ions [1]. LaOMnAs has an antiferromagnetic insulating phase at room temperature, whose Neel temperature (T_N) is 314K. According to the result of a neutron diffraction study, Mn 3d spins are antiferromagnetically aligned in the *a-b* plane but ferromagnetically along the *c* axis. If the Mn ions are assumed to be divalent, the magnetic moment would be $5 \mu_B$ per Mn²⁺ ion. However, the average value of the magnetic moment per Mn ion was estimated to be about $2.43 \mu_B$ at 290 K [2], suggesting that the valence number of the Mn ion is strongly deviated from the nominal value due to the hybridization between Mn 3d and As 4p states. The high T_N and small magnetic moment in LaOMnAs would indicate that this compound is located in the crossover regime between Mott and Slater insulators.

We have previously carried out the photoemission spectroscopy (PES) of LaOMnAs and BaMn₂As₂ utilizing hard x-ray (HX) of about 8 keV at room temperature [3] and compared our HXPES results with the results of the LDA+DMFT calculation. In the result, some discrepancies are found between the experimental and simulated spectra, which does not enable us to estimate some important parameters. Recently, it has been pointed out that the contribution of La 5p states to the valence-band (VB) spectrum in lanthanum compounds cannot be negligible in the HX region [4]. Therefore, the disagreement between our HXPES and the calculated spectra also may arise from the contribution of La 5p states to the VB spectrum.

In order to evaluate the contribution of the La 5p states to the VB spectrum in LaOMnAs, we performed the PES experiments at the beamline BL-07 of HiSOR with the photon energies ($h\nu$) of 50 and 200 eV at room temperature, where the photoionization cross section (PICS) of the La 5p states in the $h\nu$ range are relatively smaller than that in the HX range. The total energy resolutions at $h\nu = 50$ and 200 eV were set to about 50 and 250 meV, respectively. A polycrystalline sample of LaOMnAs was adopted for the measurement. Clean surface was obtained by fracturing *in situ* in ultrahigh vacuum of about 3×10^{-8} Pa just before the measurement.

The VB spectra obtained at $h\nu = 50$ and 200 eV are shown in Fig. 1(a). Some peaks and shoulders are marked as (a) - (e) with vertical lines. The spectrum at $h\nu = 50$ eV is more surface sensitive than that at $h\nu = 200$ eV because of the shorter escape depth of photoelectrons. The PICS ratio of Mn 3d, La 5p, O 2p, and As 4p is roughly 5 : 2 : 6 : 1 at $h\nu = 50$ eV and 10 : 2 : 2 : 1 at $h\nu = 200$ eV. At $h\nu = 200$ eV, the VB spectrum is mainly composed of Mn 3d states. On the other hand, both Mn 3d and O 2p states contribute to the VB spectral shape at $h\nu = 50$ eV. Both the spectra in Fig. 1(a) indicate that LaOMnAs is an insulator because of no spectral intensity at Fermi level (E_F).

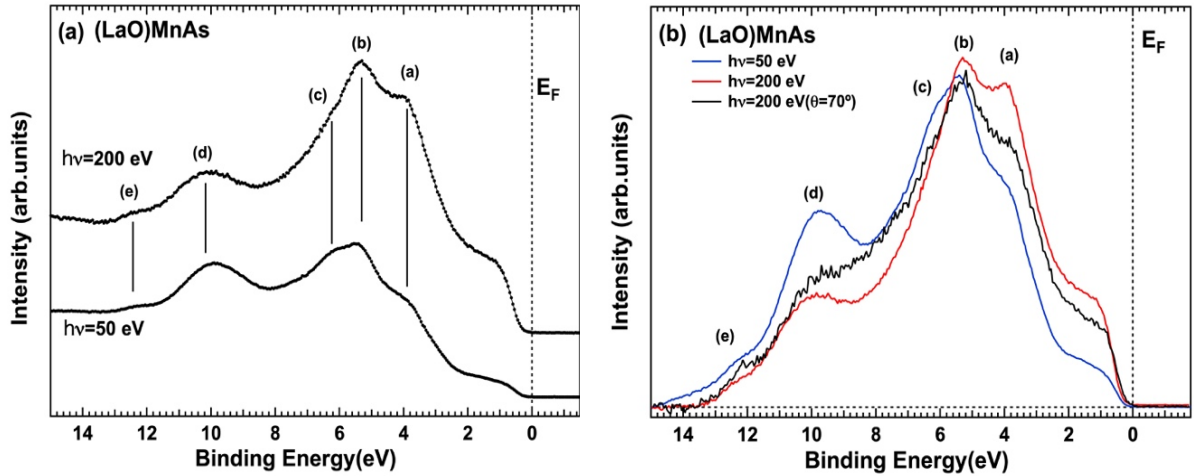


FIGURE 1. (a) VB spectra obtained at $h\nu = 50$ and 200 eV. (b) Comparison between the VB spectra at $h\nu = 50$ eV and 200 eV. The spectrum obtained at $h\nu = 200$ eV at a tilted angle (70° from the surface normal) is also shown. The positions of the markers (a)-(e) in Fig.1(b) are same as them in Fig.1(a).

Figure 1(b) shows a comparison between the VB spectra at $h\nu = 50$ and 200 eV. In addition, the spectrum obtained at an angle of 70 degrees from the surface normal is also shown, being more surface-sensitive than that at the normal emission angle. These spectra are normalized by the integrated spectral intensity between the binding energy (E_B) of -1.5 eV and 15 eV after subtracting the Shirley-type background. The spectral weight between E_F and $E_B = 5$ eV, which originates from Mn 3d states, is found to increase with $h\nu$. In contrast, the spectral weight around the markers (c)-(e) decreases with increasing $h\nu$ because of the less contribution of O 2p states to the spectrum at higher $h\nu$. Now, we can correctly evaluate the contribution of La 5p states by comparing these spectra with the HXPES spectrum. Furthermore, the spectral shape between E_F and $E_B \sim 5$ eV at $\theta = 70^\circ$ tends to become similar to that at $h\nu = 50$ eV, suggesting that the electronic structures near the surface are different from those in the bulk and the HXPES is essential to discover the bulk nature of this material.

REFERENCES

1. M. Zingl, E. Assmann, P. Seth, I. Krivenko, and M. Aichhorn, Phys. Rev. B **94**, 045130 (2016).
2. N. Emery, E. J. Wildman, J. M. S. Skakle, A. C. McLaughlin, R. I. Smith, and A. N. Fitch, Phys. Rev. B **83**, 144429 (2011).
3. A. Higashiyama, K. Nakagawa, A. Yamasaki, K. Nagai, S. Fujioka, Y. Kanai, K. Yamagami, H. Fujiwara, A. Sekiyama, A. A. Abozeed, T. Kadono, S. Imada, K. Kuga, M. Yabashi, K. Tamasaku, T. Ishikawa, S. Toyama, and K. Takase, J. Electron Spectrosc. Relat. Phenom. **220**, 58 (2017).
4. D. Takegami, L. Nicolaï, T. C. Koethe, D. Kasinathan, C. Y. Kuo, Y. F. Liao, K. D. Tsuei, G. Panaccione, F. Offi, G. Monaco, N. B. Brookes, J. Minár, and L. H. Tjeng, Phys. Rev. B **99**, 165101 (2019).

Direct Observation of Unoccupied and Occupied Electronic Structure of Cycloparaphenylenes

Kaname Kanai^a

^a Department of Physics, Faculty of Science and Technology, Tokyo University of Science, 2641 Yamazaki, Noda, Chiba 278-8510, Japan

Keywords: *n*-cycloparaphenylenes, Electronic structure

To date, countless π -conjugated molecules have been used in various electronic applications, such as in optoelectronic devices, light-harvesting devices and sensors. Most of these π -conjugated molecules are planar and have little diversity in their molecular backbones, limiting new molecular designs. The possibility of controlling the properties of molecules by employing non-planar backbones arose when *n*-cycloparaphenylenes ($[n]$ CPPs) (Fig. 1(a)) were first synthesized in 2008 [1].

Subsequent innovative synthesis strategies for this family of polycyclic aromatic hydrocarbons have been developed. $[n]$ CPP has a cyclic structure consisting of n benzene rings linked at their para-positions. These circularly aligned n phenylene units are the building blocks of armchair carbon nanotubes (CNTs) and have attracted much attention due to their potential for seeding the size-selective growth of CNTs. The $[n]$ CPP series is also fascinating for basic research, providing a good opportunity to study how the electronic structure of a π -conjugation system is modified by introducing strong strain into the molecular structure. The correlation between molecular structure and electronic structure is of great interest to both physical and synthetic chemists. The molecular structure of $[n]$ CPP is determined by the balance between energy gain due to delocalization of the π -electrons and the strain energy of the distorted molecular structure, resulting in conflict between stabilization of the electronic system and elastic strain of the molecular backbone. The distortion of each phenylene unit markedly influences their aromaticity, in analogy with fullerenes and CNTs, resulting in the unique reactivity of non-planar π -conjugated molecules. The mechanism by which the physical and chemical properties of a molecule are impacted by distortion can be understood from its electronic structure. $[n]$ CPP has an unusual electronic structure quite different from that of most other π -conjugated molecules and is due to its cyclic structure. For example, the energy gap between the highest occupied molecular orbital (HOMO) and the lowest unoccupied molecular orbital (LUMO) of $[n]$ CPP increases as the number of linked phenylene groups n increases. Density functional theory (DFT) calculations show that the HOMO-LUMO gap of $[n]$ CPP dramatically increases as n increases for n less than ~15, above which it approaches that of polyphenylenes (n P) (Fig. 1(b)). The evaluated HOMO-LUMO gaps of n P and $[n]$ CPPs are plotted as a function of n in Fig. 2. The HOMO-LUMO gap of $[n]$ CPP is dependent on the molecular size, which is opposite to that of n P. The HOMO-LUMO gap of $[n]$ CPP increases as n increases although that of n P decreases as n increases. The HOMO-LUMO gaps for n P and $[n]$ CPP begin to converge as n increases, indicating convergence at the limit of very long molecular chain lengths. Even-odd effects on the HOMO-LUMO gaps of n P and $[n]$ CPP were previously reported [2]. This n dependence of the HOMO-LUMO gap of $[n]$ CPP can be explained by considering the correlation between the degree of strain in the molecular structure and the degree of distortion of the wave functions of the π -orbitals in $[n]$ CPP.

Figure 3 shows the dihedral angle θ plotted against n for n P and $[n]$ CPP ($n = 8, 9$ and 12). The representation

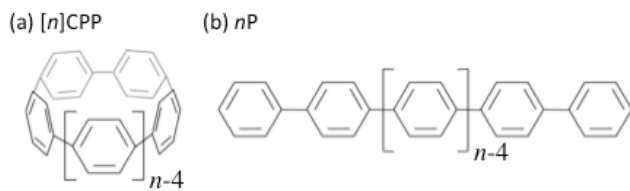


Figure 1. Molecular structure of $[n]$ CPP and n P.

of [8]CPP in the figure defines θ . Scatter data for each n represent the values of θ for each dihedral angle between two neighboring phenylene groups. The open diamonds connected by solid lines represent the average values of θ for each n . θ for nP remains around 36° and there is little dependence of θ , although the average value slightly decreases as the molecular size increases. In contrast, the average value of θ for $[n]CPP$ rapidly increases with increasing n and approaches the average value of θ for nP .

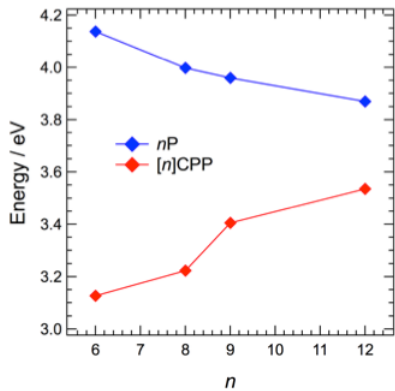


Figure 2. HOMO-LUMO gaps for nPs and $[n]CPPs$ calculated from the HOMO and LUMO energy levels.

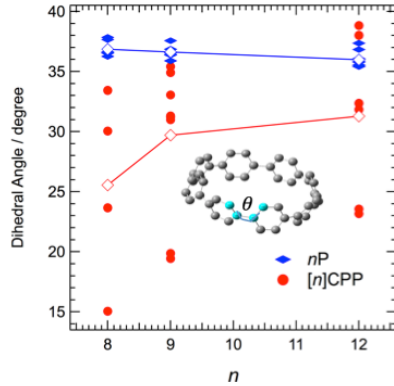


Figure 3. Calculated dihedral angle θ plotted as a function of n for nP (blue) and $[n]CPP$ (red). Open diamonds connected by solid lines represent the average values of θ for each n .

Figure 4(a) shows preliminary data of the UPS spectra combined with the IPES spectra of $[n]CPP$ ($n = 8, 9$ and 12). The HOMO-LUMO gap can be evaluated by the energy difference between the onsets of the UPS and IPES spectra, indicated by the vertical line, determined by comparison with the simulated spectra. The simulated spectra were individually shifted to reproduce the UPS and IPES spectra. Figure 4(b) shows the measured HOMO-LUMO gaps in the UPS and IPES spectra plotted against n , together with the calculated results previously shown in Fig. 2. The HOMO-LUMO gap experimentally obtained increases as n increases, consistent with the prediction by calculation.

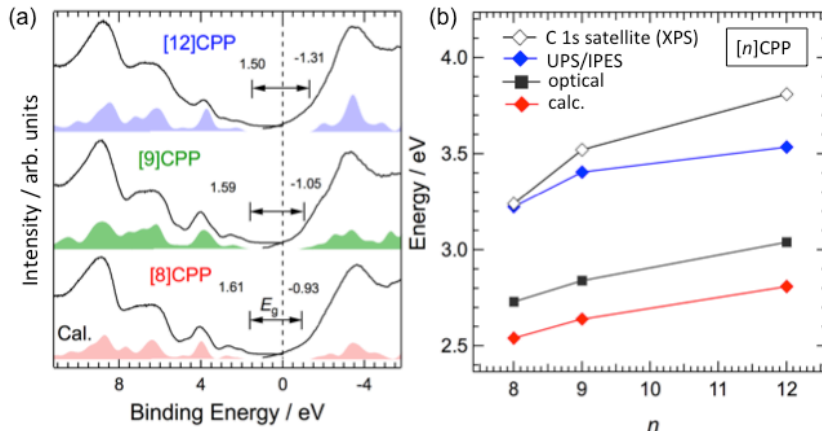


Figure 4. (a) UPS/IPES spectra of $[8]CPP$, $[9]CPP$ and $[12]CPP$. The bottom axis represents the binding energy measured from E_F . HOMO-LUMO gaps (E_g) were calculated by the energy difference between the onsets of the UPS and IPES spectra. Both onsets were determined by comparison between the experimental and simulated spectra. (b) Values of the HOMO-LUMO gap plotted against n and evaluated using the shake-up satellite in the XPS C 1s spectra, UPS/IPES spectra and UV-vis absorption spectra (optical) and calculation (calc.).

REFERENCES

- R. Jasti, J. Bhattacharjee, J. B. Neaton and C. R. Bertozzi, J. Am. Chem. Soc., 130, 17646–17647, (2008).
- T. Iwamoto, Y. Watanabe, Y. Sakamoto, T. Suzuki and S. Yamago, J. Am. Chem. Soc., 133, 8354–8361 (2011).

The observation of the composition dependence of the electronic structure in half-metal Heusler alloy Co₂Fe(Ga_xGe_{1-x})

K Goto^{a, b}, Y Sakuraba^b, T. Kono^c, H. Sato^d and K Hono^{a, b}

^aGraduate school of Pure and Applied Science, University of Tsukuba, 1-1-1 Tennodai Tsukuba 305-0047, Japan

^bNational Institute for Materials Science, 1-2-1 Senken, Tsukuba 305-0047, Japan

^cDepartmetn of Physical Science, Graduate School of Science, Hiroshima University, 1-3-1 Kagamiyama, Higashi-hiroshima 739-8526, Japan

^cHiroshima Synchrotron Radiation Center, Hiroshima University, 2-313 Kagamiyama, Higashi-hiroshima 739-0046, Japan

Keywords: Half-metal Heusler alloy, electronic structure, composition dependence

Co-based Heusler compounds such as Co₂MnSi and Co₂FeGa_{0.5}Ge_{0.5} (CFGG) are predicted to have high spin-polarization of the conduction electron at the Fermi level. These materials have been attracting much attention for spintronics devices of tunneling magnetoresistance (TMR) and current perpendicular to plane giant magnetoresistive (CPP-GMR) devices [1-4]. In previous study, Sakuraba *et al.* reported that the half-metallicity of Heusler alloys are sensitively changed by the shift of Fermi level due to the total valence electron number [5]. The CPP-GMR using the little hole-doped CFGG demonstrated high MR ratio over 280% [4], although, the half-metallicity is decreased with electron-doped CFGG. It is important for developing practical spintronics devices using CFGG to clarify the variation of a transport and the electronic band structure with changing the composition. However, no one has directly observed the changing of the electronic band structure with the composition about half-metallic Heusler alloys.

In this study, we prepared $L2_1$ ordered Co₂Fe(Ga_{1-x}Ge_x) thin films ($x = 0, 0.5, 1$) and performed ARPES measurement at BL-7 to observe the composition dependence of the electronic band structure. We controlled the position of Fermi level with the ratio of Ga and Ge. Chemical compositions of each samples were determined to be nearly stoichiometric using X-ray fluorescence analysis. Thin film samples were deposited by the magnetron sputtering method equipped at National Institute for Materials Science (NIMS) and they were delivered to HiSOR with keeping high vacuum ($\sim 3.0 \times 10^{-10}$ mbar) level by the suitcase chamber. Before ARPES measurement, samples were annealed at $\sim 500^\circ\text{C}$ for 30 min to obtain a clean surface. Photon energy was set at 64 eV and 141 eV for $x = 0.5$ and $x = 0, 1$, respectively, to observe Γ -X line in fcc Brillouin zone. The samples were kept at about 35 K during the experiments.

Figure 1(a), (b) and (c) show the band dispersion of Co₂Fe(Ga_{1-x}Ge_x) thin films with $x = 0, 0.5$ and 1, respectively. There is clear parabolic band structure around $k_{\parallel} = 0$ (Γ point) and $k_{\parallel} = 1.098$ (X point), and they are shifted to deeper energy side with increasing the valence electron number. This result about the band shift is consistent with the result of theoretical calculation. Therefore, the determination of Coulomb U effect and the optimization of spin-polarization with the chemical composition are expected by the detail

comparison with the theoretical calculation.

In summary, we have successfully observed the electronic band dispersion and its composition dependence of $L2_1$ ordered $\text{Co}_2\text{Fe}(\text{Ga}_{1-x}\text{Ge}_x)$ thin films ($x = 0, 0.5, 1$) by ARPES measurement at HiSOR BL-7. The band dispersion is shifted to deeper energy side with increasing valence electron number and this result is important for future study such as the determination of Coulom U effect and the optimization of composition to get high spin-polarization.

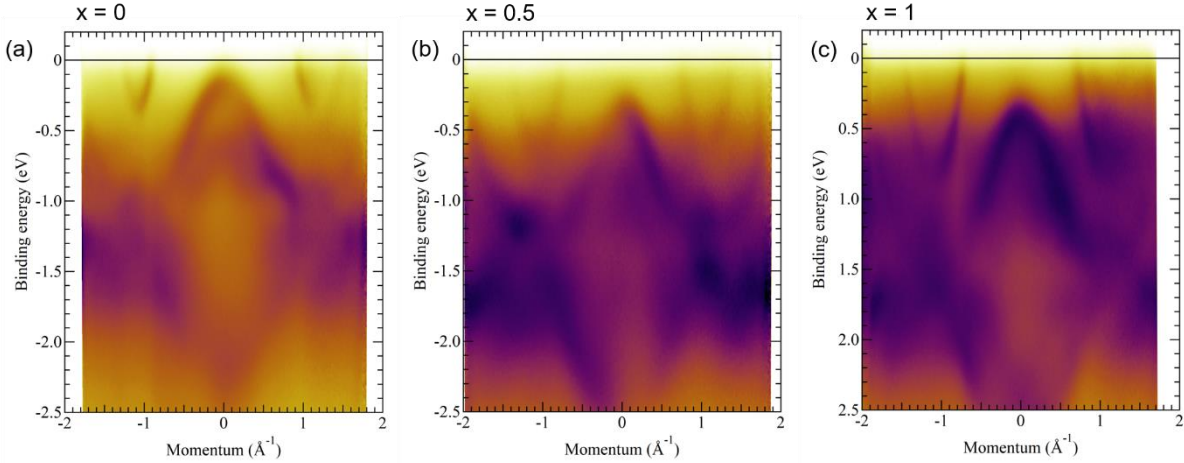


FIGURE 1. ARPES images along the Γ -X line of $\text{Co}_2\text{Fe}(\text{Ga}_{1-x}\text{Ge}_x)$ thin films. (a) $x = 0$, (b) $x = 0.5$ and (c) $x = 1$.

REFERENCES

1. Y. Sakuraba *et al.*, Appl.Phys. Lett. **88**, 192508 (2006)
2. T. Ishikawa *et al.*, J. Appl. Phys. **103**, 07A919 (2008)
3. S. Li *et al.*, Appl. Phys. Lett. **103**, 042405 (2013)
4. J. W. Jung *et al.*, Appl. Phys. Lett. **108**, 102408 (2016)
5. Y. Sakuraba *et al.*, Appl. Phys. Lett. **104**, 172407 (2014)

Photoelectron spectroscopy of Yb_4TGe_8 II

Hitoshi Yamaoka^a, Shunsuke Yamanaka^b, Masahito Hikiji^b, Chishiro Michioka^b, Naohito Tsujii^c, Hitoshi Sato^d, Kenya Shimada^d, and Kazuyoshi Yoshimura^b

^aRIKEN SPring-8 Center, 1-1-1 Kouto, Sayo, Hyogo 679-5148, Japan

^bDepartment of Chemistry, Graduate School of Science, Kyoto University, Kyoto 606-8502, Japan,

^cInternational Center for Materials Nanoarchitectonics (MANA), National Institute for Materials Science, 1-2-1 Sengen, Tsukuba, Ibaraki 305-0047, Japan

^dHiroshima Synchrotron Radiation Center, Hiroshima University, Higashi-Hiroshima, Hiroshima 739-0046, Japan

Keywords: photoelectron spectroscopy, Yb_4TGe_8 , temperature dependence, zero thermal expansion

Materials with zero thermal expansion (ZTE) or negative thermal expansion (NTE) have attracted many interests from both view points of the technological applications and physical mechanism because they are anomalous and rare. Yb_4TGe_8 ($T = \text{Cr}, \text{Mn}, \text{Co}, \text{Ni}$) has been found also to show ZTE upon cooling, but the ZTE mechanism was suggested not to be originated by the temperature-induced change in the Yb valence. [1] The crystal structure of Yb_4TGe_8 is CeNiSi₂-type with the space group of *Cmcm*. Yb and Ge zigzag chains are on the Ge square net forming the alternating layers stacked along the long *b*-axis. The temperature dependence of the lattice constants of Gd_4CrGe_8 and Yb_4AgGe_8 showed similar anomalous and the possibility of mixed valency as an origin of ZTE was eliminated. [1] While they claimed that ZTE was caused by the three-dimensional geometrical mechanism of the temperature-induced structural modulation raised from the charge transfer from *T* atoms to the Ge net, destabilizing the square-net structure of Ge. We have measured the electronic structure by high-resolution x-ray absorption spectroscopy (XAS) at the Yb-*L*₃ absorption edge for Yb_4TGe_8 at SPring-8. Pressure dependence of the crystal and electronic structures of the $T = \text{Cr}$ and Mn samples were also measured. The XAS spectra reflect the electronic structure of the empty states above the Fermi level. Here, we report the results of the photoelectron spectroscopy to observe the electronic structure below the Fermi level complementary to XAS.

Incident energy dependence of the valence band spectra of Yb_4MnGe_8 at room temperature around Yb 4*d*-4*f* resonance is shown in Fig. 1(a). Resonant enhancement of the intensity of the Yb³⁺ component was observed at 182 eV as observed in the other Yb compounds. [2] The temperature dependence of the spectra shown below were measured at off-resonant energy of 176 eV. Figure 1(b) shows a comparison of the valence band spectra of Yb_4TGe_8 ($T = \text{Cr}, \text{Mn}, \text{Fe}, \text{Ni}, \text{Co}$) at low temperatures. The intensity of the Yb²⁺ component is very weak compared to that of the Yb³⁺ component in these five compounds, indicating nearly Yb³⁺ valence state. The intensity of the Yb²⁺ component of Yb_4FeGe_8 is larger than those of the other four compounds and the Yb valence fluctuation of Yb_4FeGe_8 is relatively stronger than the others. Figure 1(c) shows a comparison of the Ge 3*d* core-level spectra at low temperatures. The peak of Ge 3*d* consists of 3*d*_{3/2} and 3*d*_{5/2}. The intensity of 3*d*_{5/2} of the $T = \text{Fe}$ and Ni samples is stronger than the others. The intensity of the Yb²⁺ component slightly increased at low temperatures as shown in Fig. 1(d). The spectra of the Yb³⁺ component shift to the lower binding energy at low temperatures. Such temperature-induced behavior has not been observed so far in the Yb compounds and this remains as an unresolved problem. Similar temperature dependence was also observed in other systems of $T = \text{Cr}, \text{Fe}, \text{Ni}$ and Co (the data are now shown here).

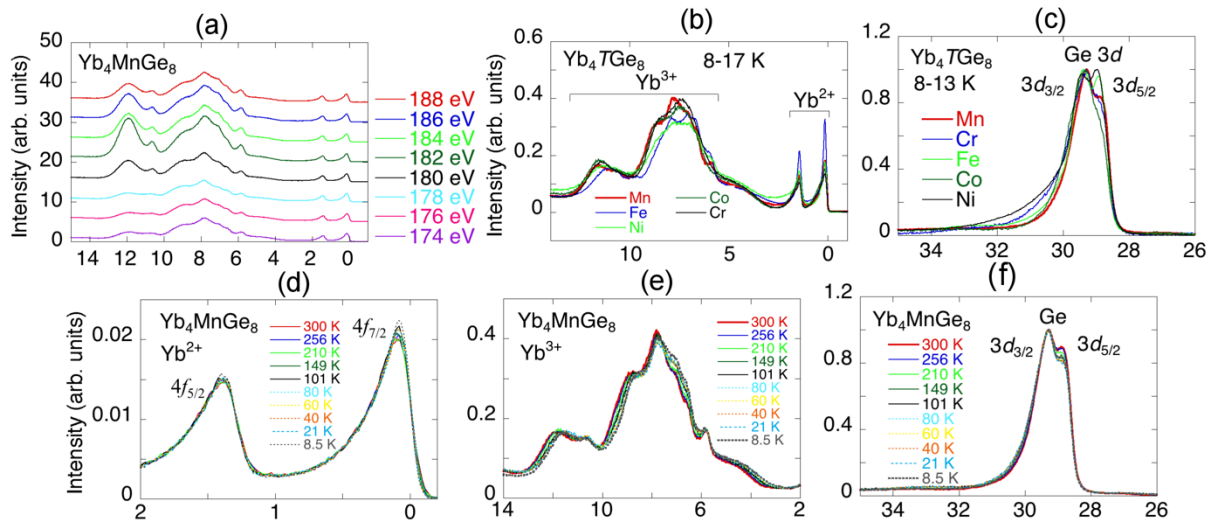


FIGURE 1. (a) Incident energy dependence of the valence band spectra of Yb_4MnGe_8 around Yb 4d-4f resonant energy at 300 K. (b) Comparison of the valence band spectra of Yb_4TGe_8 ($T = \text{Cr}, \text{Mn}, \text{Fe}, \text{Ni}, \text{Co}$) at 8–17 K. (c) Comparison of the Ge 3d core-level spectra of Yb_4TGe_8 ($T = \text{Cr}, \text{Mn}, \text{Fe}, \text{Ni}, \text{Co}$) at 8–13 K. (d) Temperature dependence of the valence band spectra of Yb^{2+} components of Yb_4CrGe_8 near the Fermi level. (e) Temperature dependence of the valence band spectra of Yb^{3+} components of Yb_4CrGe_8 . (f) Temperature dependence of the Ge 3d core-level spectra of Yb_4CrGe_8 .

REFERENCES

1. S. C. Peter, M. Chondroudi, C. D. Malliakas, M. Balasubramanian, and M. G. Kanatzidis, *J. Am. Chem. Soc.* **133**, 13840 (2011).
2. H. Yamaoka, P. Thunström, N. Tsujii, I. Jarrige, K. Shimada, M. Arita, H. Iwasawa, H. Hayashi, J. Jiang, H. Namatame, M. Taniguchi, N. Hiraoka, H. Ishii, K.-D. Tsuei, M. Giovannini, and E. Bauer, *Phys. Rev. B* **86**, 085137 (2012).

Electronic States of Lipoic acid and related molecules included in cyclodextrin

Kurumi Ando^a, Kiminori Baba^a, Hitoshi Sato^b and Hiroaki Yoshida^{a, b}

^a*Department of Physical Science, Hiroshima University,
1-3-1 Kagamiyama, Higashi-Hiroshima, 739-8526 Japan.*
^b*Hiroshima Synchrotron Radiation Center, Hiroshima University,
2-313 Kagamiyama, Higashi-Hiroshima, 739-0046 Japan.*

Keywords: Soft X-ray photoelectron spectroscopy, cyclodextrin, α -lipoic acid, inclusion

Cyclodextrin (CyD) is a cyclic oligosaccharide composed of several D-glucoses. It has a cylindrical shape and the number of linked D-glucoses decides a toric diameter. The units of 6, 7, and 8 D-glucoses are well-known as α -, β - and γ -CyD, respectively. The CyD has a special property to take other materials into an internal cavity. Such a phenomenon is called “inclusion”.

α -lipoic acid (ALA, Figure 1) is one of the functional materials which provides promotion of energy metabolism and strong anti-oxidation. It has, however, difficulty in application because of low tolerance for acid and heat. It is reported that the stability of α -lipoic acid is improved by including it in CyD [1]. Then the including compounds can be used easily to food and pharmaceutical products. There are few studies on the electronic states of α -lipoic acid included in CyD. In this study, soft X-ray photoelectron spectra (XPS) of S 2p core levels of α -lipoic acid and ALA @ γ -CyD were measured at BL-7 of HiSOR.

Figure 2 shows the obtained XPS spectra for ALA (top) and ALA@ γ -CyD (bottom). It is generally known that S 2p spectrum has two peaks, $J = 1/2$ and $J = 3/2$, with an area ratio of 1: 2 and a peak interval of 1.2 eV. Under these conditions, $J = 1/2$ and $3/2$ are regarded as one set of component, and fits are performed. As a result, the experimental data are reproduced with two set of components for ALA and three set of components for ALA @ γ -CyD. The components represented by the solid lines of ALA and ALA @ γ -CyD are same components because of almost the same peak positions. The dashed line and dotted chain line components newly appearing in ALA @ γ -CyD are considered to be due to inclusion. Since the solid line component occupies most of the XPS spectrum of ALA, it is due to sulfur atoms forming S-S bonds. The dashed line and dotted chain line are due to the sulfur atoms forming S-H bond [2] and S-O bond [3], respectively. Detail discussion on the inclusion structure of ALA into CyD is discussed.

REFERENCES

1. N. Ikuta *et al.*, *Int. J. Mol. Sci.*, **2013**, 14, 3639-3655.
2. P. E. Laibinis, *et al.*, *J. Am. Chem. Soc.*, **1991**, 113, 7152-7167.
3. K. S. Siow, *et al.*, *Sains Malays.*, **2018**, 47, 1911-1920.

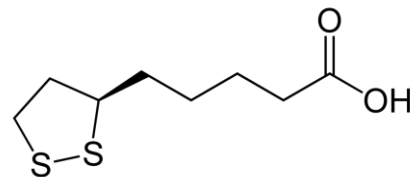


FIGURE 1 α -lipoic acid (ALA).

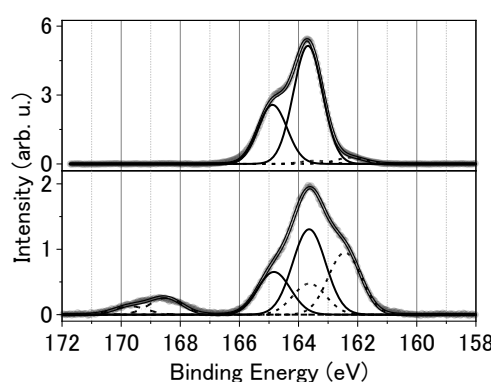


FIGURE 2 S 2p XPS spectra of ALA (top) and ALA @ γ -CyD (bottom).

Photoemission Study of the occupied molecular orbital in a TADF neat film

Yusuke Fukami^a, Keiki Fukumoto^b, Hitoshi Sato^c and Yoichi Yamada^a

^a*Institute of Applied Physics, University of Tsukuba,
1-1-1 Tennodai, Tsukuba, Ibaraki 305-8573, Japan*

^b*Institute of Materials Structure Science, High energy accelerator research organization (KEK),
1-1 Oho, Tsukuba, Ibaraki 305-0801, Japan*

^c*Hiroshima Synchrotron Radiation Center, Hiroshima University,
Kagamiyama 2-313, Higashi-Hiroshima 739-0046, Japan*

Keywords: Organic light emitting devices, Thermally activated delayed fluorescence, Photoemission spectroscopy

Thermally activated delayed fluorescence (TADF) molecules [1-2] are a group of molecules with a small energy difference between the singlet excited state (S_1) and the triplet excited state (T_1). They have attracted attention because they can achieve fluorescence emission with 100 % internal quantum efficiency by the reverse intersystem crossing from T_1 to S_1 . Currently, OLEDs using a TADF neat film for a light-emitting layer has been reported [3], which has opened up the application of TADF to the next generation devices. Therefore, it is necessary to control the molecular orientation of the TADF neat film and to elucidate its physical properties.

Controlling the molecular orientation of 4CzIPN neat films on several substrates has previously reported [4-5]. It was clarified that the 4CzIPN neat film takes a crystalline structure on HOPG substrate and an amorphous structure on SiO_2 substrate, as shown in figure 1. In this study, photoelectron spectroscopy was performed to understand the electronic structure of these films at BL-07 in HiSOR. Photon energy was set at 40 eV and 50 eV. Fermi level position was determined by measuring the Au spectra. All measurements were carried out at room temperature.

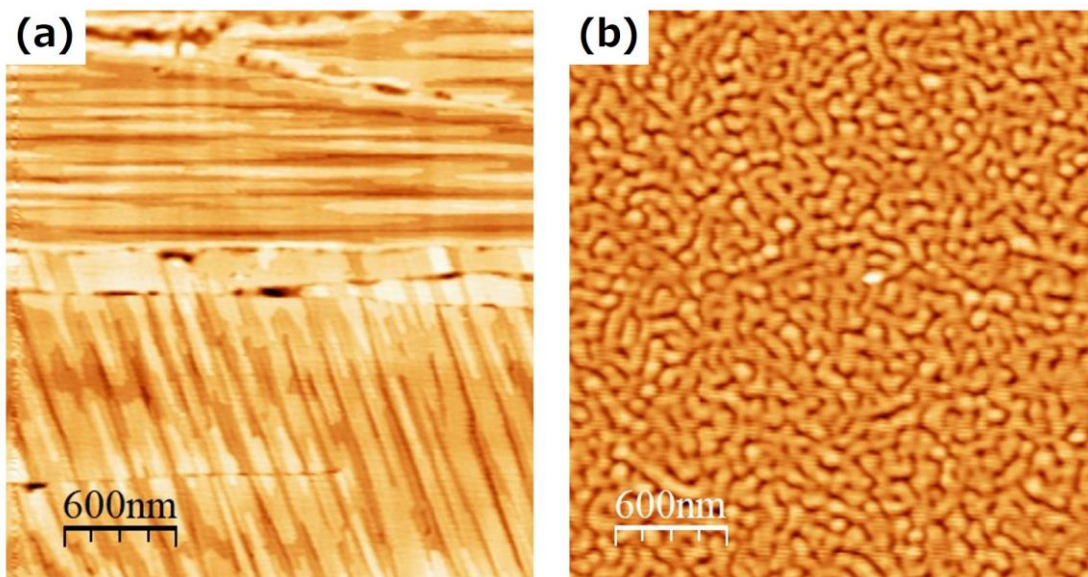


FIGURE 1. The AFM images of 4CzIPN neat film with a thickness of 50 nm (a) on the HOPG and (b) SiO_2 substrates.

Figure 2 shows the photoelectron spectra of 4CzIPN neat film with a thickness of 50 nm on the HOPG(orange line) and SiO₂ substrates(blue line). The origin of energy axis is set at the HOMO level. The energies of molecular orbitals in both spectra are almost identical, suggesting that the electronic structure is almost independent of film structure. However, the linewidth of the HOMO-1,2,3,4 of 4CzIPN/HOPG is a little smaller than that of 4CzIPN/SiO₂. This is because the environment surrounding the molecule is uniform in the crystalline structure of 4CzIPN/HOPG.

Figure 2.(b) shows the enlarged view around the HOMO level of figure 2.(a). The origin of energy axis is set at the fermi energy. The black circles in figure 2.(b) are the rising onsets of the spectrum. For the 4CzIPN neat film on HOPG and SiO₂, the onsets are 2.16 and 2.48 eV, respectively, with an energy difference of ~ 0.3 eV. This difference is resulted from the intermolecular polarization effect in the photoemission event[6-8]. In the crystalline film, the molecules surrounding the probed molecule perform a cooperative screening, which introduce a larger energy stabilization than in the amorphous one.

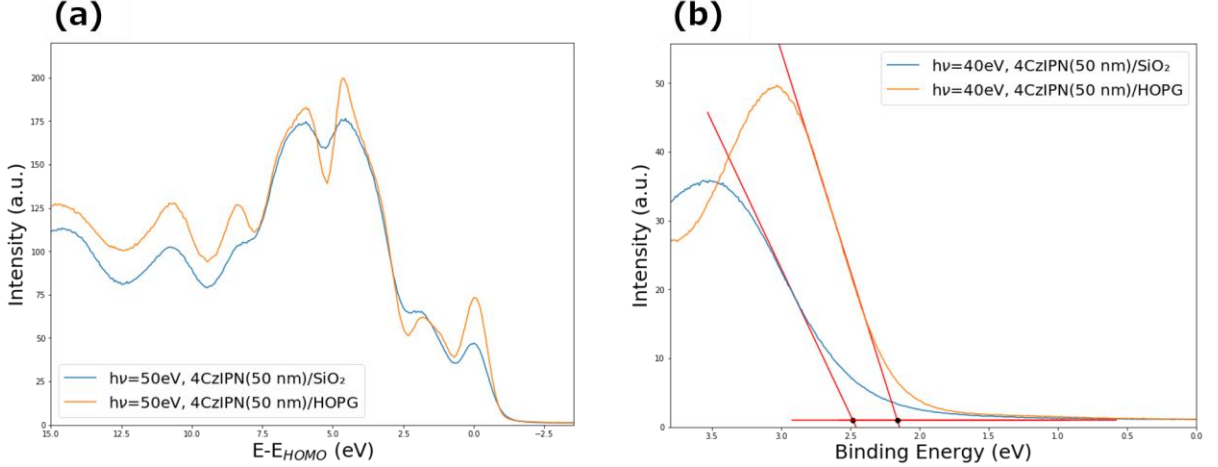


FIGURE 2. (a)The photoelectron spectra of 4CzIPN neat film with a thickness of 50 nm on the HOPG(orange line) and SiO₂(blue line) substrates and (b) its enlarged view around the HOMO level. The origin of energy axis is set at the HOMO level and the fermi energy, respectively.

REFERENCES

1. H. Uoyama, K. Goushi, K. Shizu, H. Nomura, and C. Adachi, *Nature* **492**, 234 (2012).
2. H. Kaji, H. Suzuki, T. Fukushima, K. Shizu, K. Suzuki, S. Kubo, T. Komino, H. Oiwa, F. Suzuki, A. Wakamiya, Y. Murata, and C. Adachi, *Nat. Commun.* **6**, 1 (2015).
3. N.B. Kotadiya, P.W.M. Blom, and G.J.A.H. Wetzelaer, *Nat. Photonics* (2019).
4. Y. Hasegawa, Y. Yamada, M. Sasaki, T. Hosokai, H. Nakano, and C. Adachi, *5* (2018)
5. Y. Hasegawa, H. Minami, S. Kanada, Y. Yamada, M. Sasaki, T. Hosokai, H. Nakano, and C. Adachi, *J. Photonics Energy* **8**, 1 (2018).
6. W. R. Salaneck, *Phys. Rev. Lett.*, **40** (1978) 60.
7. Y. Nakayama, S. Machida, T. Minari, K. Tsukagoshi, Y. Noguchi and H. Ishii, *Appl. Phys. Lett.* **93**, 173305 (2008).
8. H. Fukagawa, H. Yamane, T. Kataoka, S. Kera, M. Nakamura, K. Kubo, and N. Ueno, *Phys. Rev. B* **73**, 245310 (2006).

Characterization of Graphene Nanomesh Fabricated on Cu (111) Surface by Surface Reaction

Yuta Nagatomo^a, Hiroyuki Sakaue^a, Yukihiro Tominari^b, Shukichi Tanaka^b, Hitoshi Sato^c, and Hitoshi Suzuki^a

^a*Graduate School of Advanced Sciences of Matter, Hiroshima University,
1-3-1 Kagamiyama, Higashi-hiroshima, Hiroshima 739-8530, Japan*

^b*Advanced ICT Research Center, National Institute of Information and Communications Technology,
550-4 Iwaoka, Kobe, Hyogo 651-2492, Japan*

^c*Hiroshima Synchrotron Radiation Center, Hiroshima University,
2-313 Kagamiyama, Higashi-hiroshima, Hiroshima 739-0046, Japan*

Keywords: Graphene, Ullmann coupling, STM, Bottom-up.

Graphene nanomesh, a graphene sheet with an array of nanoholes, is a potentially applicable material to electronic devices because its bandgap can be controlled by the width between the neighboring two nanoholes [1]. Since, however, it is difficult to fabricate a precise array of nanoholes by lithography and etching processes, a new fabrication technique is required. Surface polymerization of aryl halides using Ullmann coupling on metal surface is one of the promising techniques for fabricating graphene nanostructures, by which a narrow graphene nanoribbon was successfully fabricated [2]. Its advantage is that the final structure is determined by the structure of the precursor molecule. To obtain the graphene nanomesh with precisely controlled nanohole array, we have used 2,3,6,7,10,11-hexabromotriphenylene (HBTP) (Figure 1a) and deposited them on Au (111) and Cu (111) surfaces [3]. HBTP molecule deposited on Au (111) surface at room temperature formed the mesh structure after annealing at 373 K. On Cu (111) surface, the molecules deposited on the surface heated at 473 K formed the mesh structure (Figure 1b), while the annealed molecules deposited at room temperature formed randomly connected filament structure. In the case of Cu surface, hexagonally arranged globules or noisy streaks were observed on the surface in addition to the mesh structure. The results indicate that by-product remained after the surface polymerization of HBTP molecules and they would affect on the chemical reaction. In this study, we have characterized the structure on the Cu surface on which the graphene nanomesh was formed, by XPS at BL-7 of HiSOR.

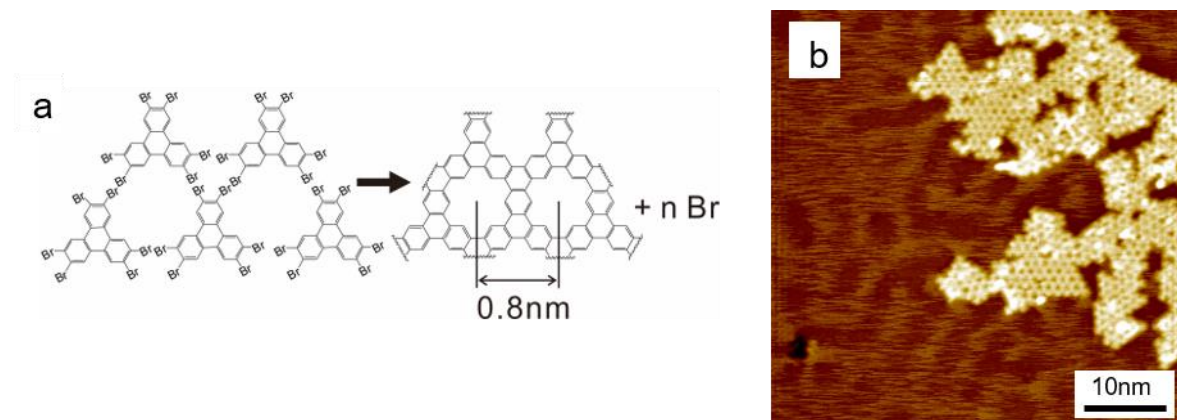


FIGURE 1. (a) Molecular structure of HBTP and the expected mesh structure. (b) STM image of graphene nanomesh formed by deposition of HBTP on Cu (111) at 473 K. The image obtained at 77K.

HBTP molecules were deposited on Cu (111) surface at room temperature and 473 K in a UHV chamber connected to a low temperature scanning tunnelling microscope (STM). The structures formed by HBTP

molecules were observed with STM. After that, the sample was moved to a transfer chamber whose vaccum was kept by a ion sputter pump operated by batteries[4] to transfer it from the STM chamber system to BL-7 chamber. The pressure was kept in the range of 10^{-7} Pa. The XPS measurements was carried out with the X-ray at energy 380 eV. The annealing of the sample at BL-7 was carried out at 523 K for 30 min by electron bombardment to backside of the sample plate.

The random filament structure was formed by HBTP deposited on Cu (111) surface at room temperature and noisy streaks were also observed on the surface. Its XPS spectrum showed C1s, Br3d5/2, and Br3d3/2 peaks at 285 eV, 69.3 eV, and 70.3 eV, respectively, with Cu3p peak that corresponds to the substrate (Figure 2a-1 and b-1). The peak positions of Br3d (Figure 2a-2) did not change after annealing at 523 K at BL-7. However, the relative peak height of Br3d to Cu3p decreased. The result suggests that the chemical bond of Br atoms did not changed but the amount of Br atoms decreased by annealing.

HBTP molecules deposited on the heated Cu surface formed the mesh structure with hexagonally packed globules on the surface and most of Br atoms of the molecules were dissociated from the molecules. The XPS spectra had also C1s and Br3d peaks with Cu3p one (Figure 2a-3 and b-3). The peak position of Br3d was the same as those of the sample prepared at room temperature. The lack of the chemical shift of Br3d peak between the sample prepared at room temperature and at 473 K indicates that Br atoms were dissociated form the molecules and bound to Cu atoms even at room temperature. The globules and streaks on Cu surface, which were observed in STM image, should be Br atoms. On both samples, Br atoms were sublimed from the surface by annealing at 523 K.

C1s peak shape depended on the preparation conditions. The peak of the sample prepared at room temperature (Figure 2b-1) had a notable component at lower binding energy but it decreased after annealing at 523 K (Figure 2b-2). The peak of the sample prepared at 473 K (Figure 2b-3) also had a small component of that and its decrease after annealing was small (Figure 2b-4). These two components reflect different chemical bonds of C. By analogy with this chemical shift of C1s and that in C-Si [5], we suppose that the component at the lower energy is due to C-Cu bond. Further XPS measurements of other materials, such as graphene and triphenylene, are necessary to identify the components.

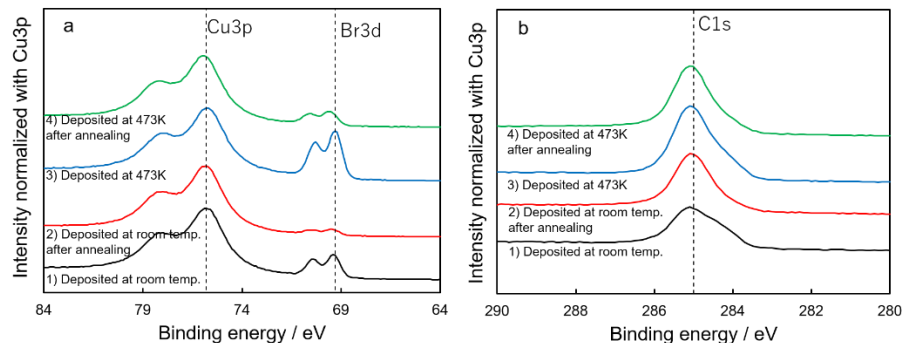


FIGURE 2. (a) XPS spectra of Cu3p and Br3d. (b) XPS spectra of C1s.

The globules and noisy streaks on Cu surface observed with the deposited HBTP molecules and the formed mesh structure were Br atoms dissociated from HBTP molecules. The annealing at 523 K was effective for decreasing them but they remained after annealing. The variation of C1s peak shape depending on the molecular deposition conditions and annealing should reflect the chemical bonds of C of HBTP molecules.

REFERENCES

1. J. Yang, M. Ma, L. Li, Y. Zhang, W. Huang, and X Dong, *Nanoscale* **6** 13301 (2014).
2. J. Cai, P. Ruffieux, R. Jaafar, M. Bieri, T. Braun, S. Blankenburg, M. Muoth, A.P. Seitsonen, M. Saleh, X. Feng, K. Müllen, and R. Fasel, *Nature* **466** 470 (2010); W. Wang, X. Shi, S. Wang, M.A. Van Hove, and N. Lin, *J. Am. Chem. Soc.* **133**, 13264 (2011); A. Basagni, F. Sedona, C.A. Pignedoli, M. Cattelan, L. Nicolas, M. Casarin, and M. Sambi, *J. Am. Chem. Soc.* **137**, 1802 (2015)
3. Y. Nagatomo, T. Kataoka, H. Sakaue, Y. Tominari, S. Tanaka, and H. Suzuki, *Jpn. J. Appl. Phys.* **59** SDDA16 (2020).
4. E. Kobayashi and S. Tanaka, *Vac. Surface Sci.* **62** 551(2019) (in Japanese).
5. S. Contarini, S.P. Howlett, C. Rizzo, and B.A. De Angelis, *Appl. Surface Sci.* **51** 177 (1991).